amU
Aix Marseille Université

NNT : 2023AIXM0001

THÈSE DE DOCTORAT

Soutenue à Aix-Marseille Université
le 19 décembre 2024 par

Michiko AHN FURUDATE

High-energy potential surfaces of Li_2 and the CO_3 system

Discipline
Sciences Chimiques

École doctorale
ED 250 : Sciences chimiques de Marseille

Laboratoire/Partenaires de recherche
Institut des Sciences Moléculaires de Marseille (iSm2)

Composition du jury

Céline LÉONARD PR Université Gustave Eiffel	Rapporteure
Thierry LEININGER PR Université Paul Sabatier	Rapporteur
Thierry STOECKLIN DR Université de Bordeaux	Examinateur
Mario BARBATTI PR Aix-Marseille Université	Président du jury
Gwang-Hi JEUNG PR Aix-Marseille Université	Directeur de thèse
Denis HAGEBAUM-REIGNIER MCF Aix-Marseille Université	Co-encadrant de thèse
Jean-Paul MALRIEU DR Université Paul Sabatier	Membre invité

iSm2 Institut des Sciences Moléculaires de Marseille UMR 7313

Affidavit

I, undersigned, Michiko AHN FURUDATE, hereby declare that the work presented in this manuscript is my own work, carried out under the scientific supervision of Gwang-Hi JEUNG and Denis HAGEBAUM-REIGNIER, in accordance with the principles of honesty, integrity and responsibility inherent to the research mission. The research work and the writing of this manuscript have been carried out in compliance with both the french national charter for Research Integrity and the Aix-Marseille University charter on the fight against plagiarism.

Some parts of this work have been presented to the scientific communities as can be seen in the following page.

Marseille, 21st of October



This work is licensed under Creative Commons Attribution-NonCommercial-NoDerivatives 4.0 International Public License

List of publications and conference attendances

List of publications as part of the thesis project

1. "Resonant Ionic, Covalent Bond, and Steric Characteristics Present in $^1\Sigma_u^+$ States of Li_2", Molecules 27, 2022.

2. "Singlet and triplet electronic states involved in the reactions CO_2+O $\leftrightarrows$ CO+O_2", under review.

Attendances to conferences, workshops or summer schools as part of the thesis project

1. July, 2021, Optical Society of Korea, Online, Oral presentation

2. July, 2022, International Symposium on Rarefied Gas Dynamics, Seoul, Oral presentation

3. July 2022, Europe-Korea Conference on Science and Technology, Marseille, Oral presentation

4. March 2023, 4th European Conference on Non-Equilibrium Gas Flows, Eindhoven, Oral presentation

Résumé

L'exploration de Mars, la planète la plus proche de la Terre, devrait permettre de mieux comprendre l'origine et l'évolution du système solaire. De plus, on s'attend à ce que Mars ait un potentiel d'eau, de vie et de ressources précieuses, ce qui en fait la cible principale des missions spatiales. Lors de l'entrée sur Mars, le vaisseau spatial est soumis à des conditions thermiques extrêmes lorsqu'il pénètre dans l'atmosphère martienne à des vitesses hypersoniques (5 à 10 km/s), où les molécules de gaz subissent des excitations thermiques et des réactions chimiques à haute température. Ces phénomènes, y compris la dissociation de CO_2, produisent des espèces telles que C, CO et C_2, qui influencent de manière critique les environnements thermiques autour du vaisseau spatial. La compréhension de ces processus est nécessaire pour la conception des systèmes de protection thermique (TPS), qui doivent protéger le vaisseau spatial de la destruction causée par les conditions extrêmes de température.

Cette étude concerne les surfaces d'énergie potentielle (SEP) du système CO_3, en particulier leur rôle dans la réaction $CO_2 \rightarrow O_2 + CO$, un processus clé pendant le vol d'entrée dans l'atmosphère martienne.

Le chapitre 2 commence par une exploration du dimère Li_2 en tant que système modèle pour comprendre les interactions complexes des états électroniques excités. Cette analyse a été réalisée à l'aide des méthodes MRCI (Multi-Reference Configuration Interaction), et différents types de liaisons moléculaires, c'est-à-dire résonantes, ioniques, covalentes et de van der Waals, ont été observées en fonction des différentes distances internucléaires et des différents niveaux d'énergie. Les résultats ont permis d'acquérir une compréhension fondamentale du caractère de la liaison, ce qui a aidé à étudier des molécules plus complexes comme CO_3.

Dans le chapitre 3, les SEP de CO_3 ont été étudiées pour identifier les états d'équilibre, les états de transition et les chemins réactionnels pour la réaction $O + CO_2 \rightarrow O_2 + CO$. L'analyse a révélé de nouveaux intermédiaires réactionnels et états de transitions, qui n'avaient pas été documentés auparavant.

Le chapitre 4 se concentre sur le calcul des constantes de vitesse de réaction sur la base de ces données relatives aux chemins de réaction. Les théories de l'état de transition et Rice-Ramsperger-Kassel-Marcus (RRKM) ont été utilisées pour calculer les constantes de vitesse canoniques. En outre, les équations maîtresses ont été résolues à différentes températures par une méthode de discrétisation du domaine des énergies, à l'aide du logiciel libre MESMER. Les constantes de vitesse obtenues sont comparées aux données expérimentales existantes et à d'autres études théoriques.

Cette étude devrait permettre de mieux comprendre les flux d'entrée martiens à

haute température sur n'importe quel objet, y compris les météorites, les astéroïdes et les engins spatiaux artificiels, ainsi que leurs conséquences, afin de contribuer aux sciences planétaires au sens large. Plus spécifiquement, les résultats sur le système CO_3 présentés dans cette thèse peuvent fournir de nouvelles informations sur les réactions hors équilibre qui se produisent dans des conditions hypersoniques, offrant ainsi des données importantes pour les futures missions d'exploration de Mars.

Mots clés: oxydes de carbone, dimère du lithium, calculs *ab initio*, surfaces d'énergie potentielle, états hautement excités, constante de vitesse de réaction

Abstract

Exploration of Mars, the planet closest to Earth, is expected to bring a significant insight into the origin and the evolution of the solar system. Moreover, it is expected that Mars has the potential for water, life, and valuable resources, making it the primary target for space missions. During the Mars entry, the spacecraft experiences extreme aeroheating conditions as they fly into the Martian atmosphere at hypersonic speeds (5 to 10 km/s), where gas molecules undergo high-temperature thermal excitations and chemical reactions. These phenomena, including the dissociation of CO_2, produce species such as C, CO, and C_2, that critically influence the thermal environments around the spacecraft. Understanding these processes is necessary for the design of thermal protection systems (TPS), which is required to protect the spacecraft from destruction caused by extreme aeroheating.

This study investigates the potential energy surfaces (PES) of the CO_3 system, focusing on their role in the reaction $CO_2 \rightarrow O_2 + CO$, a key process during Martian atmospheric entry flight.

Chapter 2 begins with an exploration of the Li_2 dimer as a model system to understand complex interactions in excited electronic states. This analysis has been performed using Multi-Reference Configuration Interaction (MRCI) methods, and different types of molecular bonding, i.e., resonant, ionic, covalent, and van der Waals, have been observed according to different internuclear distance and different energy level. The results have provided a fundamental understanding on the bonding character, that helped to study more complex molecules like CO_3.

In Chapter 3, PESs of CO_3 were investigated to identify equilibrium states, transition states, and reaction pathways for the $O + CO_2 \rightarrow O_2 + CO$ reaction. The analysis have revealed novel reaction intermediates and transition states, which were not previously documented.

Chapter 4 focuses on calculating the reaction rate constants based on these reaction pathway data. Transition-state theory and the Rice–Ramsperger–Kassel–Marcus (RRKM) theory were used to calculate the canonical rate constants. Also, energy grained master equations at various temperatures were solved by the open-source software, MESMER. The obtained rate constants are compared with existing experimental data and other theoretical studies.

This study would help better understanding the high-temperature Martian entry flows over any object including the meteorites, asteroids, and man-made spacecrafts, and their consequences so that to contribute to broader planetary sciences. More specifically, the findings on the CO_3 system presented in this dissertation may provide

new insights into non-equilibrium reactions that occur in hypersonic conditions, offering important data for future Mars exploration missions.

Keywords: carbon oxides, lithium dimer, *ab initio* calculations, potential energy surfaces, highly excited states, reaction rate constants

Acknowledgements

First and foremost, I am profoundly grateful to Dr Denis HAGEBAUM-REIGNIER, whose constant support and advice have been truly indispensable. His detailed feedback and tireless assistance in every step of my research process have been invaluable.

I would like to express my deepest gratitude to Prof. Gwang-Hi JEUNG, for his invariable guidance, insightful feedback, and continuous support throughout my research. His expertise and encouragement have greatly contributed to the completion of this dissertation.

I also extend my thanks to my thesis committee members, Prof. Céline LÉONARD, Prof. Thierry LEININGER, Dr Thierry STOECKLIN, Prof. Mario BARBATTI, and Dr Jean-Paul MALRIEU, for their valuable comments and advice that greatly improved the quality of this work.

I am sincerely grateful to my colleagues and friends at CTOM (Chimie ThéOrique et Modèles) for their unwavering support and fruitful discussions. The time we spent together has been invaluable and irreplaceable. I am also thankful to the technical and administrative staff for their consistent support throughout my research.

Lastly, I would like to thank my husband, Mu-Young, and my son, Jae-Yun, for their endless understanding, patience, and support throughout this challenging period.

Table of contents

Affidavit 2

List of publications and conference attendances 3

Résumé 4

Abstract 6

Acknowledgements 8

Table of contents 9

1 Introduction 11
- 1.1 Background and Motivations . . . 11
  - 1.1.1 Atmospheric Entry Technologies in Space Exploration . . . 11
  - 1.1.2 Aeroheating in Hypersonic Entry Flight and Thermal Protection System Design . . . 12
  - 1.1.3 Nonequilibrium Atomic and Molecular Processes in Hypersonic Entry Flight . . . 16
- 1.2 Thermochemistry in Hypersonic Entry Flow for Mars Missions . . . 18
  - 1.2.1 Importance of $O + CO_2 \rightarrow O_2 + CO$ reaction . . . 18
- 1.3 Modeling molecular processes . . . 22
- 1.4 Outline of this thesis . . . 23

2 Complexity of the electronic excited states : Li_2 as example 24

3 Potential energy hyper-surfaces of the CO_3 complex 35
- 3.1 Introduction . . . 36
  - 3.1.1 Background . . . 36
  - 3.1.2 Objectives . . . 38
- 3.2 Computational methods . . . 38
  - 3.2.1 Structure optimizations and energy refinement . . . 38
  - 3.2.2 PES, Intersection points and seam curves . . . 39
  - 3.2.3 Reference energies of reactants and products . . . 39
- 3.3 Results and discussion . . . 40
  - 3.3.1 Formation of planar star-shape CO_3 and quenching reaction . . . 42
  - 3.3.2 Formation of chain-shape CO_3 states and reaction pathways . . . 45
  - 3.3.3 Property changes along the reaction pathways . . . 49
  - 3.3.4 Local shape of the PES's . . . 52

3.4 Conclusions 55
Bibliography of Chapter 3 57

4 Kinetics of the reactions $CO_2 + O \rightarrow CO_3 \rightarrow CO + O_2$ 60
4.1 Introduction 60
4.2 Method of Calculations 61
4.2.1 Stationary Points on PES of CO_3 system 61
4.2.2 Reaction rate constants 62
4.2.3 Energy grained master equation 62
4.3 Results 63
4.3.1 IRC calculations and TST rate constants 63
4.3.2 RRKM and BM rate constants 64
4.4 Summary 70
Bibliography of Chapter 4 71

Conclusion 73

1 Introduction

Contents

1.1 Background and Motivations 11
1.1.1 Atmospheric Entry Technologies in Space Exploration 11
1.1.2 Aeroheating in Hypersonic Entry Flight and Thermal Protection System Design 12
1.1.3 Nonequilibrium Atomic and Molecular Processes in Hypersonic Entry Flight 16
1.2 Thermochemistry in Hypersonic Entry Flow for Mars Missions 18
1.2.1 Importance of $O + CO_2 \rightarrow O_2 + CO$ reaction 18
1.3 Modeling molecular processes 22
1.4 Outline of this thesis 23

1.1 Background and Motivations

1.1.1 Atmospheric Entry Technologies in Space Exploration

Space development that began in the 1960s has led to various technological breakthroughs that have enriched our lives. For example, communication satellites have made it possible to connect people around the world, and the Global Positioning System (GPS) allows us to travel easily via the navigation systems. The development of weather satellites has improved weather forecasting accuracy, bringing benefits to the agriculture and many industries that depend on weather conditions, such as agriculture and fisheries. Although early space development was primarily led by national governments, participation by private companies has been increasing since the 2000s, and the space development market is expected to expand even further. Additionally, exploring other planets and deep space to seek the origins of humanity and the potential for new extraterrestrial resources and life forms not only satisfies humanity's intellectual curiosity but also has significant implications for the further development and survival of humankind.

Currently, many space exploration programs are being advanced in various countries, not only the United States and the European Union but also several countries in Asia and South America. The National Aeronautics and Space Administration (NASA) in the United States is operating the Artemis mission, aiming to send the first woman and the next man to the Moon by 2025 (https://www.nasa.gov/feature/artemis/). NASA plans to establish a sustainable base on the lunar surface

and apply the developed technologies to future manned Mars missions. The European Space Agency (ESA) launched a probe in 2023 as part of the JUICE (Jupiter Icy Moons Explorer) mission to explore the possibility of water and life on Jupiter's moons (https://www.esa.int/Science_Exploration/Space_Science/Juice). Additionally, a Mars exploration mission, the ExoMars, is ongoing to send a rover to the Martian surface to search for signs of life on Mars.(https://www.esa.int/Enabling_Support/Operations/Current_and_future_missions)

In such space exploration missions, the technologies to transport payloads to the planet's surface are essential. The capsules carrying these payloads are launched from Earth, travel through space, and enter the planets' atmospheres at extremely high speeds. These speeds exceed 10 km/s and can even reach up to 40 km/s; speeds that would allow you to fly from Marseille to Paris within under one minute. To ensure the capsule reaches its destination using aerobraking without being deflected by the planet's atmosphere or burning up due to aeroheating, it is necessary to predict the forces and heat acting on the capsule during the atmospheric entry flight. Because it is difficult and expensive to build ground facilities that can replicate the physical environment of planetary entry, theoretical and numerical approaches are indispensable in predicting these forces and heat during the entry.

Apart from the man-made entry space vehicle, every planet or satellite is stroken by a large number of meteorites and asteroids. The interface between those objects and the shock wave front also creates a high temperature layer of atmosphere. So the high temperature chemistry in this environment would play a great role to understand the atmosphere of the planets. It is also one of the aims of this work.

In the next subsection, we will explore the physical background of aeroheating phenomena during atmospheric entry and discuss the technological requirements for accurate prediction of heat in theoretical and numerical analyses.

1.1.2 Aeroheating in Hypersonic Entry Flight and Thermal Protection System Design

The pressure disturbances in longitudinal wave form, i.e., the sound, propagate through gas at the speed of sound (that will be noted here as a). According to Newton's isothermal model corrected by Laplace's adiabatic model (1816), $a = (\gamma P/\rho)^{1/2}$, where γ is the ratio of the specific heat at constant pressure to that at constant volume (C_p/C_v, about 1.4 for the diatomic gases composing the air), P is the pressure and ρ is the density of the gas. For the ideal gas, $a = (\gamma RT/M)^{1/2}$, where R is the gas constant, T is the absolute temperature and M is the molar mass. When the source of pressure disturbance, e.g., a point-like object, is stationary, the sound wave propagates spherically at the speed of sound. When the point object moves with a speed less than that of the sound, the sound wave propagates as shown in Fig. 1.1a. When the point object moves with the same speed with the sound, the wave front forms a plane as in Fig. 1.1b. When the point object moves faster than the speed of sound, the wavefront forms a cone shape with its apex located at the source, as illustrated in Fig. 1.1c. This implies that information about the movement of an object traveling at supersonic speed in

the gas is not transmitted ahead of the object. Therefore, when an object moves at a speed faster than the speed of sound, a detached shock wave, which is different from the ordinary sound wave, with a discontinuity in thermodynamic parameters (density, pressure, temperature, entropy, etc.) is formed at the front of the object. For an object with finite volume moving with supersonic speed, the shock front takes a form of the hyperbola of revolution with assymptotes making twice of the Mach angle. (Fig. 1.2)

The ratio of the speed of the sound source (moving object) to the speed of sound is called the Mach number, denoted as M_a. Flights of objects at speeds exceeding $M_a = 1$ are called supersonic flights. The typical flight speed of atmospheric entry capsules corresponds to Mach 10-30, which belongs to the hypersonic speed regime. During the hypersonic entry flight, the gas between the ambient air and the moving capsule is strongly compressed thus changing suddenly the local gas density and that creates a strong detached shock wave. This adiabatic compression causes the increase of the local pressure accompanied by the increase of the local temperature of the gas, $(\Delta T)/(\Delta P) > 0$, according to the gas law, often reaching several thousand to tens of thousands of degrees Celsius.

The capsule contacting such a hot gas is heated up due to the convective heat transfer. When the temperature is high enough to initiate ionization of the gas, the gas emits radiation, which also contributes to heating the capsule. The heat transferred to the capsule can reach the order of several hundred megawatts per square meter (MW/m^2), which is comparable to the heat flux at the surface of the Sun. (Fig. 1.3) Therefore, the thermal protection system (TPS), which protects payloads from such a severe aeroheating environment, is one of the most important technologies for successful entry missions.

The choice of materials and methods of TPS depends on the entry speed and the resulting thermal environment. For example, in the case of the reentry flight of Space Shuttles, the entry speed was about 7.6 km/s. For this moderate entry speed, the peak heat transfer along the entry trajectory was about 0.4 MW/m^2, and the dominant heating mechanism is convective heat transfer. The reusable thermal insulator tiles have been used since the wall temperature could remain below the withstand temperature of the tiles at about 1500K.(Fig. 1.4a) On the other hand, in the case of the Jorevian entry flight of the Galileo Probe, whose entry speed was as high as 45 km/s, the ablative heat shield was used to protect the probe from the significant radiative heating which peak heating exceeded 300 MW/m^2.(Fig. 1.4b)) The materials of ablative heat shields, which are typically phenolic carbons, pyrolyze and sublimate in such a heating environment. The pyrolysis gas ablated from the heat shield surface blocks the convective heat, and the carbon species in the pyrolysis gas absorb radiation before the radiation reaches the body surface.

Figure 1.5 shows the images of the Stardust Sample Return Capsule, which has an ablative TPS, throughout its lifecycle. Stardust was launched on February 7, 1999, from Florida. The objective of the mission was to collect samples from the coma of comet Wild 2 and return them to Earth. After successfully collecting thousands of particles from Wild 2 on January 2, 2004, Stardust returned to Earth and landed in the Utah desert on January 15, 2006. The image on the left in Fig. 1.5 shows the capsule before

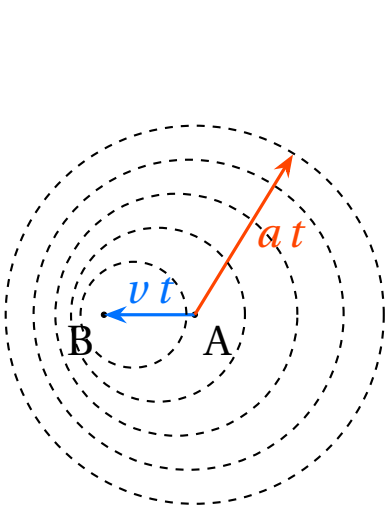

(a) Subsonic : $v < a$

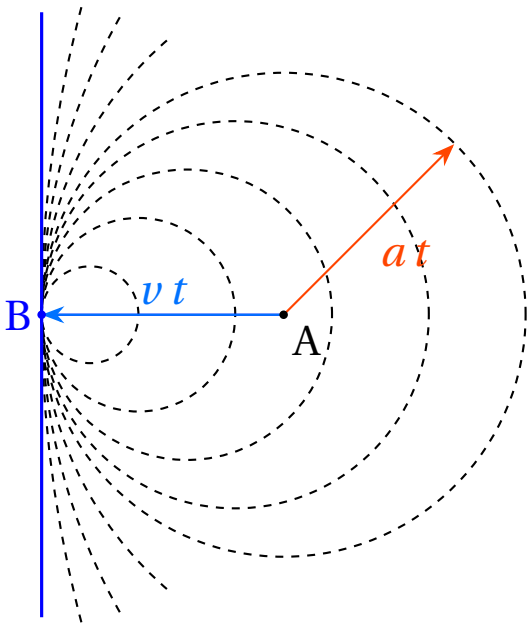

(b) Sonic : $v = a$

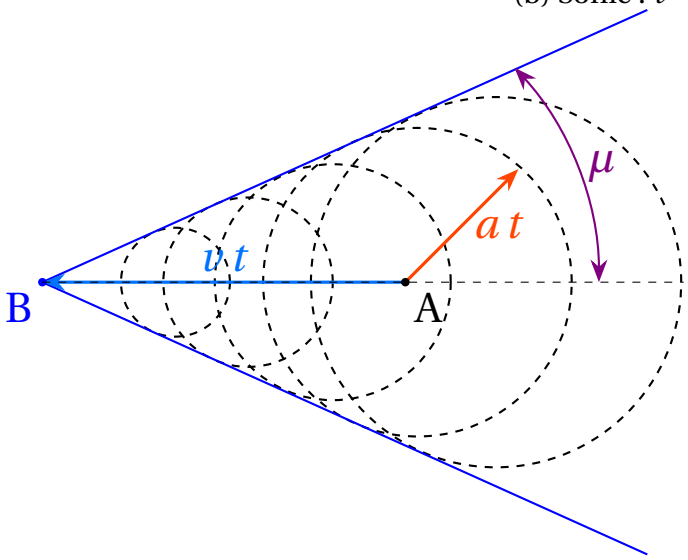

(c) Supersonic : $v > a$

FIGURE 1.1 : Sound waves generated by a point-like object moving with a speed v, where a is the speed of sound and t is the lapse of the time measuring the travel time ; (a) $v < a$, (b) $v = a$ where the shock front forms a plane, (c) $v > a$ where the shock front forms a cone and μ is called Mach angle.

launch, covered with a white Thermal Protection System (TPS). The middle image captures the capsule during the reentry flight, emitting a bright light, which is the radiation emitted from ionizing gases around the capsule. The image on the right shows the capsule, blackened and reduced in size after landing due to the pyrolysis of TPS caused by aeroheating during the entry flight.

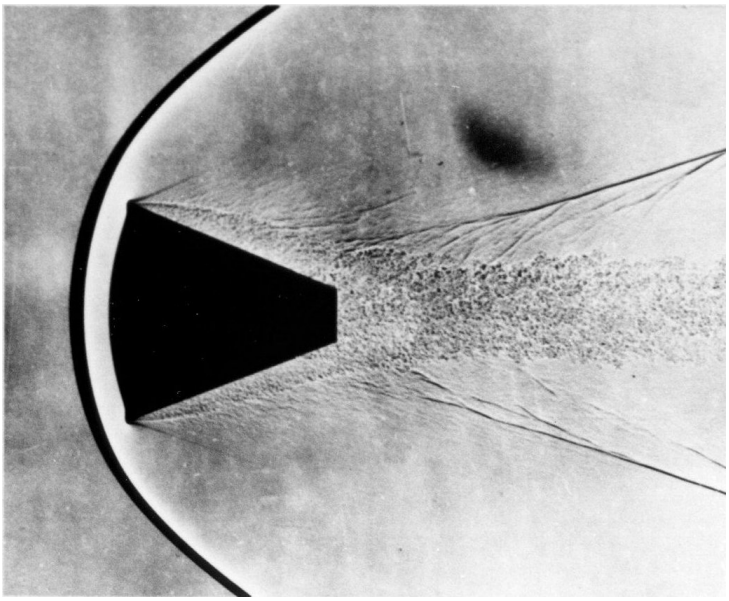

FIGURE 1.2 : Shock wave over an experimental model of reentry capsule (Shadowgraph : Gemini capsule flight stability study, NASA ID : ARC-1963-A-31214) where the stern wave behind the capsule is also visible.

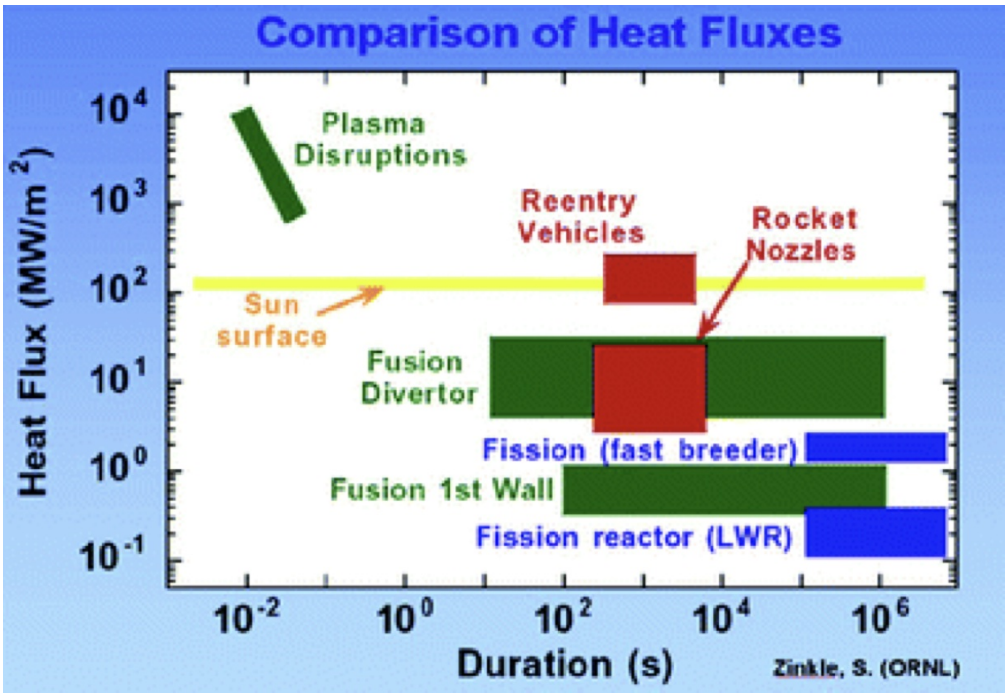

FIGURE 1.3 : Comparison of Heat Fluxes

As insight from these images, upon the ablative TPS's design, techniques to predict the amount of heat flux to the heat shield are essential for determining the size of the heat shield not to be used during the entry flight. The convective heat flux depends on the temperature of the gas on the heat shield surface and the radiative heat transfer depends on the temperature and number density of the ionizing gases. In the hypersonic entry flight, because the capsule moves faster than the speed of sound, the atomic and molecular processes, such as internal energy excitation, dissociation, and ionization, are likely to be nonequilibrium. Understanding these nonequilibrium processes is crucial for accurately predicting the heat flux on entry capsules. These processes will be explained in more detail in the next subsection.

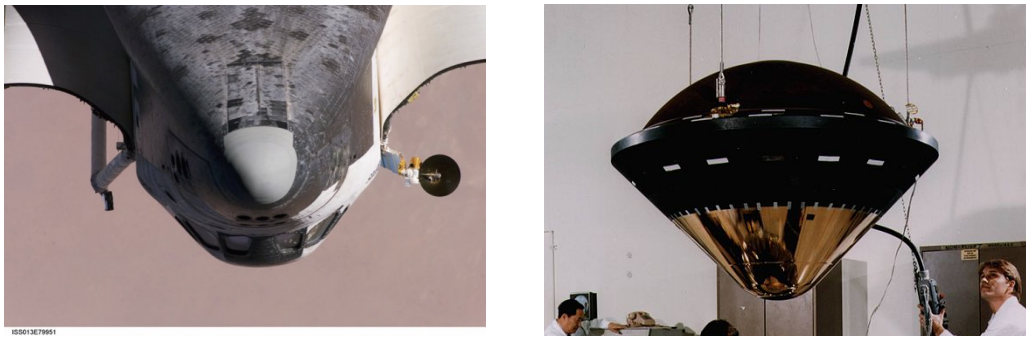

a. Thermal insulator tiles on STS-115 b. Ablative heat shield in Galileo Probe

FIGURE 1.4 : Heat Shields on Space Vehicles (https://images.nasa.gov/)



a. Before the entry flight b. During the entry flight c. After the entry flight

FIGURE 1.5 : Photographs of the Stardust Sample Return Capsules (https://images.nasa.gov/)

1.1.3 Nonequilibrium Atomic and Molecular Processes in Hypersonic Entry Flight

At the hypersonic speeds, the gas between the detached shock wave and the entry capsule undergoes significant atomic and molecular processes, such as internal energy

excitation, dissociation, and ionization, which is referred to as high-temperature real-gas phenomena. These processes are schematically explained in Fig. 1.2 for a scenario where a fluid element containing a large number of diatomic molecules moves and crosses a shock wave.

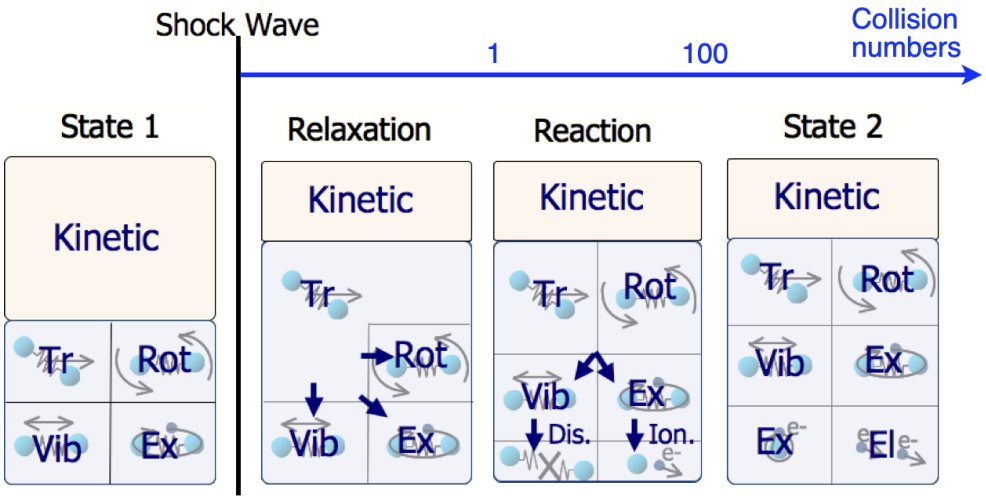

FIGURE 1.6 : Schematics of energy conversion behind the shock wave

A moving fluid element has bulk kinetic energy associated with its macroscopic speed and internal energy associated with its temperature, which measures the thermal activities of the molecules in the fluid element. The total energy, which is the sum of the bulk kinetic energy and internal energy, is conserved across the shock wave. A fluid element moving at hypersonic speed in a low-temperature gas possesses a large bulk kinetic energy and a small internal energy. When the fluid element suddenly decelerates by crossing the shock wave, a large portion of the bulk kinetic energy is converted into the internal energy of the molecules, increasing their thermal kinetic energy and, consequently, the temperature, in accordance with the law of energy conservation.

Molecules have degrees of freedom associated with thermal activities in translational, rotational, vibrational, and electronic excitation modes. The average kinetic energy for each type of mode in a bulk gas can be described as a function of the internal temperature. For the translational mode in equilibrium, the Maxwell distribution describes the average kinetic energy of the molecules, which is associated with the translational temperature. For each of the rotational, vibrational, and electronic excitation modes in equilibrium, the average energy is described by the Boltzmann distribution over their energy levels, characterized by rotational, vibrational, or electronic excitation temperatures, respectively. In thermal equilibrium between modes, the internal temperatures corresponding to these different degrees of freedom have the same value.

Before crossing the shock wave, the molecules in the fluid elements are in equili-

brium at low temperatures both within and between the internal energy modes.(State 1) The sudden energy conversion from bulk kinetic energy to internal energy at the shock wave initially excites the translational mode, leading to a sudden rise in translational temperature. The density of the fluid element also increases due to compression by the shock wave. As a result, the molecules behind the shock wave have a shorter mean free path and higher thermal velocity, leading to a higher collision frequency with greater collision energies. The translational energy is transferred through molecular collisions to the other internal energy modes, causing the excitation of these modes and disrupting the Boltzmann distribution.

After a sufficient number of molecular collisions, the populations over the energy levels in all the energy modes reach new Boltzmann distributions, achieving a new equilibrium state (State 2) at a temperature higher than State 1. This process is known as thermal relaxation.

During the thermal relaxation process, if the rovibrational energy mode of the molecules is excited to unbound energy levels, molecular dissociation occurs. When electronic energy is excited from bound to continuum states, ionization begins. Additionally, when intermolecular collision energies are high enough to overcome activation energies, exchange reactions between different chemical species can occur. These chemical reaction processes strongly correlate with thermal relaxation processes; thermal relaxation controls the chemical reaction rate, and vice versa.

Moreover, in the hypersonic flowfield around a planetary spacecraft, the thermochemical states of the gas in the fluid elements are likely to be in nonequilibrium. Because the fluid elements move very quickly, they pass through the shock layer surrounding the entry capsule before fully adjusting to the new equilibrium state corresponding to the internal energy increase across the shock wave.

Understanding these nonequilibrium atomic and molecular processes is crucial for accurately predicting the heat flux on entry capsules using theoretical and numerical approaches. Specifically, it is essential to model the thermal relaxation time and chemical reaction rates accurately. For a more detailed analysis that resolves non-Boltzmann population distributions, it is necessary to model state-to-state transition rates and state-specific dissociation rates.

1.2 Thermochemistry in Hypersonic Entry Flow for Mars Missions

1.2.1 Importance of O + CO_2 → O_2 + CO reaction

ESA is planning to launch ExoMars, a rover to explore the Martian surface, in 2028. That mission's primary objectives are to search for possible biosignatures of past life on Mars and to develop techniques for future sample return missions. Additionally, ESA has announced the selection of the EnVision mission as a future medium-class mission, targeting a launch in 2031. This mission aims to send an orbiter to Venus to investigate the divergent evolutionary paths of Earth and Venus. Notably, both Mars

and Venus have atmospheres primarily composed of carbon dioxide (CO_2).

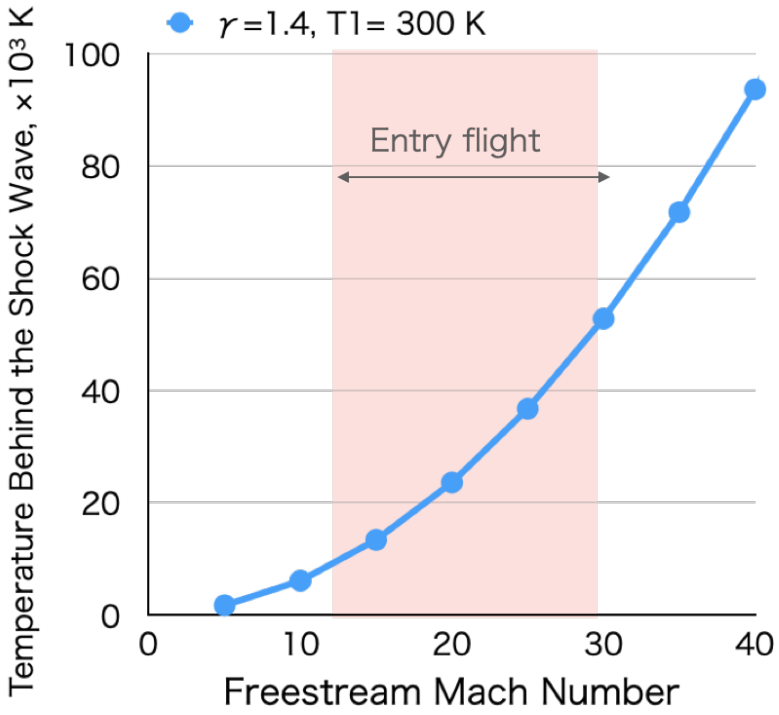

FIGURE 1.7 : Temperature behind the shock wave determined by Rankine-Hugoniot relation

The Martian atmosphere consists of approximately 95% CO_2, 2.8% N_2, and 2% Ar. The entry flight speed on Mars typically ranges from 5 to 10 km/s, corresponding to a Mach number between 20 and 40. Fig. 1.7 shows the relationship between the freestream Mach number and the temperature behind the shock wave according to the Rankine-Hugoniot relations. For Mach numbers between 12 and 30, the temperature behind the shock wave reaches several tens of thousands of Kelvin. Because radiative heat transfer is significant in this flight regime, an ablative Thermal Protection System (TPS) is necessary for the entry capsule.

Previous missions and their associated studies have identified C, CO, C_2, and CN as strong radiators, with intense radiation emitted from the nonequilibrium region behind the shock wave, where the thermal state of gases deviates from Boltzmann distribution. The wavelength of radiation is determined by the energy gap between states, while the intensity of the radiation is governed by the population of these energy states. Therefore, to accurately predict radiative heat transfer, it is essential to know the number densities at various energy levels, which necessitates state-resolved transition or reaction rate coefficients.

A recent study by Vargas highlighted the significant impact of the reaction $O + CO_2 \rightarrow O_2 + CO$ on the thermochemistry in the shock layer (Vargas et al., *J. Phys. Chem. A* **2021**, 125, 493–512). As shown in Fig. 1.8, there are variations in the experimental and

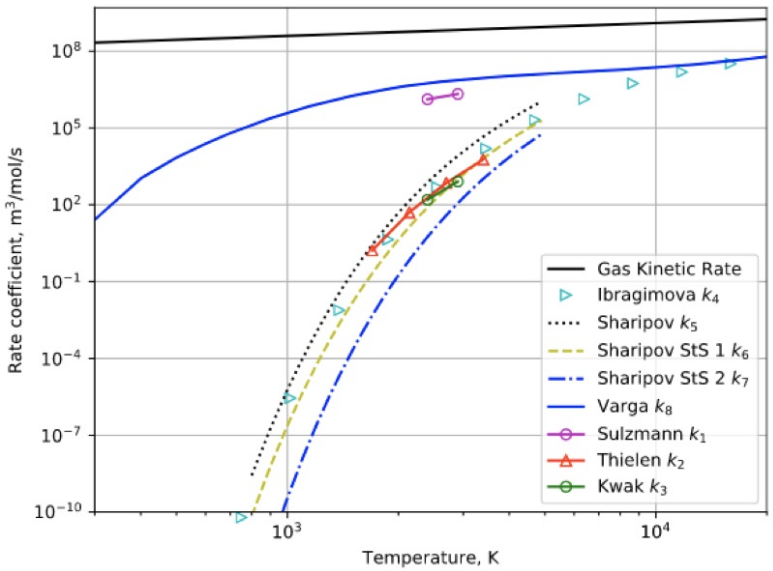

Figure 11. Exchange reactions $CO_2 + O \leftrightarrow CO + O_2$ found in some works in the literature plotted against the gas kinetic rate $CO_2 + O$ collision.

FIGURE 1.8 : Comparison of rate coefficients for the direct reaction $CO_2 + O \rightarrow CO + O_2$ (taken from VARGAS, J. et al. Heavy Particle Impact Vibrational Excitation and Dissociation Processes in CO_2. *The Journal of Physical Chemistry A* **2021**, *125*, 493-512)

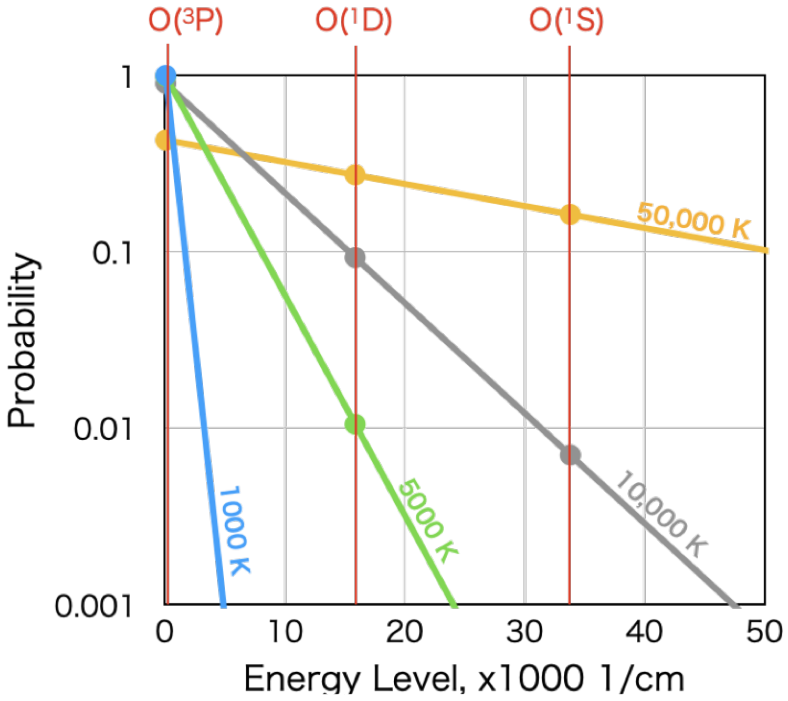

FIGURE 1.9 : Boltzmann distributions over electronic energy levels of O

theoretical results of reaction rate coefficients from past studies, leading to different CO_2 mole fraction profiles in the flow behind the shock wave. Therefore, it is expected that the reaction $O + CO_2 \rightarrow O_2 + CO$ is the one determining the thermal state of the gas, thus the radiation emission, in the nonequiliurbium region. Moreover, the effect of excited states involving this reaction must be examined, because the population of excited states, such as singlet D or singlet S of atomix oxygen, becomes non-negligible when the temperature exceeds 10,000 Kelvin, as shown in Fig. 1.9 illustrating the Boltzmann population distribution over the electronic energy levels of atomic oxygen.

Given this background, we are motivated to study the exchange reaction $O + CO_2 \rightarrow O_2 + CO$, which involves an intermediate in a form of CO_3. The CO_3 molecule has 22 valence electrons, and is considered inherently unstable because unpaired electrons remain; this corresponds to the requirement of the octet rule in the valence bond theory. The ground state of the neutral CO_3 molecule is expected to have a planar star-shape structure similar to the stable carbonate ion CO_3^{2-}, while the chain-shaped structure of CO_3 is expected to have higher energy due to strong electron localization. Compared to the star-shape structure, the chain-shape OCOO structure is expected to be ready to produce an O_2 structure for the topological reason, making it more probable intermediates in the reaction $O + CO_2 \rightarrow O_2 + CO$.

The energy gap between the triplet ground state and the first excited triplet state with the first excited state of O_2 molecule is 94.72 kJ/mol. The OCOO structure containing an O-O bond is expected to have several different states (spin and geometry),

that implies the presence of intersystem crossing and avoided crossing. Thus it is interesting to investigate the effects of interactions between the ground and excited states on the reaction $O + CO_2 \rightarrow O_2 + CO$.

For the reasons exposed in above, a global PES covering a wide range of energy is necessary when modeling this reaction using molecular dynamics methods such as QCT. Therefore, this study aims to explore the PES of both ground and excited states of CO_3 system to contribute the modeling of reaction kinetics in Martian entry flow from the perspective of computational quantum chemistry.

1.3 Modeling molecular processes

Because the flow around entry capsules is very fast, the molecular collision energies are very high, allowing the molecular systems to easily overcome activation energy through collisions. Under such conditions, the collision processes can be described by classical mechanics, as the quantum tunneling effects are insignificant. Hence, the Quasi-Classical Trajectory (QCT) simulation over a given potential energy surface (PES) is the most commonly used to model molecular processes in hypersonic flow fields.

In QCT simulations, the positions and velocities of atoms or molecules during a molecular collision are calculated by solving the classical equations of motion within an interatomic or intermolecular force field. The force field is determined by the gradient of the PES of the system. On the other hand, the initial and final energy states are treated quantum mechanically. These states are allocated to discrete rovibrational energy levels, which are determined by solving the Schrödinger equation. The state-to-state transition rates and state-specific dissociation rates are determined by statistically evaluating the collision integrals, which are derived from millions of trajectories calculated from various initial conditions.

The PES plays a critical role in QCT because it determines the interatomic and intermolecular forces, which ultimately govern the trajectories of the particles involved. Even in reactions between just two molecules, a PES that accurately represents the full range of interactions is essential. This includes both the long-range part where the molecules are far enough apart that intermolecular forces can be neglected, and the short-range part where they come close enough to form a single intermediate complex. The PES must capture both the global landscape and the local extrema (maxima and minima) with high resolution to ensure accurate simulations.

Furthermore, when a trajectory approaches a region where the PES of the ground state intersects or closely approaches that of an excited state, there is a possibility of a transitions between the ground and excited state. Therefore, identifying and characterizing the conical intersections made from the intersystem crossings between various PES's is also important. These intersections often govern the outcome of chemical reactions, particularly in photochemical processes, where the system can make transitions between different electronic states. In this point of view, the best known method to obtain the most accurate PES is the multi-reference configuration

interaction (MRCI) combined with the complete-active-space self-consistent-field (CASSCF) as used in this work.

1.4 Outline of this thesis

The objective of this study is to explore the PES of both ground and excited states of the CO_3 system to contribute to modeling the kinetics of the O + CO_2 →O_2 + CO reaction, which is significant in Martian entry flow, from the perspective of computational quantum chemistry. Toward this goal, Chapter 2 explores the simplest alkali dimer, Li_2, focusing on the excited states involving all types of bonding, i.e., resonant ionic, covalent, steric, and van der Waals interactions. This example was very useful to the author in learning about the quantum chemical calculations and in understanding the complex nature of the electronic states. Furthermore, this original work presents the relationship between different states not known before. This work also served the author to better analyse the nature of interactions involved in the electronic states in larger systems, such as CO_3. In Chapter 3, the PES's of the CO_3 system are explored using ab initio methods to investigate the possible reaction pathways for O + CO_2 → O_2 + CO, including the transition states and intermediates along these pathways. This chapter also examines the interactions between excited electronic states through multi-state electron configuration calculations. Using the reaction pathways obtained in Chapter 3, the reaction rates for O + CO_2 → O_2 + CO are determined by solving master equations in Chapter 4. Finally, the conclusion is presented in Chapter 5.

2 Complexity of the electronic excited states : Li_2 as example

As mentioned in the previous section, the CO_3 system is expected to have avoided crossings between the ground state and the excited states. To enhance understanding of the nature of interactions between the electronic states, this section explores the Li_2 system, the simplest alkali dimers, for molecular bonding in the excited states involving resonant ionic, covalent bonds, and steric interactions. The potential energy curves of $^1\Sigma_u^+$ states are calculated by Multi-Reference Configuration Interaction (MRCI) method using 13s8p5d3f Gaussian atomic basis functions by using MOLPRO program. The obtained PECs exhibit complex potential energy curves because the types of interactions vary as functions of the internuclear distance. For short bond lengths (less than 8 Bohr), the $2^1\Sigma_u^+$ state shows strong covalent bonding between the 3d and 2s atomic orbitals (AOs), forming the attractive part of the inner well. As the bond length increases, the 2p AO becomes involved in the bonding, which leads to a repulsive interaction around 12 Bohr. This change in bonding causes an avoided crossing between the (3d + 2s) and (2p + 2s) PECs, resulting in a local maximum near 10 Bohr that separates the inner and outer wells of the $2^1\Sigma_u^+$ state. The (2p + 2s) $^1\Sigma_u^+$ state makes a transition to a resonant ionic bonding configuration (Li^+/Li^- and Li^-/Li^+) at around 20 Bohr and then interacts with the covalent (3s + 2s) bonding, resulting in another avoided crossing. In the long lengths (greater than 20 Bohr), $2^1\Sigma_u^+$ state is made from (3s + 2s), which is expected to be more diffusive.

The spectroscopic constants are calculated by solving radial Schrödinger equation with the LEVEL16 program. The obtained spectroscopic constants for the inner and outer wells of both $2^1\Sigma_u^+$ and $3^1\Sigma_u^+$ agree well with the experimental data. Furthermore, new spectroscopic constants for the $4^1\Sigma_u^+$ and $5^1\Sigma_u^+$ states are reported.

Following article

AHN FURUDATE, M. et al. Resonant Ionic, Covalent Bond, and Steric Characteristics Present in $1\Sigma_u^+$ States of Li_2. *Molecules* **2022**, *27*, 3514

molecules

MDPI

Article

Resonant Ionic, Covalent Bond, and Steric Characteristics Present in $^1\Sigma_u^+$ States of Li_2

Michiko Ahn Furudate [1], Denis Hagebaum-Reignier [2,*], Jin-Tae Kim [3,*] and Gwang-Hi Jeung [2]

[1] Department of Mechatronics Engineering, Chungnam National University, Daejeon 34134, Korea; furu@cnu.ac.kr
[2] Aix Marseille Univ, CNRS, Centrale Marseille, iSm2, 13007 Marseille, France; gwang-hi.jeung@univ-amu.fr
[3] Department of Photonic Engineering, Chosun University, Gwangju 61452, Korea
* Correspondence: denis.hagebaum-reignier@univ-amu.fr (D.H.-R.); kimjt@chosun.ac.kr (J.-T.K.)

Abstract: The molecular bonding in the excited states of the alkali dimers involves the resonant ionic, covalent bond and steric interactions. We show here the case of the $^1\Sigma_u^+$ states of Li_2 by ab initio calculation. These interactions as functions of the internuclear distance lead to complex potential energy curves, providing an important application for high resolution laser spectroscopy. The spectroscopic constants for the 4 and 5 $^1\Sigma_u^+$ states are obtained for the first time.

Keywords: resonant ionic; $^1\Sigma_u^+$ states of Li_2; potential energy curves; spectroscopic constants

check for updates

Citation: Ahn Furudate, M.; Hagebaum-Reignier, D.; Kim, J.-T.; Jeung, G.-H. Resonant Ionic, Covalent Bond, and Steric Characteristics Present in $^1\Sigma_u^+$ States of Li_2. *Molecules* **2022**, *27*, 3514. https://doi.org/10.3390/molecules27113514

Academic Editor: Daniel Escudero

Received: 7 April 2022
Accepted: 19 May 2022
Published: 30 May 2022

Publisher's Note: MDPI stays neutral with regard to jurisdictional claims in published maps and institutional affiliations.

Copyright: © 2022 by the authors. Licensee MDPI, Basel, Switzerland. This article is an open access article distributed under the terms and conditions of the Creative Commons Attribution (CC BY) license (https://creativecommons.org/licenses/by/4.0/).

1. Introduction

The molecular bonding between atoms is classified according to its characteristics into three main types of bonds; namely, the covalent bonding, ionic bonding, and Van der Waals bonding. Former two types are present for relatively short internuclear distances and there also exists intermediate type of bonding that has both partially covalent and partially ionic characters. In contrast, the Van der Waals type is concerned for larger distances and is often disqualified as chemical bonding but is counted as a physical bonding. In the case of homopolar dimers, another type of ionic bonding exists, namely the resonant ionic bonding, where the time-averaged dipole moment is zero but the instantaneous one is non-zero [1].

Colliding atoms can also repulse each other without making a chemical bonding due to the steric repulsion as in the example of the rare gas atoms or between closed-shell molecules (N_2, O_2, etc.). The steric repulsion is strong enough at room temperature to impede the formation of Van der Waals complex. In the case of the excited states of Rydberg type, the steric repulsion concerns an interaction between a valence orbital and a Rydberg orbital. As the latter has a diffuse electron distribution, the repulsion is much weaker than between the valence orbitals. However, the strength of the repulsion decreases slowly for large internuclear distance and shows undulating property, as was shown in some diatomics [2].

Some experimental and theoretical studies on highly excited electronic states of Li_2 of Rydberg character have been reported [3–14]. Such states were also used to probe lower-lying states [14]. As has been commented in those works, it is difficult to find the correlation between the molecular states and the atomic asymptotes as many more molecular states can be made from a given atomic states and many avoided crossings occur due to the high density of states. The energy levels of the molecular states are also difficult to anticipate as the molecular bond energies differ much according to the point group symmetry and also depend on the atomic orbitals involved. The Rydberg character has been initially defined for the atomic states as one made from the principal quantum number greater than that of the ground state. In forming a diatomic molecule, the atomic orbitals from both atoms are all mixed up resulting in a difficulty of defining the Rydberg character. In the case of Li_2, there are also many states made from (2p + 2p) that interact with other states. This can

2 Complexity of the electronic excited states : Li_2 as example

be seen from a recent theoretical calculation of some Rydberg states [14] where subtleties related to deriving quantum defects were presented. It is apparent that no simple model without complication can give molecular energy levels. As a consequence, it is not evident to identify the atomic asymptote for an unknown electronic state that lies far above the ground state.

In the excited states, as the electronic energy is much higher than in the ground state, it is easier for the electron to be ionized. It makes the resonant ionic state much more probable, where two forms, Li^+/Li^- and Li^-/Li^+, have the equal probability to exist. Due to the symmetry reason, this can happen for the $^1\Sigma^+$ states in Li_2. The resonant ionic state is diabatically correlated to the asymptotic energy that is the difference between the ionization potential (IP) and the electronic affinity (EA) of the Li atom, IP−EA. On the first approximation, the potential energy as a function of the internuclear distance (R), i.e., potential energy curve (PEC), of such resonant ionic state would be IP−EA−1/R + SR, where SR is the steric repulsion term between the two cores in the $1s^2$ state of the Li atom.

Among these excited states, the second singlet state of $\Sigma_u{}^+$ symmetry, hereafter named $2\ ^1\Sigma_u{}^+$, has attracted attention of both experimentalists and theoreticians due to the presence of two wells in its potential curve. This unusual potential shape was already predicted theoretically in the early 1980′s by Konowalow and Fish effective core potential calculation [3]. Further high-resolution spectroscopic studies showed the survival of up to eight vibrational states in the inner well and some vibrational states of the outer well could also be detected due to tunneling effects [8]. The present work revisits the origin of the double-well potential of the $2^1\Sigma_u{}^+$ and presents more general properties of the excited electronic states that this state appears to share. We also give here the spectroscopic constants for the 4 and 5 $^1\Sigma_u{}^+$ states for the first time that could be a good guide for the precision spectroscopic measurements in energy in future.

2. Method of Computation

The basis set used in this work includes 13s8p5d3f Gaussian atomic basis functions. It was taken from the 15s10p6d3f functions previously described [2]. This basis was specially made to well represent high-lying excited states up to 6s + 2s asymptotic state of Li_2.

In this basis set, the most diffuse two s-type functions cause the linear dependence problem for short internuclear distance, resulting from the large overlap integrals between such diffuse s-type functions. So, we had to use different basis sets, with and without these two, to compare the resulting energy (see below in this section). The most diffuse two p-type functions and 1 d-type functions were also tested with and without, as the atomic asymptotes we report here, (3s + 2s), (3p + 2s) and (3d + 2s), are very well described with the truncated basis set. We have used MOLPRO [15] program packages for the molecular calculation. In the multi-configuration (MC) self-consistent-field (SCF) calculations, we have used four σ_g, four σ_u, one π_g, one π_u molecular orbitals (Mos) in the valence active space. In the multi-reference (MR) configuration interaction (CI) calculations, we have used all single and double excitations from the MC-SCF active space. The four core electrons were also allowed to make all possible single and double substitutions. In all, 250,549 configuration state functions (CSFs) were generated for the $^1\Sigma_u{}^+$ states.

Transition dipole moments from $n^1\Sigma_u{}^+$ states to the ground state $X^1\Sigma_g{}^+$ are also calculated by MOLPRO. To calculate the PEC of the ground state, we have used the basis set and the active space consistent with those for n $^1\Sigma_u{}^+$ mentioned above.

From computed potential energy curves for n $^1\Sigma_u{}^+$ states, we have determined vibrational levels for each electronic state by using the LEVEL16 program [16]. This program solves the radial Schrodinger equation for an input PEC, and outputs bound and/or quasi-bound levels, and eigenfunctions and various constants for those levels.

3. Results and Discussion

The PECs for the second, third, fourth, and fifth $^1\Sigma_u{}^+$ states are reported in Figure 1. The energy scale in these figures is with respect to the dissociation limit of the ground state

(2s + 2s). To obtain the transition energy from the ground state molecule one has to add the ground state dissociation energy (D_e), 8517 cm^{-1} [17]. Here, T_e is the potential energy difference between the minimum of the ground state and the minimum of the excited state. That should not be confounded with T_0, which is the potential energy difference between the lowest vibrational level of the ground electronic state and the lowest vibrational level of the excited electronic state. We can see here that the second state (2 $^1\Sigma_u^+$) has two potential wells. The inner well of 2 $^1\Sigma_u^+$ is made from the covalent bonding of (3d + 2s) while the outer well is made from (3s + 2s). The 3dσ atomic orbital (AO) is more directed along the internuclear axis, so it can make more efficient bonding with 2s AO in comparison with much more diffuse 3s AO. As a result, the bond strength of (3d + 2s) is much larger than (3s + 2s). In the intermediate distance between these two, from around 10 Bohr to the bottom of the outer well, 2p AO takes part in the bonding, corresponding to the repulsive part of (2p + 2s) $^1\Sigma_u^+$. All those changes result in the avoided crossing between the two potential wells, thus making atypical PEC with double well. This state becomes resonant ionic at around 20 Bohr and this part of PEC is a result of the avoided crossing between the covalent (3s + 2s) bond and the resonant ionic (Li^+/Li^- and Li^-/Li^+) bond.

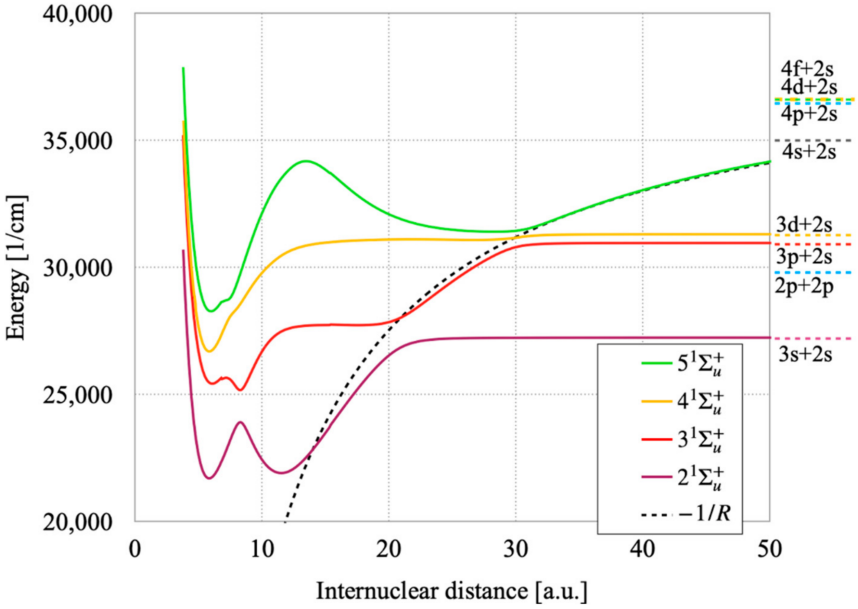

Figure 1. Potential energy curves of the 2, 3, 4 and 5 $^1\Sigma_u^+$ states of $^7Li_2$.

In the case of the third state (3 $^1\Sigma_u^+$), three kinds of bonds, (3s + 2s), (3p + 2s) and (3d + 2s), interfere to make a very strange PEC with double well. An avoided crossing between (3p + 2s) and the resonant ionic bonds occurs around 30 Bohr.

Table 1 shows the critical points, potential well (maxima, M), potential barrier (minima, m) and inflection points (i), resulted in two different basis sets, one with the two diffuse s-type Gaussian functions, and another one without them. We can see here that the differences in distance and relative energy are very small for the 2 $^1\Sigma_u^+$ and 3 $^1\Sigma_u^+$ states. For the 4 $^1\Sigma_u^+$ state, however, the potential well depth (m) differs by about 200 cm^{-1}. We have connected PECs from this smaller basis set (13s8p5d3f) to the corresponding PECs from the full basis (15s10p6d3f) at the interatomic distance of 5.3 Bohr. To make smooth connections, each PEC from the smaller basis set is shifted to have the same minimum energy values at the same interatomic distance as the corresponding state PECs from the full basis set.

Table 1. Critical points (maxima M, minima m, inflection i, asymptote a), of the electronic states calculated in this work.

Basis		**15s10p6d3f**		**13s8p5d3f**	
States		**R (a.u)**	**E (cm^{-1})**	**R (a.u)**	**E (cm^{-1})**
$5\,^1\Sigma_u^+$	m	6.00	28,271	6.000	28,298
	i	6.925	28,657		
	i	7.175	28,702		
	i	8.525	30,098		
	M	13.50	34,177		
	i	16.125	33,428		
	m	28.35	31,404		
	i	33.30	31,924		
	a	100	35,030		
	a (ex)	∞ (4s + 2s)	35,012		
$4\,^1\Sigma_u^+$	m	5.849	26,693	5.830	26,885
	i	7.025	27,595		
	i	7.775	28,236		
	i	8.725	28,891		
	a	100	31,302		
	a (ex)	∞ (3d + 2s)	31,283		
$3\,^1\Sigma_u^+$	m	6.091	25,424	6.099	25,439
	i	6.925	25,622		
	M	7.184	25,652		
	i	7.875	25,359		
	m	8.281	25,170	8.311	25,251
	i	9.075	25,779		
	i	14.95	27,727		
	M	15.40	27,748		
	i	16.00	27,740		
	m	17.55	27,723		
	i	23.35	28,834		
	a	100	30,961		
	a (ex)	∞ (3p + 2s)	30,925		
$2\,^1\Sigma_u^+$	m	5.844	21,697	5.843	21,702
	i	7.375	23,039		
	M	8.300	23,904		
	i	9.025	23,346		
	m	11.526	21,904	11.505	21,937
	i	15.725	23,976		
	a	100	27,237		
	a (ex)	∞ (3s + 2s)	27,206		

The fourth state ($4\,^1\Sigma_u^+$) has a single well perturbed by the upper lying states, at the outer part of the well around 8 Bohr, as can be seen in the inflection points in Table 1. The fifth state ($4\,^1\Sigma_u^+$) shows a potential barrier around the maximum at 13.5 Bohr. It is due to an avoided crossing between the repulsive 3d + 2s and higher lying state.

The transition dipole moments (TDMs) from the ground state to these $^1\Sigma_u^+$ states as functions of the internuclear distance (R) are shown in Figure 2. We can better understand the changing molecular electronic eigenfunctions with respect to R by comparing Figures 1 and 2. For the $2\,^1\Sigma_u^+$ state, the TDM goes to zero at around 9 Bohr where 3d AO is predominant, as the 3d-2s transition is dipole forbidden. One can also see a large TDM around 12 Bohr where the 2p AO takes part in the bonding. For larger distances, the TDM rapidly vanishes where the resonant ionic configuration becomes predominant then the asymptotic neutral configuration (3s + 2s) replaces the former.

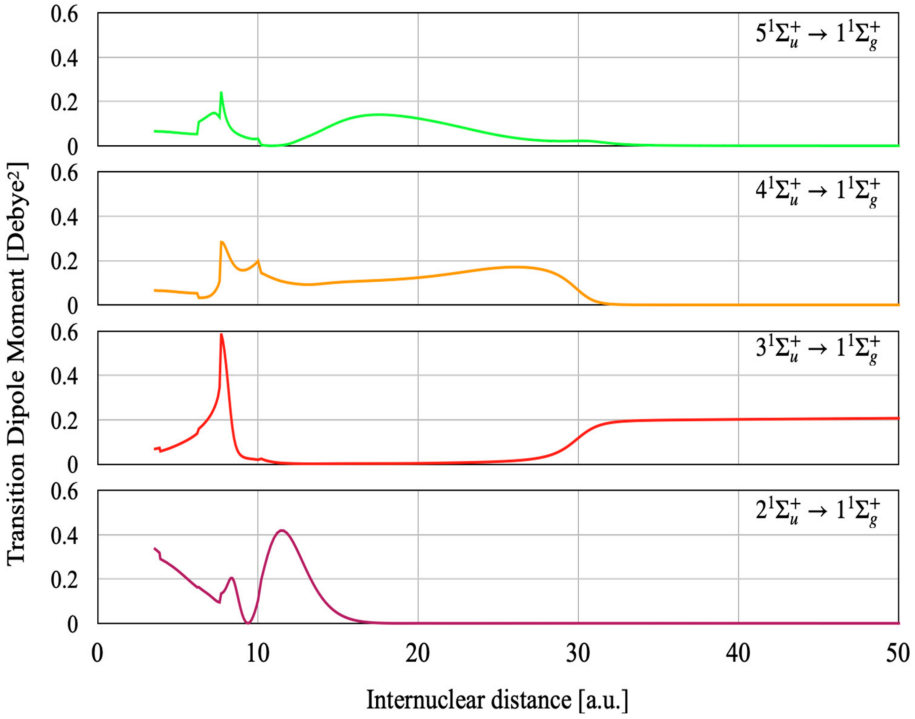

Figure 2. Transitional dipole moment (Squared) from the ground state to the $^1\Sigma_u^+$ states.

For the $2^1\Sigma_u^+$ state, there is a perfect concordance between the PEC and TDM around R = 15 Bohr, where the resonant ionic configuration relays the mixed valence configuration. Indeed, the TDM decreases to zero for R between 15 and 20 Bohr as the $2^1\Sigma_u^+$ state is resonant ionic. For the resonant ionic state, each atom can be described as $2s^2/2$ and the $(2s^2/2)$ -2s transition is dipole forbidden. For R > 20 Bohr, the TDM remains zero as the $2\ ^1\Sigma_u^+$ state becomes 3s + 2s, the 3s-2s being forbidden. The TDM of the $3^1\Sigma_u^+$ state remains zero for a large domain of R values because this state correlates to the 3s + 2s dissociation asymptote for R < 20 Bohr. The $3\ ^1\Sigma_u^+$ state becomes resonant ionic at around 20 Bohr, so its TDM remains zero between 20 and 30 Bohr. For R > 30 Bohr, this state becomes 3p + 2s and its TDM converges to the 3p-2s value. The TDM of $4\ ^1\Sigma_u^+$ converges to zero for R > 0 Bohr, as it corresponds to the 3d-2s atomic transition that is dipole forbidden. The TDM of the $5\ ^1\Sigma_u^+$ state converges to zero for R > 32 Bohr as it corresponds to resonant ionic part. The $5\ ^1\Sigma_u^+$ state dissociates into 4s + 2s, so its TDM remains zero for R corresponding to dissociation.

The vibrational levels obtained from the LEVEL16 program for $2\ ^1\Sigma_u$ state are summarized in Table 2 and compared with Kasahara's experimental and semi-classical results [8]. As shown in Figure 3 Kasahara's potential curve in the inner well and the barrier regions matches well with one calculated by us. The lowest three levels in the inner well are in good agreement with Kasahara's values; the error is within the spectroscopic accuracy. As the level increase, the error increases up to about 8 cm^{-1}. For the outer well, we made the correspondence of the outer well vibrational levels in two works considering the relations of vibrational levels in the inner and outer wells from the plot of wave functions in Kasahara's work [8] and the present work (Figure 4). The upper vibrational levels in the present study agree reasonably with Kasahara's values and the differences within 9 cm^{-1}. However, the difference is significant in the lower levels. Our outer potential well is lower than that of Kasahara's by about between 59 cm^{-1} and 81 cm^{-1}. With the increases of internuclear distance the differences are becoming larger. This disparity may be originated from the adjustment made by Kasahara et al. Indeed, they have obtained the vibrational levels from the PEC optimized to fit their experimental term values by the inverted perturbation approach (IPA) [18]. As the initial outer PEC for the IPA, they used the theoretical PEC of

Schmidt-Mink [4], and the curve was shifted up by about 35 cm^{-1} to roughly reproduce the experimentally determined vibrational levels near the local maximum. Since experimental data to optimize the outer well is available only for a few levels near the local maximum, the accuracy of the PEC for the lower part of the outer well would be less reliable, as they have mentioned in their work.

Table 2. Vibrational energy levels of 2 $^1\Sigma_u^+$ (J = 0) of $^7Li_2$.

$2^1\Sigma_u^+$ (J = 0) Inner Well							
	G_v (cm^{-1})				B_v (cm^{-1})		
v_i	Present	v_i	Kasahara	Present-Kasahara	Present	Kasahara	Present-Kasahara
0	129.0231	**0**	129.0751	−0.0520	0.49949	0.49865	0.00084
1	384.0727	**1**	384.1343	−0.0616	0.49330	0.49232	0.00098
2	634.7832	**2**	634.9956	−0.2124	0.48671	0.48587	0.00084
3	880.0632	**3**	881.4854	−1.4222	0.47933	0.47924	0.00009
4	1119.3332	**4**	1123.3140	−3.9808	0.47200	0.47231	−0.00031
5	1354.0883	**5**	1359.9908	−5.9025	0.46547	0.46490	0.00057
6	1583.9713	**6**	1590.6952	−6.7239	0.45733	0.45670	0.00063
7	1806.1984	**7**	1814.0597	−7.8613	0.43857	0.44691	−0.00834
8	2019.1734	**8**	2026.9763	−7.8029	0.39926	0.38556	0.01370
$2^1\Sigma_u^+$ (J = 0) Outer Well							
	G_v (cm^{-1})				B_v (cm^{-1})		
v_o	Present	v_o	Kasahara	Present-Kasahara	Present	Kasahara	Present-Kasahara
0	266.2942		-	-	0.12910	-	-
1	383.2602	**0**	361.8034	21.4568	0.12901	0.13129	−0.00125
2	499.2858	**1**	483.0413	16.2445	0.12891	0.13061	−0.00131
3	614.2992	**2**	603.7395	10.5597	0.12879	0.13016	−0.00153
4	728.3109	**3**	722.3377	5.9732	0.12868	0.13010	−0.00180
5	841.2961	**4**	839.1467	2.1494	0.12856	0.13021	−0.00248
6	953.2471	**5**	953.5825	−0.3354	0.12846	0.13036	−0.00349
7	1064.1449	**6**	1065.6593	−1.5144	0.12836	0.13094	−0.00427
8	1173.9686	**7**	1175.8812	−1.9126	0.12829	0.13185	−0.00433
9	1282.6964	**8**	1285.0167	−2.3203	0.12825	0.13256	−0.00362
10	1390.3004	**9**	1393.7730	−3.4726	0.12826	0.13258	−0.00272
11	1496.7460	**10**	1502.0048	−5.2588	0.12832	0.13188	−0.00237
12	1601.9835	**11**	1608.7631	−6.7796	0.12848	0.13104	−0.01001
13	1705.9445	**12**	1713.5840	−7.6395	0.12878	0.13085	0.00548
14	1808.6007	**13**	1816.8750	−8.2743	0.13818	0.13879	−0.04630
15	1909.5915	**14**	1918.2592	−8.6677	0.13042	0.13270	0.02033
16	2007.7026	**15**	2015.4642	−7.7616	0.16340	0.17672	−0.08919
17	2105.6652	**16**	2112.3711	−6.7059	0.14045	0.14307	−0.00160
		17	2193.0165	-	-	0.22964	-

Our spectroscopic constants such as R_e, T_e, B_e, α_e, ω_e, $\omega_e x_e$ of the inner and outer wells of the 2 $^1\Sigma_u^+$ state as shown in Table 3 are closer to Musiał et al.'s experimental ones. Spectroscopic constant T_e in other publications gave a large difference of around 300 cm^{-1}, as can be seen in Table 3, although all of previous reported constants except α_e agree within ~1%. Our spectroscopic constants for the inner and outer wells of the 3 $^1\Sigma_u^+$ state as shown in Table 3 are also closer to Musiał et al.'s experimental ones. In Table 4, one can see that our spectroscopic constants fitted for the 2 $^1\Sigma_u^+$ state using Dunham polynomials match well with those of Kasahara et al.

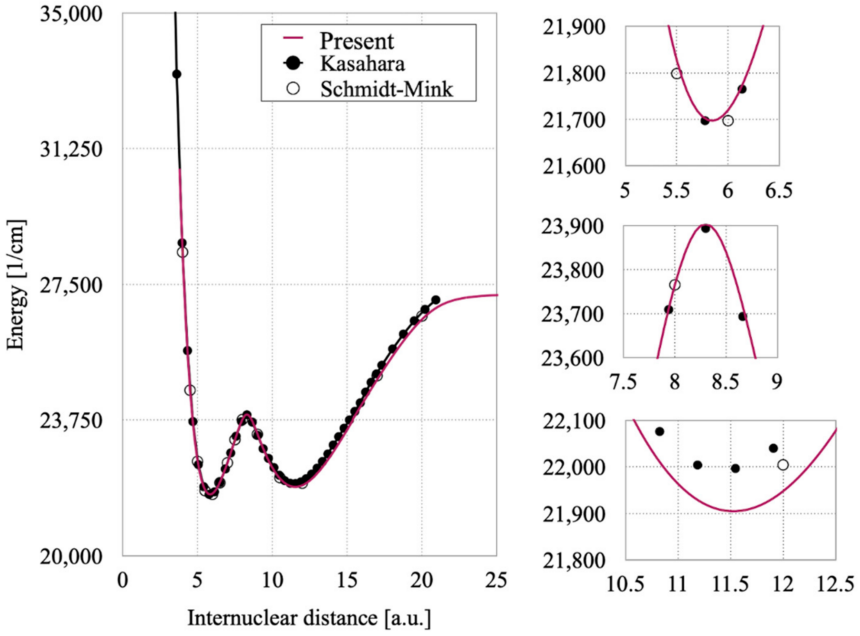

Figure 3. Comparisons of the potential curves of the 2 $^1\Sigma_u^+$ state between the present work and previously published results (**left**) with three close-up figures (**right**).

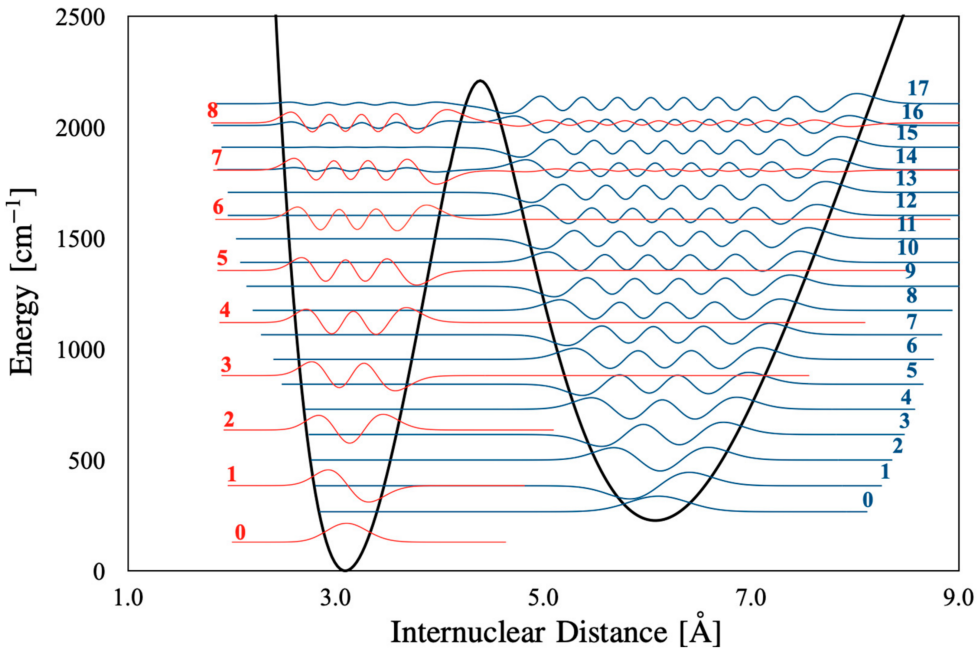

Figure 4. The eigenfunctions of vibrational levels v = 0–16 (v_i = 0–8 and v_o = 0–17) for $2^1\Sigma_u^+$ (J = 0). The amplitudes are magnified by a factor of 50.

We have new spectroscopic constants for the 4 $^1\Sigma_u^+$ and 5 $^1\Sigma_u^+$ states in Table 4 that could serve as a guide to the future experimental observation using far UV photons with short wavelengths. Especially, the 5 $^1\Sigma_u^+$ state has a wide potential barrier so that the experimental observation of this state will be a challenging task.

Table 3. Spectroscopic constants of 2, 3, 4 and 5 $^1\Sigma_u^+$ states of $^7Li_2$.

State		R_e (Å)	D_e (cm^{-1})	T_e (cm^{-1})	B_e (cm^{-1})	α_e (cm^{-1})	ω_e (cm^{-1})	$\omega_e x_e$ (cm^{-1})
$2^1\Sigma_u^+$ Inner	Present	3.092	5540	29,986.74	0.502	0.0052	258.7	1.60
	Kim [14]	3.078	5702.6	30,144.3	0.507	0.0062	259.7	2.01
	Lee [12]	3.125	5568	29,653				
	Musial [13]	3.093	5608	30,044			260	
	Jasik [9]	3.081	5674.0	30,094.0			259.82	
	Linton [5]	3.094		30,100.3	0.502	0.0066	259.9	2.23
	Exp. [8]	3.096		30,101.407	0.502	0.0062	259.003	1.71
$2^1\Sigma_u^+$ Outer	Present	6.100	5333	30,194.00	0.129	4.978×10^{-5}	117.9	0.4579
	Lee [12]	6.072	5367	29,853				
	Musial [13]	6.088	5389	30,261			118	
	Jasik [9]	6.072	5413	30,285			119.05	
	Exp. [8]	6.037		30,400.137				
$3^1\Sigma_u^+$ Inner	Present	3.223	5537	33,713.25	0.465	0.0248	188.9	-
	Lee [12]	3.288	5663	33,300				
	Musial [13]	3.250	5628	33,762			193	
$3^1\Sigma_u^+$ Outer	Present	4.382	5791	33,460.00	0.249	−0.0033	272.9	-
	Kim [14]	4.351	5894	33,669.8			304.0	
	Lee [12]	4.384	5872	33,091			306	
	Musial [13]	4.360	5874	33,512				
	Jasik [9]	4.369	5854	33,668.0			295.3	
$4^1\Sigma_u^+$	Present	3.095	4663	34,982.61	0.4993	0.00250	262.4	6.6591
$5^1\Sigma_u^+$	Present	3.173	6759	36,554.79	0.4775	0.0106	228.6	2.4409

Table 4. Spectroscopic constants of 2, 3, 4 and 5 $^1\Sigma_u^+$ states of $^7Li_2$ for Dunham expression.

State	$2^1\Sigma_u^+$ Inner		$2^1\Sigma_u^+$ Outer
	Present	Kasahara	Present
v_{max}	4		13
j_{max}	6		6
Err_{max}	5.789×10^{-2}		4.336×10^{-2}
RMS	4.898×10^{-3}		2.794×10^{-3}
Y_{00}	0.04751	0.1101	207.5
Y_{10}	258.762	259.003	117.9
Y_{20}	−1.606	−1.7124	−0.4579
Y_{30}	-1.386×10^{-1}	-1.811×10^{-1}	-3.774×10^{-3}
Y_{01}	0.5031	0.5016	0.1289
Y_{11}	-6.896×10^{-3}	-6.247×10^{-3}	-4.9781×10^{-5}

There is one peculiarity in the PEC of the 5 $^1\Sigma_u^+$ state. This state should be converging to the 3s + 2s asymptote before meeting the resonant ionic state at large distance (at about 25 Bohr). So one might expect the PEC from about 10 Bohr to 25 Bohr to remain below the 3s + 2s asymptote. However, it is not the case. In fact, the potential energy between 10.8 Bohr to 17.4 Bohr (see Table 1) remains significantly higher than the asymptote, by 478 cm^{-1} at the top of the barrier according to our calculation. We think this may be caused by the steric repulsion between 3s and 2s atomic orbitals (AOs). Figure 5 shows the overlap integrals between 2s/2s, 3s/2s, 4s/2s and 5s/2s. The overlap between 2s/2s increases as the internuclear distance (R) becomes small, while that of 3s/2s has one maximum, 4s/2s two maxima, and 5s/2s three maxima, due to the nodal structure of the AO. For a given R, the magnitude of the overlap decreases rapidly in the order of 2s/2s/, 3s/2s, 4s/2s and 5s/2s, as the amplitude of excited AOs decrease according to the degree of excitation. The steric repulsion is approximately a function of the amplitude of the overlap integral, so the former behaves similar to the latter.

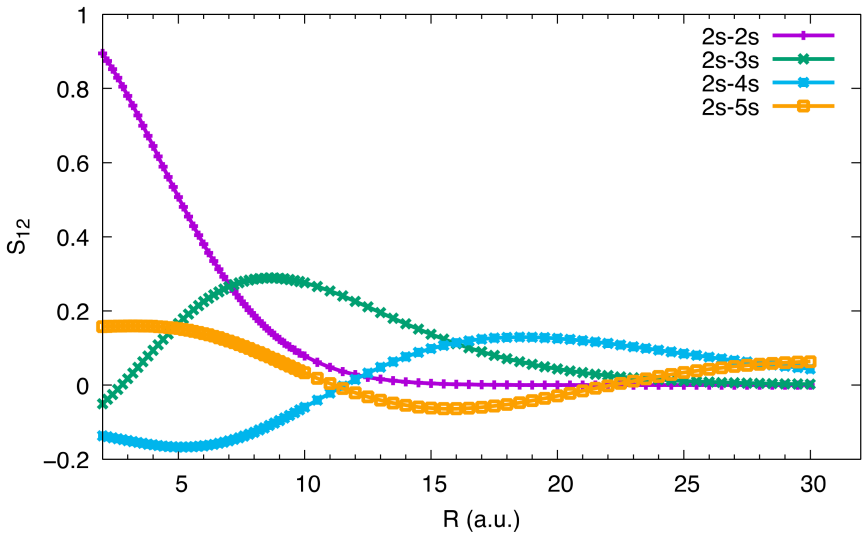

Figure 5. Overlap integrals between ns and 2s atomic orbitals as functions of R.

As other effects, in particular the reorganization of the electron distribution in forming the molecule due to the presence of other core ($1s^2$), the correlation effect between the two electrons, intervene apart from the steric repulsion, it is not easy to attribute one contribution for the peculiarity mentioned above. In the case where the interatomic bonding is not strong, one can better see the oscillating PEC as has been reported before [2,19]. There are other states, e.g., the excited $^1\Sigma_g{}^+$ states of Li_2 and in other alkali dimers, that show the same aspect.

4. Conclusions

The potential energy curves (PECs) for the second, third, fourth, and fifth $^1\Sigma_u{}^+$ states calculated in this work show all essential features of the excited electronic states: covalent contribution, resonant ionic contribution and the steric contribution. These three contributions appear in different domains of the internuclear distance and in different levels of the potential energy. As the excited atomic orbitals becomes more diffuse as the degree of excitation increases, all three contributions extend to larger nuclear distance. The avoided crossings for the highly excited states appearing at relatively short internuclear distances are caused by the interaction between different components of the covalent bonding, attractive and repulsive. As the resonant ionic contribution behaves approximately according to $-1/R$, the perturbation caused by this contribution appears at larger distances as the degree of electronic excitation increases. The steric repulsion shows undulating behavior due to the radial part of the atomic orbital density for the excited state, and that is reflected at large internuclear distance. The case of the $^1\Sigma_u{}^+$ states shown in this work illustrate very well the complexity of the potential energy curves and the nature of electronic functions. New spectroscopic constants for the 4 and 5 $^1\Sigma_u{}^+$ states as well as transition dipole moments from the ground state to the $^1\Sigma_u{}^+$ states as functions of the internuclear distance are reported in this work for the first time, too.

Author Contributions: Formal analysis, resources and data curation, M.A.F.; visualization, M.A.F. and D.H.-R.; writing—original draft preparation, M.A.F., G.-H.J. and J.-T.K.; investigation, M.A.F., G.-H.J. and D.H.-R.; conceptualization, validation, writing—review and editing, M.A.F., G.-H.J., J.-T.K. and D.H.-R.; supervision and project administration, G.-H.J. and D.H.-R. All authors have read and agreed to the published version of the manuscript.

Funding: This work was partially supported by Brain Pool Program through the National Research Foundation of Korea (NRF) funded by the Ministry of Science and ICT (2020H1D3A2A01103751). This work was also partially supported by the National Research Foundation of Korea (NRF) grant funded by the Korea government (MSIT) (No. NRF-2020R1A2C1010994).

Institutional Review Board Statement: Not applicable.

Informed Consent Statement: Not applicable.

Acknowledgments: M.A.-F. thanks Aix-Marseille University for hosting.

Conflicts of Interest: The authors declare no conflict of interest.

References

1. Jeung, G.-H.; Ross, A.J. Electronic structure of the lowest $^{1,3}\Sigma_g^+$, $^{1,3}\Sigma_u^+$, $^{1,3}\Pi_g$, $^{1,3}\Pi_u$, $^{1,3}\Delta_g$ and $^{1,3}\Delta_u$ states of K_2 from valence CI calculations. *J. Phys. B At. Mol. Opt. Phys.* **1988**, *21*, 1473–1487. [CrossRef]
2. Yiannopoulou, A.; Jeung, G.-H.; Park, S.J.; Lee, H.S.; Lee, Y.S. Undulations of the potential-energy curves for highly excited electronic states in diatomic molecules related to the atomic orbital undulations. *Phys. Rev. A* **1999**, *59*, 1178–1186. [CrossRef]
3. Konowalow, D.D.; Fish, J.L. The molecular electronic structure of the twenty-six lowest lying states of Li_2 at short and intermediate internuclear separations. *Chem. Phys.* **1984**, *84*, 463–475. [CrossRef]
4. Schmidt-Mink, I.; Müller, W.; Meyer, W. Ground- and excited-state properties of Li_2 and Li_2^+ from ab initio calculations with effective core polarization potentials. *Chem. Phys.* **1985**, *92*, 263–285. [CrossRef]
5. Linton, C.; Martin, F.; Bacis, R.; Vergès, J. Observation and analysis of the $2\,^1\Sigma_u^+$ "double minimum" state of Li_2. *J. Mol. Spectrosc.* **1989**, *137*, 235–241. [CrossRef]
6. Poteau, R.; Spiegelmann, F. Calculation of the Electronic Spectrum of Li_2 Using Effective Core Pseudopotentials and l -Dependent Core Polarization Potentials. *J. Mol. Spectrosc.* **1995**, *171*, 299–308. [CrossRef]
7. Ross, A.J.; Crozet, P.; Linton, C.; Martin, F.; Russier, I.; Yiannopoulou, A. On the $5d^1\Pi_g \rightarrow 2^1\Sigma^+{}_u$ and $5d^1\Pi_g \rightarrow C^1\Pi_u$Fluorescence in $^7Li_2$. *J. Mol. Spectrosc.* **1998**, *191*, 28–31. [CrossRef] [PubMed]
8. Kasahara, S.; Kowalczyk, P.; Kabir, H.; Baba, M.; Katô, H. Doppler-free UV-visible optical–optical double resonance polarization spectroscopy of the $2\,^1\Sigma_u^+$ double minimum state and the $C^1\Pi_u$ state of Li_2. *J. Chem. Phys.* **2000**, *113*, 6227–6234. [CrossRef]
9. Jasik, P.; Sienkiewicz, J.E. Calculation of adiabatic potentials of Li_2. *Chem. Phys.* **2006**, *323*, 563–573. [CrossRef]
10. Jędrzejewski-Szmek, Z.; Grochola, A.; Jastrzebski, W.; Kowalczyk, P. The $5^1\Pi_u$ electronic state of the lithium dimer. *Chem. Phys. Lett.* **2007**, *444*, 229–231. [CrossRef]
11. Grochola, A.; Kowalczyk, P.; Jastrzebski, W. Rydberg states of the Li_2 molecule studied by polarization labelling spectroscopy. *J. Phys. B At. Mol. Opt. Phys.* **2010**, *43*, 155102. [CrossRef]
12. Lee, C.-W. Study of the Valence and Rydberg States of a Lithium Dimer by the Multi-reference Configuration-interaction Method, *Bull. Korean Chem. Soc.* **2014**, *35*, 1422–1432. [CrossRef]
13. Musiał, M.; Kucharski, S.A. First Principle Calculations of the Potential Energy Curves for Electronic States of the Lithium Dimer. *J. Chem. Theory Comput.* **2014**, *10*, 1200–1211. [CrossRef] [PubMed]
14. Kim, H.-J.; Lee, C.-W. Rydberg series of $^1\Sigma_u^+$ and $^1\Delta_u$ states of the Li_2 molecule studied by the promotion model. *J. Phys. B At. Mol. Opt. Phys.* **2015**, *48*, 015101. [CrossRef]
15. Werner, H.-J.; Knowles, P.J.; Knizia, G.; Manby, F.R.; Schütz, M. Molpro: A general-purpose quantum chemistry program package. *WIREs Comput. Mol. Sci.* **2012**, *2*, 242–253. [CrossRef]
16. Le Roy, R.J. LEVEL: A computer program for solving the radial Schrödinger equation for bound and quasibound levels. *J. Quant. Spectrosc. Radiat. Transf.* **2017**, *186*, 167–178. [CrossRef]
17. Coxon, J.A.; Melville, T.C. Application of direct potential fitting to line position data for the $X^1\Sigma_g^+$ and $A^1\Sigma_u^+$ states of Li_2. *J. Mol. Spectrosc.* **2006**, *235*, 235–247. [CrossRef]
18. Kosman, W.M.; Hinze, J. Inverse perturbation analysis: Improving the accuracy of potential energy curves. *J. Mol. Spectrosc.* **1975**, *56*, 93–103. [CrossRef]
19. Geum, N.; Jeung, G.-H. Undulating potential curves of the Rydberg states of NaHe. *Chem. Phys. Lett.* **2001**, *333*, 314–318. [CrossRef]

3 Potential energy hyper-surfaces of the CO_3 complex

Contents

3.1 Introduction . . . 36
3.1.1 Background . . . 36
3.1.2 Objectives . . . 38
3.2 Computational methods . . . 38
3.2.1 Structure optimizations and energy refinement . . . 38
3.2.2 PES, Intersection points and seam curves . . . 39
3.2.3 Reference energies of reactants and products . . . 39
3.3 Results and discussion . . . 40
3.3.1 Formation of planar star-shape CO_3 and quenching reaction . . . 42
3.3.2 Formation of chain-shape CO_3 states and reaction pathways . . . 45
3.3.2.1 Trans and cis chain-shape CO_3 . . . 45
3.3.2.2 CO_3+O → CO_3 → CO+O_2 reaction pathways on the triplet PES's . . . 48
3.3.2.3 CO_3 + O → CO_3 → CO + O_2 reaction pathways on the singlet PES's . . . 48
3.3.3 Property changes along the reaction pathways . . . 49
3.3.4 Local shape of the PES's . . . 52
3.4 Conclusions . . . 55
Bibliography of Chapter 3 . . . 57

Abstract

The singlet and triplet electronic states of the CO_3 complex are studied with the best available quantum chemical methods, CASSCF and MRCI, using a flexible basis set without imposing any symmetry restriction. A large domain of the potential energy surfaces correlated with the lowest four reactant states of CO_2 + O is explored. Several pathways leading to two different types of isomers (star-shape and chain-shape) are found for both singlet and triplet spin states, and their spectroscopic properties are characterized. Among these pathways, three reaction pathways on high-lying singlet potential energy surfaces leading to the CO + O_2 dissociation channel are reported for the first time, as well as four intersystem crossing points between the triplet and singlet

surfaces. Change in electronic properties along different reaction paths is analyzed in detail.

3.1 Introduction

3.1.1 Background

The carbon trioxide, CO_3, was isolated and characterized experimentally for the first time by Moll et al. in 1966 [1]. They used three different techniques to produce CO_3 at very low temperatures and measured the infrared absorption. From the observed frequencies of the absorption lines, they deduced that its structure should be of C_{2v} symmetry. Weissberger's experiment and theoretical study in 1967 indicated that CO_3 was a possible intermediate of the CO_2 + $O(^1D)$ reaction.[2] In 1970, DeMore experimentally revealed that CO_3 has a very short lifetime and acts as an intermediate in the quenching reaction $O(^1D)$ + $CO_2 \rightarrow O(^3P)$ + CO_2.[3] The D_{3h} isomer of CO_3 was first identified by Jamieson et al. in 2006 using infrared spectroscopy.[4] They suggested that this structure in planetary atmospheres can be formed by isomerization of the C_{2v} isomer. Subsequent experiments using interstellar ice analogues and CO_2 ice have detected CO_3, confirming its importance in atmospheric chemistry.[5-9]

Various theoretical studies have reported that the C_{2v} symmetric CO_3 has closed-shell molecular orbitals and is more stable than its D_{3h} symmetric isomer.[10-14] CO_3 was confirmed as being an intermediate in the quenching and isotope exchange $O(^1D)$ + $CO_2 \rightarrow CO_3 \rightarrow O(^3P)/O(^1D)$ + CO_2 reaction (first type of reaction). [15, 16]

The second type of reaction, CO_2 + O $\rightleftharpoons$ CO + O_2, is also important in combustion chemistry.[17-20] The reaction rate coefficient of CO_2 + O $\rightarrow$ CO + O_2 varies a lot according to different experimental and theoretical studies[2, 18]. This variation is larger when the temperature is lower. A recent study by Vargas et al.[21] shows that this second type of reaction may occur as the second step reaction in the dissociation of CO_2. This reaction also has a significant influence on the thermochemistry in the Mars entry flight of spacecraft.[22] In high-temperature CO_2 flows, such as those around the Mars entry vehicle, Vargas et al. also showed that triplet CO_2, an excited state with a bent molecular shape, has a significant effect on the dissociation mechanism of CO_2. They predicted that triplet CO_2 promotes dissociation of CO_2 and leads to a variety of reaction pathways, including reactions via intersystem crossing.

To understand the role of CO_3 in the aforementioned reactions, several theoretical studies were done in the past by surveying the relevant potential energy surface (PES), by characterizing the spectroscopic properties of this intermediate, and by calculating the reaction coefficients. Froese and Goddard [23] have performed complete active space self-consistent field (CASSCF) and Møller-Plesset perturbation (MP2) calculations : they found two star-shape (carbon atom surrounded by three oxygen atoms) singlet CO_3 isomers (lowest one with C_{2v} symmetry and one with D_{3h} lying 4.0 kcal/mol above the former), one star-shape triplet CO_3 (C_{2v}) lying 7.0 kcal/mol over the singlet C_{2v} and two higher-lying (59.3 kcal/mol above the singlet C_{2v}) chain-shape

(OCOO) triplet planar (one cis-form and one trans-form) intermediate. As the chain-shape triplet states lie higher than the $O(^1D)$ + CO_2 reactant level, and supposing a transition state to form these complexes lying still higher, but without exploring possible chain-shape singlet states, they concluded that the second type of reaction cited above would not take place.

In order to find the $O(^3P)/O(^1D)$ branching ratio in the first type of reaction for the quenching and non-quenching isotope exchange reactions, $O(^1D) + CO_2 \rightarrow CO_3 \rightarrow O(^3P)/O(^1D) + CO_2$, Mebel et al. [13] have performed CASSCF calculations for the CO_3 system. They characterized the stationary points on the two lowest singlet and triplet PES's, as well as one intersection point, also called the intersystem crossing point. In addition to the star-shape equilibrium states found by Froese and Goddard (two singlets and one triplet), they also found a new star-shape state on the second singlet PES, as well as two van der Waals singlet states in the CO_2 + $O(^1D)$ entrance channel. They also found one high-lying chain-shape triplet equilibrium state without showing the full PES. The transition states connecting these structures were then searched along the minimum energy paths starting from the equilibrium structures. The energy barriers and the intersystem crossing points were manually searched and refined at the multi-reference configuration interaction (MRCI) level, and the branching ratio of $O(^3P)/O(^1D)$ were calculated by the non-adiabatic transition state theory or the radiationless theory incorporated with the RRKM theory. Their work showed a good agreement with the experimental data in the low collision energy regime, but a quantitative disagreement at higher collision energy. The $O(^1D)$ production was overestimated due to the underestimation of the barrier height, while the $O(^3P)$ production was underestimated due to the one-dimensional handling of the surface hopping probability.

Sharipov and Starik [24] have performed coupled-cluster singles-and-doubles with connected triple excitations (CCSD(T)) calculations using a cc-pVTZ basis set on the reaction paths for the second type of reaction cited above. They found two reaction pathways on the lowest triplet PES connecting the CO +O_2 ($X^3\Sigma_g^-$) channel to CO_2 + $O(^3P)$ via planar cis- and trans-type local minima. The cis isomer was found lower in energy than the trans isomer and connected to the CO_2 + $O(^3P)$ products via a lower transition state. By projecting the triplet minimum energy path on the singlet PES, they could estimate the location of the intersystem crossing point, lying nearby the triplet trans-type transition state. They pointed out the importance of this crossing for the production of excited $O(^1D)$ from the CO +O_2 ($X^3\Sigma_g^-$) reaction. The planar cis- and trans- local minima and transition states along the reaction pathway on the singlet PES were however not characterized.

In the experiments of Grigorenko et al. in 2020,[25], a T-shape van der Waals structure $CO_2 \cdots O(^3P)$ was produced by annealing a mixture of N_2/CO_2/Kr and decomposing N_2O into N_2 and O with a 193 nm light. With the second 193 nm photon, they observed the production of CO_3 and CO molecules. They also performed MP2 and CCSD calculations to understand the photochemical reactions, and postulated two scenarios of possible reaction pathways producing CO and O_2.

3.1.2 Objectives

The aim of the present work is to extend the previous quantum chemical calculations to survey larger area of the PES's and to include more singlet and triplet electronic states related to the four lowest asymptotic states, namely $CO_2(\tilde{X}^1\Sigma_g^+)$ + O(^3P) (ground state), $CO_2(\tilde{X}^1\Sigma_g^+)$ + O(^1D) (first excited state), $CO_2(\tilde{X}^1\Sigma_g^+)$ + O(^{1}S) (second excited state), and $CO_2(^3B_2)$ + O(^3P) (third excited state). It is necessary as different states interact with each other via non-adiabatic and spin-orbit couplings. To do that, we have used a better basis set and included more electron correlation effect via larger MRCI (see further in section 3.2.1) than in the works cited above. No geometrical restriction to planar structure was imposed in the begining, that is, we used C_1 point-group symmetry. For higher point-group symmetry cases (C_s or C_{2v}), we have done secondary calculations using the appropriate symmetry with the molecular plane for the reflection, to determine the irreps of the states. We also have used the intrinsic reaction coordinate (IRC) method to connect the equilibrium states via the transition states. As the result, we have found new equilibrium intermediate states and the transition states connecting between the formers, unknown in previous studies. We also have found several possible reaction paths for $CO_3 \rightarrow CO{+}O_2$. We present in this paper many aspects related to the PES, i.e., the intermediate states, transition states, their spectroscopic properties, and the electronic properties. Thus we show in this work a fairly complete picture on the title reactions for the first time. The reaction dynamic aspects will follow elsewhere.

3.2 Computational methods

3.2.1 Structure optimizations and energy refinement

Structure optimizations of CO_3 are performed by the CASSCF method using MOLPRO software.[26] We assume seven closed-shell orbitals and consider all possible configurations distributing 16 electrons over 13 active molecular orbitals (MO's), for the given symmetry. The employed basis set is the augmented correlation consistent polarized valence triple zeta (aug-cc-pVTZ) basis set consisting of 5s4p3d2f functions centered to each atom. Six geometry parameters in z-matrix coordinates are optimized without assigning any symmetry restrictions. For the optimized structures, the normal mode frequencies and IRC's are calculated at the CASSCF level in the same manner as for the optimization calculations. In order to refine the energy of the optimized structures, single-point calculations were performed at the MRCI level, assuming four cores, seven closed, and nine active orbitals. All IRC calculations were done using a single state, except for a few cases where state-averaged calculations were done, as will be specified later.

To evaluate the possible size-inconsistency, the Davidson correction [27] (+Q) adapted for the multi-reference cases was added and compared to the uncorrected energies. In this work, the energies including this correction are indicated by MRCIQ (+Q added to MRCI). As this correction is known to be too strong and as can be seen in the result

section, this correction significantly changes the energy of the CO_3 complex states by systematically lowering the complex energy in comparison with the reactant and product energies. The active space was chosen considering the accuracy *vs* computation time on the CASSCF level, and all possible single and double excitations were included for MRCI.

3.2.2 PES, Intersection points and seam curves

With six internal degrees of freedom, a PES is, in fact, a hypersurface in seven dimensions, so special care should be taken to explore even a single surface. Indeed, if a sufficiently large domain of geometry is not explored, it is difficult to know if two different partial sections belong to a single hypersurface or not.

When a singlet PES and a triplet PES cross each other, the intersecting points make a hypercurve, called a "seam line" or "seam curve", and there exists one point (i.e., a specific molecular geometry) having the lowest energy, often called the conical intersection point or the intersystem crossing point, that we shall rather call spin crossing point (SXP) hereafter. It is the molecular geometry whereabouts the spin state (singlet or triplet) may change via the spin-orbit coupling. The SXP was sought a specific optimization procedure implemented in MOLPRO [26].

3.2.3 Reference energies of reactants and products

In this study, we explore the singlet and triplet potential energy surfaces to find the possible reaction paths connecting the CO_2 + O and CO + O_2 channels. Because the chemical reaction involves a drastic change of the global geometry, from the reactant to the product via the intermediate, the computational methods need to have correct size-consistency. That is, the accuracy of the calculation should be consistent between the dissociated states (reactant and product) and the intermediate (compact geometries) states. The size-consistency in this aspect of the present computational methods is thus assessed. We considered here four reactant asymptotes, $CO_2(\tilde{X}^1\Sigma_g^+)$ + O(^3P), $CO_2(\tilde{X}^1\Sigma_g^+)$ + O(^1D), $CO_2(\tilde{X}^1\Sigma_g^+)$ + O(^1S), and $CO_2(^3B_2)$ + O(^3P), and three product asymptotes $CO(\tilde{X}^1\Sigma^+)$ + $O_2(\tilde{X}^3\Sigma_g^-)$, $CO(\tilde{X}^1\Sigma^+)$ + $O_2(a^1\Delta_g)$ and $CO(\tilde{X}^1\Sigma^+)$ + $O_2(b^1\Sigma_g^+)$. Then, the energies for the supermolecular system consisting of two fragment molecules at the reactant/product asymptotes are computed by placing the two fragments at the distance of 100 Å. The electronic energies are computed at CASSCF(16,13)/aug-cc-pVTZ, MRCI(8,9)/aug-cc-pVTZ on top of the CASSCF(16,13) calculation, and MRCIQ levels of calculation.

Since O(^1D) exhibits a five-fold degeneracy, the $CO_2(\tilde{X}^1\Sigma_g^+)$ + O(^1S) state can be calculated as the 6th singlet state when the C_1 point-group is considered. To maintain consistency with the reference energy state, $CO_2(\tilde{X}^1\Sigma_g^+)$ + O(^3P), state-averaged CASSCF calculations were performed for six singlet states and one triplet state for all the asymptotes. Note here that we have employed two types of CO_2 in the CO_2 + O supermolecules : one is a linear CO_2 with geometry optimized for the singlet $\tilde{X}^1\Sigma_g^+$

ground state, and the other is a bent CO_2 optimized for the triplet $^3B_2$ state. For the linear CO_2, the energies calculated for the first five singlet states are almost identical. In contrast, the sixth state exhibits a closed-shell highest occupied molecular orbital (HOMO) in both CO_2 and O fragments, justifying to assign this state as $CO_2(\tilde{X}^1\Sigma_g^+)$ + $O(^1S)$. In the case of bent CO_2, the first three singlet states exhibit very close energies, with two open shells in both the CO_2 and O fragments. These observations justify designating the lowest singlet state with the bent CO_2 as the $CO_2(^3B_2)$ + $O(^3P)$.

The relative energies measured from the $CO_2(\tilde{X}^1\Sigma_g^+)$ + $O(^3P)$ asymptote are compared with the sum of energies of two fragments in Table 3.1. The supermolecular system energies tend to become smaller with respect to that of $CO_2(\tilde{X}^1\Sigma_g^+)$ + $O(^3P)$, as the level of the computational method increases from CASSCF to MRCI, meaning larger correlation energy in the complex than in the reactant or product. The Davidson correction energy changes the supermolecular energy levels significantly and improves the energy level with respect to the NIST data. At the MRCIQ level, the maximum deviation from the sum of the computed fragment energies is 9.3 kcal/mol for $CO(\tilde{X}^1\Sigma^+)$ + $O_2(X^3\Sigma_g^-)$ asymptote. It can also be noted that adding energies from separate calculations of the fragments (smaller systems) gives better energy levels in comparison with the experimental data of NIST. This means, as could be inferred naturally, that the calculation on the smaller systems gives more accurate energies than the calculation on the larger systems.

TABLE 3.1 : Asymptotic energies (in kcal/mol) of ground and excited states of atomic and molecular fragments of the CO_3 system

System	NIST[a]	Sum of fragment energies[b]			Supermolecule energy		
		CASSCF	MRCI	MRCIQ	CASSCF	MRCI	MRCIQ (Err[c])
$CO_2(^3B_2)$ + $O(^3P)$	106.0	110.5	107.0	100.7	116.2	117.3	106.2 (0.2)
$CO_2(\tilde{X}^1\Sigma_g^+)$ + $O(^1S)$	96.6	123.9	98.3	93.1	125.0	107.2	98.6 (2.0)
$CO_2(\tilde{X}^1\Sigma_g^+)$ + $O(^1D)$	45.3	51.3	46.0	45.6	50.0	46.4	45.9 (0.6)
$CO_2(\tilde{X}^1\Sigma_g^+)$ + $O(^3P)$	0.0	0.0	0.0	0.0	0.0	0.0	0.0
$CO(\tilde{X}^1\Sigma^+)$ + $O_2(b^1\Sigma_g^+)$	45.8	52.2	56.0	46.5	70.0	66.0	52.8 (7.0)
$CO(\tilde{X}^1\Sigma^+)$ + $O_2(a^1\Delta_g)$	30.7	35.2	33.2	31.1	55.0	49.9	36.9 (6.1)
$CO(\tilde{X}^1\Sigma^+)$ + $O_2(X^3\Sigma_g^-)$	8.1	15.9	11.3	4.0	37.1	30.7	17.4 (9.3)

[a] Energies calculated from the formation enthalpies in NIST database[28]
[b] Electronic energies as a sum of energies of individual fragments
[c] Electronic energies calculated for a CO_3 supermolecule with an interfragment distance of 100 Å.

3.3 Results and discussion

Let us consider CO_2 + O as the reactant and count the possible number of the electronic states, not including the spin-orbit interaction, for the CO_3 complex. First, excluding the electron excitation from $2s^2$, four 2p electrons in the oxygen atom can be in three

different atomic orbital (AO) occupations, i.e. electron configurations, in $O(^3P)$: (i) $p_-^2 p_0^1 p_+^1$, (ii) $p_0^2 p_+^1 p_-^1$, and (iii) $p_+^2 p_-^1 p_0^1$, in complex AOs, with singly occupied AOs in parallel spins. They are equivalent to, in real AOs, $p_x^2 p_y^1 p_z^1$, $p_y^2 p_z^1 p_x^1$, and $p_z^2 p_x^1 p_y^1$. So, from the ground state $CO_2(\tilde{X}^1\Sigma_g^+) + O(^3P)$, three electronic states and corresponding three PESs would result. For the singlet electronic state, the previous three configurations should be in antiparallel spins. Furthermore, three more configurations are possible : (iv) $p_-^2 p_0^2 p_+^0$, (v) $p_0^2 p_+^2 p_-^0$, and (vi) $p_+^2 p_-^2 p_0^0$. The configuration (vi) makes the $O(^1S)$ state and the remaining five, (i)−(v), make the $O(^1D)$ state. So, from $CO_2(\tilde{X}^1\Sigma_g^+)$ + $O(^1D)$ five states would result, in all. Among those, only three configurations (i), (ii), and (iii) can make bonding with the carbon dioxide. The (iv) and (v) cannot make any bonding as they contain only closed sub-shells, so the corresponding two PES's would be only repulsive. For the same reason, the single PES originating from $CO_2(\tilde{X}^1\Sigma_g^+)$ + $O(^1S)$ should be repulsive and will not be considered in the present study. From $CO_2(^3B_2)$ + $O(^3P)$, three states can be made as in the ground state. The interaction between the repulsive PES's and the attractive PES's will be discussed in 3.3.2.

If we consider CO + O_2 as the product and count the number of the electronic states for the CO_3 complex, there would be one from $CO(\tilde{X}^1\Sigma^+) + O_2(\tilde{X}^3\Sigma_g^-)$ as the oxygen dimer in the ground state is nondegenerate. There should be two electronic states from $CO(\tilde{X}^1\Sigma^+) + O_2(a^1\Delta_g)$ as the doubly occupied highest-lying MO in $O_2(a^1\Delta_g)$ can be in two different occupations, $\pi_g(x)^2$ or $\pi_g(y)^2$. And from $CO(\tilde{X}^1\Sigma^+) + O_2(b^1\Sigma_g^+)$, two PES's would result as two unpaired electrons in antiparallel spins have two possibilities of occupying two π_g MOs, but the PES's we obtained remain below this asymptote.

In the present study, we have identified nine equilibrium states (referred hereafter as EQ's) for the CO_3 complex, five singlets and four triplets, and transition states (TS's hereafter) connecting between them on the potential energy hypersurfaces, which span from four CO_2 + O asymptote to two CO + O_2 asymptotes. These stationary structures form a CO_3 complex in either star-like (CO_3) or chain-like (OCOO) configurations, depending on which atom of the CO_2 fragment makes a bond with the free atomic oxygen. We also have found several equilibrium states of van der Waals type (VW's hereafter). Although we have found more than one VW from each asymptote having different geometrical characteristics, we are not going to discuss this variety as they all have very small bond energies. Grigorenko et al. [25] have reported an observation of one T-shape VW made from the triplet ground state asymptote, but did not give the intermolecular vibrational frequencies to compare with our calculated values, 27 and 36 cm^{-1}. We shall only show VW from $CO_2(\tilde{X}^1\Sigma_g^+) + O(^3P)$, VW1 from $CO_2(\tilde{X}^1\Sigma_g^+)$ + $O(^1D)$, and VW2 from $CO_2(^3B_2)$ + $O(^3P)$.

We have found five possible reaction pathways on the PES connecting the reactants CO_2 + O and the products CO + O_2. All of them involve chain-shape transition and intermediate states. The star-shape structures lie in a lower energy range, and no direct connection to the CO + O_2 asymptotes has been observed in the present study, as also reported in the literature. In the following subsections, we present the details of the obtained structures and their IRC connections. In 3.3.1, we describe the star-shape structures and their IRC connections from CO_2 + O, along with quantitative

comparisons of the electronic energy levels with available experimental data. In 3.3.2, we discuss the chain-shape structures and the $CO_2 + O \rightarrow CO + O_2$ pathways, which include a noteworthy reaction pathway involving an out-of-plane deformation of the CO_3 complex. This pathway is examined in detail in terms of property changes along the IRC, such as MOs, electron occupations, etc., in 3.3.3. This subsection also presents multi-state energy profiles along an IRC to explore the multi-reference character of the reaction pathway. Finally, subsection 3.3.4 presents three-dimensional slices of the potential energy hypersurface to provide insights into the shape of the global PES.

3.3.1 Formation of planar star-shape CO_3 and quenching reaction

In our present study, the lowest equilibrium states of CO_3 are all of star-shape, which consists of three C−O bonds on the same plane. We have found, in all, five stationary points with the star-shape structure; two singlet states (^{1}EQ0, ^{1}EQ1) on the lowest singlet PES and one triplet state (^{3}EQ1) on the lowest triplet PES, and one each (^{1}EQ2, ^{3}EQ2) on the second lowest singlet and triplet PES. The optimized geometric parameters, electronic energy, and vibrational frequencies for these five states are tabulated in Table 3.2 with the available experimental and computational values in past studies. The state ^{3}EQ2 is the new one we found and it has not been reported in the previous theoretical works. The connections between the EQ's and the TS's lying nearby are shown in the energy diagram in Figure 3.1, which has been found by IRC calculations at CASSCF level.

The ground state ^{1}EQ0 belongs to the C_{2v} point-group, and the additional calculations assuming C_{2v} symmetry have reveiled that this state is a $^1A_1$ state. This state lies much below the $CO_2(\tilde{X}^1\Sigma_g^+) + O(^1D)$ asymptote meaning a large bond energy, and at the MRCI level, even lower than the $CO_2(\tilde{X}^1\Sigma_g^+) + O(^3P)$ asymptote. ^{1}EQ0 is only the star-shape structure having a single bond linking one pair of oxygen atoms adding to the two single bonds between the carbon and the oxygen atoms, while the other four star-shape states have three single C-O bonds. The second-lowest equilibrium state ^{1}EQ1 has a slightly higher energy level than ^{1}EQ0, and belongs to $^1A_1$ symmetry the same as ^{1}EQ0. Among the star-shape complexes, ^{1}EQ1 is the only structure belonging to D_{3h} point-group. The upper states, ^{1}EQ2, ^{3}EQ1 and ^{3}EQ2 have C_{2v} molecular geometries, and respectively belong to $^1A_2$, $^3B_2$ and $^3B_1$ symmetry. As shown in Table 3.2, the optimized geometric parameters for the three lowest states agree well with those in Mebel's work despite the differences in the basis set used for the geometry optimizations. The energies are also consistent with Mebel's results with a maximum of 2 kcal/mol (5 kcal/mol) deviation at the CASSCF (MRCI) levels, respectively.

Although experimental values of the formation enthalpy of CO_3 itself are not available, we deduced it as the sum of the formation enthalpy of CO_3^- and the electron affinity of CO_3. The formation enthalpy of CO_3 is -490 ± 50 kJ/mol (-117 ± 12 kcal/mol), and the electron affinity of CO_3 is greater than 3.34 eV (77.0 kcal/mol) according to the NIST database. Hrovat et al. have determined that the adiabatic electron affinity of D_{3h}

TABLE 3.2 : Geometric parameters, relative electronic energies, and vibrational frequencies of the five lowest electronic states of the star-shape CO_3 system. Energies are with respect to $CO_2(\tilde{X}^1\Sigma_g^+) + O(^3P)$

Structure	^{1}**EQ0**	^{1}**EQ1**	^{1}**EQ2**	^{3}**EQ1**	^{3}**EQ2**
	C_{2v} 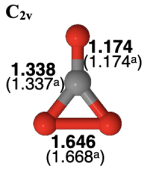	D_{3h} 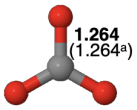	C_{2v} 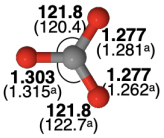	C_{2v} 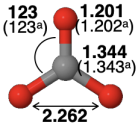	C_{2v} 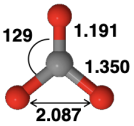
Energy kcal/mol					
CASSCF	18.82 (20.29[a])	25.22 (25.39[a])	46.0(44.28[a])	40.37(42.68[a])	41.28
MRCI	1.07 (2.85[a])	9.50 (4.77[a])	30.0(24.11[a])	24.92(25.93[a])	29.52
MRCI+Q	-5.23 (0.4[a])	-1.63 (1.46[a])	17.3(20.83[a])	21.28(23.26[a])	26.32
ZPE(CASSCF)	8.55 (8.54[a])	7.24 (7.37[a])	6.00(6.07[a])	7.74(7.79[a])	7.47
Frequency cm^{-1}					
ν_1	2061 (2045[b])	1176	1050	1701	1822
ν_2	1073 (1073[b])	1176	821	1238	969
ν_3	1013 (972[b])	1082	742	916	853
ν_4	680	759	694	687	689
ν_5	579 (593[b])	437	506	445	560
ν_6	575 (568[b])	437	385	429	333

[a] Computation, Mebel et. al.[13] [b] Experiments, Moll et. al. [1] for $^{12}C^{16}O_3$

singlet CO_3 is 4.06 ± 0.03 eV (93.5 ± 0.7 kcal/mol) from the negative ion photoelectron spectrum of the CO_3 radical anion. They also determined that the lowest triplet state is 17.8 ± 0.9 kcal/mol above the D_{3h} singlet state, and the energy difference between the lowest and the second triplet states is 4.6 kcal/mol. Using these data, we determined the relative energy of the lowest four CO_3 states and compared them with our computational results in Table 3.3. At the MRCIQ level, our computed relative energies fall within the error bounds of reference values for all four states. The calculated adiabatic electron affinities for ^{1}EQ0 agreed well with the NIST value, and that for ^{1}EQ1 is closer to the NIST value than to Hrovat's. The experimental values of energy gaps between the states are well reproduced across all levels of calculation. The vibrational frequencies calculated at the CASSCF agree well with the spectroscopic measurements by Moll et al.[1]. These results indicate that including the electronic correlation at least at the MRCI level is necessary for a quantitatively accurate estimation of the activation energy for the $CO_2 + O_3 \rightleftharpoons CO + O_2$ reaction. However, the CASSCF level still provides an acceptable qualitative analysis for the CO_3 system.

As shown in Figure 3.1, ^{1}EQ0 and ^{1}EQ1 are separated by a relatively low transition state, $^1TS_{0-1}$. The relatively short bond distance between a pair of oxygen atoms (165 pm) in the latter in comparison with the former and the high vibrational frequency (2061 cm^{-1}) support this supplementary bond. ^{1}EQ2 lies on the second lowest singlet

TABLE 3.3 : Relative energies (kcal/mol) and electron affinities (eV) of singlet and triplet states of CO_3

System	Relative energies [kcal/mol]				Electron affinity, EA [eV] Energy gap, ΔE [kcal/mol]			
	NIST/Exp.	CASSCF	MRCI	MRCIQ	NIST/Exp.	CASSCF	MRCI	MRCIQ
$CO_3(^3EQ2)$	33.4±14.5	46.8	29.5	26.3	ΔE_{TT} = 4.6[a]	4.7	4.6	5.1
CO_3 ($^3EQ1$)	28.8±14.5	42.1	24.9	21.2	ΔE_{ST} = 17.8±0.9[a]	16.9	15.4	22.8
CO_3 ($^1EQ1$)	11.0±13.6	25.2	9.5	-1.6	EA = 4.06±0.03[a]	2.18	3.00	3.36
					2.04	2.81	3.53	
$CO_3(^1EQ0)$	-5.6±11.9	18.8	1.1	-5.2	EA > 3.40[b]	1.90	2.63	3.20
					3.399?	-0.49	0.40	1.08
$CO_3^{\cdot-}$	-82.6±11.9	-25.05	-59.58	-79.1				
$CO_2(\tilde{X}^1\Sigma_g^+) + O(^3P)$	0.0	0.0	0.0	0.0				

[a] Hrovat et al.[29] : ΔE_{ST} is the energy gap between the singlet state with D_{3h} structure ($^1EQ1$) and the lowest triplet state($^3EQ1$);
ΔE_{TT} is energy gap between the lowest ($^3EQ1$) and the second lowest ($^3EQ2$) triplet state; [b] NIST[30]

PES, and $^1TS_{VW-2}$ to access $^1EQ2$ is very high. The energy barrier from $CO_2(\tilde{X}^1\Sigma_g^+)$ + $O(^1D)$ is as high as 29 kcal/mol at CASSCF level. At MRCIQ level, however, this barrier corresponding to $^1TS_{VW-2}$ is very much lowered to 7.8 kcal/mol, that can be compared with the barrier of 4.5 kcal corresponding to TS_{VW-0}. So one should keep in mind that Fig. 1 and Fig. 2 used CASSCF and the inclusion of the electron correlation effect (so-called dynamic) adjusts different levels quantitatively. The first lowest triplet state $^3EQ1$ is separated from the van der Waals complex ^3VW by the transition state $^3TS_{VW-1}$ at an energy level of 47.2 kcal/mol with respect to $CO_2(\tilde{X}^1\Sigma_g^+)$ + $O(^3P)$ asymptote. The second lowest triplet state $^3EQ2$ can be accessed from ^3VW via $^3TS_{VW-2}$ at an energy level of 55.2 kcal/mol, which was obtained by a three-state calculation.

Three star-shape SXP's between the singlet PES and the triplet PES were identified. The lowest one, SXP1, corresponds to the crossing point between the $1^1A''$ PES and the $1^3A''$ PES. SXP1 lies energetically and geometrically very close to both $^1EQ2$ on $^11A''$ and $^3TS_{2-2}$ on $^3A''$ PES. As SXP1 lies to the right of $^1TS_{VW-2}$, the quenching reaction converting $O(^1D)$ to $O(^3P)$, or vice versa, can only occur with a large activation energy (equivalent to 24,670 K) to overcome $^1TS_{VW-2}$. For the crossing between the $1^1A'$ PES and the $1^3A'$ PES's, we have found SXP2 lying close to $^1TS_{VW-0}$ and $^3TS_{VW-1}$. The quenching reaction $O(^1D) \rightarrow O(^3P)$ around SXP2 can occur without any supplementary kinetic energy. Thus SXP2 would be involved in the experimentally observed quenching reaction. The SXP3 between the $1^1A'$ PES and the $1^3A''$ PES is energetically and geometrically very close to those of $^3TS_{VW-1}$. A change of PES around SXP3 may occur with the spin-orbit interaction, but it should also accompany the emission or absorption of a photon because of the different parity of $1^1A'$ from $1^3A''$.

3.3.2 Formation of chain-shape CO_3 states and reaction pathways

3.3.2.1 Trans and cis chain-shape CO_3

We have found four chain-shape structures (OCOO), ^{1}EQ3, ^{1}EQ4, ^{3}EQ3 and ^{3}EQ4 as stationary points on the lowest singlet and triplet PES's. The energy levels of these structures, the geometric parameters, and the zero-point vibrational energies are shown in Figure 3.2, as well as the connections between the EQ's and TS's.

The four chain-shape states have cis- or trans- configuration as a combination of a bent CO_2 with an additional O−O bond, and their energy levels are clustered around 82 kcal/mol (60 kcal/mol) above the $CO_2(\tilde{X}^1\Sigma_g^+)$ + O(^3P) asymptote at CASSCF (MRCIQ) level regardless of its total spin quantum number. The second and third lowest chain-shape states are ^{3}EQ3 and ^{3}EQ4 on the lowest triplet PES, and they respectively have a planar trans- and cis-type geometry. On the singlet PES, we have found a noteworthy non-planar equilibrium ^{1}EQ3. ^{1}EQ3 has a dihedral angle of 83°, and forms a cis-type structure (Here, the dihedral angle is measured as an angle between the plane defined by CO_2 and the plane defined by the C−O−O segment. The dihedral angle 180 corresponds to the planar trans-type, ^{3}EQ3 and ^{1}EQ4, and the angle 0 corresponds to the planar cis-type, ^{3}EQ4. We have not found any planar cis-type chain structure in the present study. ^{1}EQ4 is a planar trans-type chain-shape state on the singlet PES, and has the highest energy among the obtained five chain-shape structures. MRCIQ gives that ^{1}EQ4 lies 3.48 kcal/mol higher than the ^{1}EQ3 and they are separated by ^{1}TS$_{4-3}$ lying 3.96 kcal/mol above ^{1}EQ3. The rotational barrier between the two non-superposable stereo isomers, i.e. the energy difference between ^{1}TS$_{3-3}$ and ^{1}EQ3, is 6.45 kcal/mol at MRCIQ level.

Two non-planar chain-shape SXP's connecting the singlet PES and the triplet PES were found. The trans SXP4 lies in the vicinity of ^{1}TS$_{4-3}$ on the potential energy hypersurface, and the cis SXP5 lies nearby ^{1}TS$_{3-3}$. The spin change via the spin-orbit interaction would occur around theses SXP's.

We have found five possible reaction pathways, two on the triplet and three on the singlet PES's, connecting the CO_2 + O and CO + O_2 channels via transition and intermediate states with chain-like (OCOO) geometry, as shown in the Figure 3.2. We present them and discuss their characteristics in the following subsections.

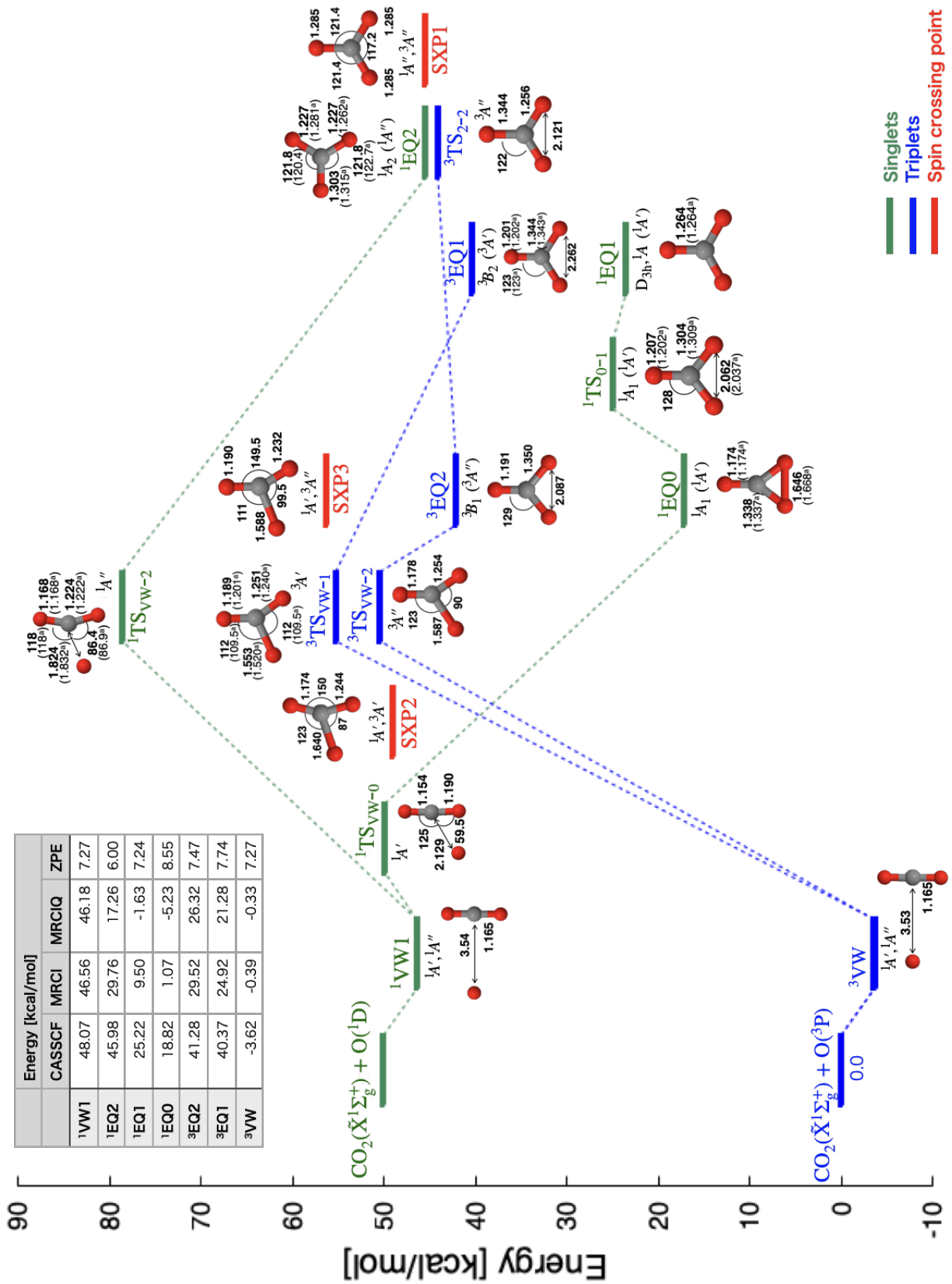

FIGURE 3.1 : Energy Diagram of the star-shape CO_3 (Energy levels are with respect to $CO_2(\tilde{X}^1\Sigma_g^+) + O(^3P)$)

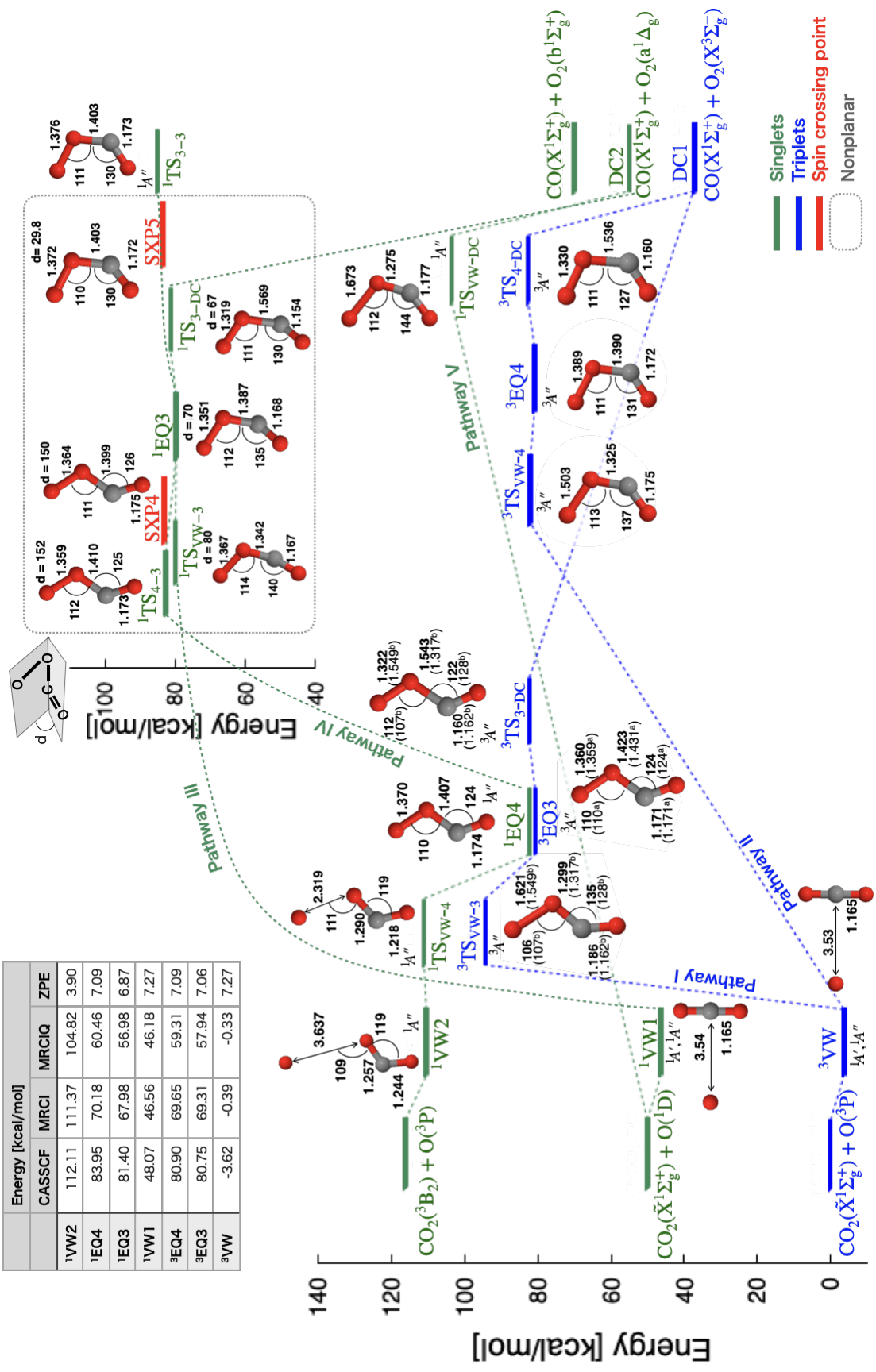

Energy [kcal/mol]	CASSCF	MRCI	MRCIQ	ZPE
^{1}VW2	112.11	111.37	104.82	3.90
^{1}EQ4	83.95	70.18	60.46	7.09
^{1}EQ3	81.40	67.98	56.98	6.87
^{1}VW1	48.07	46.56	46.18	7.27
^{3}EQ4	80.90	69.65	59.31	7.09
^{3}EQ3	80.75	69.31	57.94	7.06
^{3}VW	-3.62	-0.39	-0.33	7.27

FIGURE 3.2 : Energy Diagram of the chain-shape CO_3

3.3.2.2 CO_3+O → CO_3 → CO+O_2 reaction pathways on the triplet PES's

Starting from the reactant $CO_2(\tilde{X}^1\Sigma_g^+)$ + O(^3P), when the unbound oxygen atom approaches to one of the two oxygen atoms attached to the carbon atom, it falls in a van der Waals structure ^{3}VW. From ^{3}VW, we could identify two IRC pathways on the triplet potential energy surface going to the product $CO(X^1\Sigma_g^+)$ + $O_2(X^3\Sigma_g^-)$. In these reaction paths, the transition and the intermediate states keep planar molecular geometries, but one pathway makes a trans-type chain-shape intermediate (hereafter called Pathway I), while the other makes a cis-type chain-shape intermediate (Pathway II).

On Pathway I, the van der Waals structure ^{3}VW connects to the transition state $^3TS_{VW-3}$ at a very high energy of 94 kcal/mol (74 kcal/mol) at CASSCF (MRCIQ) level. In this TS, the imaginary frequency corresponds to the antisymmetric stretching mode of O−O−CO with larger amplitude in O−O stretching than in O−C stretching. $^3TS_{VW-3}$ then connects to ^{3}EQ3 located at 81 kcal/mol (59 kcal/mol) , which consequently connects to the transition state $^3TS_{3-DC}$ at 82 kcal/mol (55 kcal/mol) at CASSCF (MRCIQ) level with a small energy barrier. The latter TS also has an imaginary frequency in the antisymmetric stretching mode of O−O−C with larger amplitude in OO−CO stretching, and connects to the $CO(X^1\Sigma_g^+)$ + O_2 dissociation channel (DC).

On Pathway II, the van der Waals structure ^{3}VW connects to the transition state $^3TS_{VW-4}$ at the energy of 82.1 kcal/mol. The energy gap between the ^{3}EQ4 and $^3TS_{VW-4}$ in Pathway II is very small and is much smaller than that in Pathway I. $^3TS_{VW-4}$ has an imaginary frequency in the O−OCO bond stretching mode, showing a bond formation between the two oxygen atoms towards the CO_3 complex. This TS then connects to ^{3}EQ4 at 81 kcal/mol (58 kcal/mol), which consequently connects to $^3TS_{4-DC}$ at 83 kcal/mol (56 kcal/mol) at CASSCF (MRCIQ) level. The $^3TS_{4-DC}$ has an imaginary frequency in the OO−CO stretching, showing the O_2−CO bond breaking, and connects to the dissociation channel, $CO(X^1\Sigma_g^+)$ + O_2.

On both pathways, the potential energy wells confining the chain-shape intermediates are very shallow. Thus, the complex in chain-shape would be unstable, and its lifetime should be short.

3.3.2.3 CO_3 + O → CO_3 → CO + O_2 reaction pathways on the singlet PES's

One of the three reaction pathways on the singlet PES's (hereafter called Pathway III) starts from ^{1}VW1, a van der Waals structure resulting from the interaction of of $CO_2(\tilde{X}^1\Sigma_g^+)$ with O(^1D), and ends at the $CO(X^1\Sigma_g^+)$ + $O_2(a^1\Delta_g)$ dissociation channel (DC2). This pathway connects to $^1TS_{VW-3}$ at the energy of 31.1 kcal/mol from the $CO_2(\tilde{X}^1\Sigma_g^+)$ + O(^1D) asymptote. $^1TS_{VW-3}$ has a cis-type non-planar geometry with a dihedral angle of 83°, where the dihedral angle is measured between the plane defined by CO_2 and the plane defined by the C−O−O segment. $^1TS_{VW-3}$ connects to ^{1}EQ3 at the energy 2.9 kcal/mol (3.0 kcal/mol) below $^1TS_{VW-3}$ at CASSCF (MRCIQ) level, then to $^1TS_{3-DC2}$ at the energy 1.6 kcal/mol (4.0 kcal/mol) above ^{1}EQ3, and finally to DC2.

Another reaction pathway (hereafter called Pathway IV) lying on the lowest singlet

PES begins from ^{1}VW2, a van der Waals structure resulting from the interaction of $CO_2(^3B_2)$ with $O(^3P)$, and ends at DC2. The PES connected to the $CO_2(^3B_2)$ + $O(^3P)$ asymptote was never explored before. It connects ^{1} VW2 and DC2 via three TS's and two EQ's, which involves the out-of-plane deformation from trans-type geometries to cis-type ones. The relative energy of ^{1}VW2 measured from $CO_2(\tilde{X}^1\Sigma_g^+)$ + $O(^3P)$ asymptote is 112 kcal/mol (115 kcal/mol) at CASSCF (MRCIQ) level. The first intermediate state connecting from ^{1}VW2 is ^{1}EQ4 having a planar trans-chain structure, and separated from ^{1}VW2 by the transition state $^1TS_{VW-4}$. $^1TS_{VW-4}$ is located at the energy level slightly (0.6 kcal/mol at CASSCF and 6.6 kcal/mol at MRCIQ level) higher than ^{1}VW2, and 28 kcal/mol (54 kcal/mol) higher than ^{1}EQ4 at CASSCF (MRCIQ) level . The second intermediate state ^{1}EQ3 is connected ^{1}EQ4 via a non-planar transition state $^1TS_{4-3}$, which is energetically close to ^{1}EQ3. From ^{1}EQ3 the passage to $^1TS_{3-DC2}$ leads to the DC2. This pathway would lead to a practically barrierless direct reaction, i.e., the reactant made from the triplet carbon dioxide and the ground state triplet oxygen atom will directly lead to the oxygen dimer and carbon monoxide. Alternatively, ^{1}EQ3 connects to its non-superposable stereoisomer twin (mirror image, not shown in Figure 3.2) via $^1TS_{3-3}$.

The third reaction pathway we found (hereafter called Pathway V) lies on the second lowest singlet PES, starting from ^{1}VW1 and ending at the $CO(X^1\Sigma_g^+)$ + $O_2(a^1\Delta_g)$ dissociation channel. Unlike the pathways III and IV, the CO_3 molecular structure keeps a planar shape all along Pathway V, and has only one transition state, $^1TS_{VW-DC}$, located at a very high level above the $CO_2(\tilde{X}^1\Sigma_g^+)$ + $O(^1D)$ asymptote, so this pathway requires a large activation energy.

3.3.3 Property changes along the reaction pathways

As shown in the previous subsection, there are three possible reaction pathways on the singlet PES connecting the reactants CO_2 + O and the product CO + O_2. In this subsection, we shall focus on Pathway IV and Pathway V to analyze the property changes along their IRC coordinates. Firstly, we examine Pathway IV, a noteworthy pathway in which two triplet state reactants $CO_2(^3B_2)$ + $O(^3P)$ yield two singlet state products $CO(X^1\Sigma_g^+)$ + $O_2(a^1\Delta_g)$ while maintaining on a singlet PES. Our primary interest lies in how the MOs change along this pathway with the out-plane deformation of the molecular structure. Then, we present the energy profiles of the ground and the excited states along Pathway V, which is the only possible reaction pathway keeping a planar molecular structure and connecting to the $CO(X^1\Sigma_g^+)$ + $O_2(a^1\Delta_g)$ asymptote. This will help us understand how the states originating from the five-folded $O(^1D)$ interact with the higher state.

The variation of the lowest potential energy of the CO_3 system along Pathway IV, i.e., involving the most spontaneous reaction, is shown in Figure 3.3, with the variations of geometric parameters, electron occupancies of the four highest MO's, and the norm of dipole moment along the IRC. The potential energy curve has three plateaus : two of them are asymptotes corresponding to the energy of $CO_2(^3B_2)$ + $O(^3P)$ and to $CO(X^1\Sigma_g^+)$ + $O_2(a^1\Delta_g)$, and the middle one corresponds to compact trans-chain

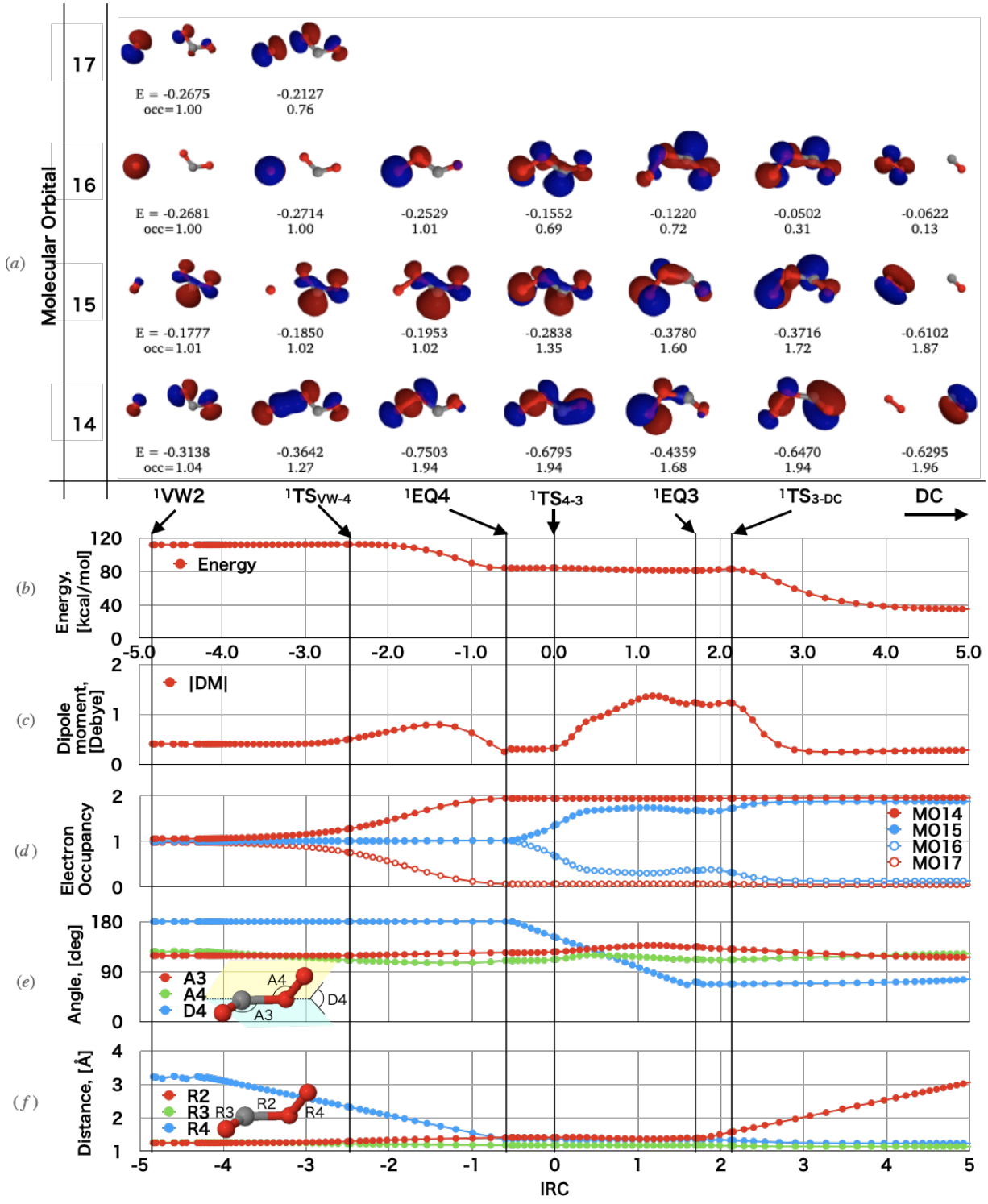

FIGURE 3.3 : Properties along pathway IV : (a) Molecular orbitals at stationary points, (b) Potential energy, (c) Norm of dipole moment, (d) Electron occupancies, (e) Bond angles, (f) Bond lengths

(^{1}EQ4) and cis-chain (^{1}EQ3) CO_3 geometries. These equilibrium structures are almost isoenergetic. ^{1}EQ4 is connected to ^{1}VW2 via $^1TS_{VW-4}$ and is 28 kcal/mol lower than that of $^1TS_{VW-4}$. . Even though there are three EQ's and three TS's, since the energy barriers to overcome TS's in the forward direction are very small, we can see here that $CO_2(^3B_2) + O(^3P) \rightarrow CO(X^1\Sigma_g^+) + O_2$ is practically a barrierless reaction.

The variation of electron occupancies in Figure 3.3d clearly shows that MO14 and MO17 are strongly correlated, as well as MO15 and MO16. At ^{1}VW2, MO14 − MO17 are essentially singly occupied MOs. Along the IRC from ^{1}VW2 to ^{1}EQ4, where the terminal atomic oxygen $O(^3P)$ approaches to $CO_2(^3B_2)$, the electron occupancy steadily increases to two while that of MO17 decreases to zero at ^{1}EQ4, so two open shells are converted to one closed shell making a bond. Along Pathway IV, the sum of MO14 and MO17 occupancies is almost constant at the value of 2. We see a similar change for the pair of MO15 and MO16, whose occupancies vary along the transition from ^{1}EQ3, where the variation of dihedral angle is involved. The MO15–MO16 change is accompanied by the increase of dipole moment, suggesting a charge transfer as can be seen in Figure 3.3c.

For the IRC linking ^{1}VW2, $^1TS_{VW-4}$ and ^{1}EQ4, the terminal atomic oxygen $O(^3P)$ approaches to $CO_2(^3B_2)$, the OCO angle (A3, see Figure 3.3 for definition) slightly opens, and the OO−CO distance (R2) slightly increases. As indicated by the constant dihedral angle (D4) at 180 degrees, the four atoms in the super system consisting of $O(^3P)$ and $CO_2(^3B_2)$ remain in the same plane. The dihedral angle decreases linearly when going from ^{1}EQ4 to $^1TS_{4-3}$ then to ^{1}EQ3. This is consistent with the observation that $^1TS_{4-3}$ has an imaginary frequency in the out-of-plane vibration mode. The transition from ^{1}EQ3 to $^1TS_{3-DC}$ and the dissociated state $CO(X^1\Sigma_g^+) + O_2(a^1\Delta_g)$ takes place along an almost constant dihedral angle, while the molecular structure still keeps non-planar form. $^1TS_{3-DC}$ is characterized by an imaginary vibrational frequency in the OO−CO stretching mode, and the dissociation occurs due to the OO−CO bond breaking.

Figure 3.4 shows the electronic energy profiles of the ground and vertically excited states along Pathway V. This figure shows complex adiabatic interactions between the nine electronic states originating from three asymptotes, so resulting into a cascade of avoided crossings. The energies are calculated by a series of multi-state single-point calculations under the C_s symmetry restriction for each IRC point. We considered nine electronic states to resolve the states from the five-fold degenerate $CO_2(\tilde{X}^1\Sigma_g^+)$ + $O(^1D)$, the non-degenerate $CO_2(\tilde{X}^1\Sigma_g^+)$ + $O(^1S)$, and the triply degenerate CO_2 (linear : $^3B_2$ deformed to $^3\Sigma_u^+$ in this section of PES) + $O(^3P)$ asymptotes, which are five A' and four A'' states in C_s symmetry. Pathway V, obtained on the second lowest PES in the C_1 point-group, follows the PES of the $1A''$ state in the C_s symmetry. As seen in the red lines, when $O(^1D)$ approaches linear CO_2, the degeneracy of the $O(^1D)$ state is resolved into three groups, each with different slopes of energy increase. All the states exhibit a repulsive nature until the formation of the transition state. The $1A''$ state has about the same energy with that of the $2A'$ state and their energies increase together in the reactant phase, maintaining higher values than the $1A'$ state. Once the

CO_3 complex is formed, the $1A''$ state forms a plateau of energy and keeps about the same energy with the $1A'$ state, leading to the $CO(X^1\Sigma_g^+) + O_2(a^1\Delta_g)$ products. After separating from the $1A''$ state, the $2A'$ state undergoes avoided crossings with the $1A'$ state, further increases in energy, undergoes another avoided crossing with the $3A'$ state, then decreases in energy, and finally leads to the $CO(X^1\Sigma_g^+) + O_2(b^1\Sigma_g^+)$ products. The blue line representing the $4A'$ state from the $CO_2(\tilde{X}^1\Sigma_g^+)$+$O(^1S)$ asymptote also shows a repulsive behavior, while the green lines of the $3A''$, $4A''$, and $5A'$ states from the CO_2 (linear : $^3B_2$ deformed to $^3\Sigma_u^+$ in this section of PES) + $O(^3P)$ asymptote exhibit attractive character, due to a charge transfer from the $O(^3P)$ atom to the CO_2 moiety. The $3A'$, $4A'$ and the $5A'$ states show several avoided crossings due to the adiabaticity. Similarly, the $2A''$, $3A''$, and $4A''$ states also exhibit several avoided crossings.

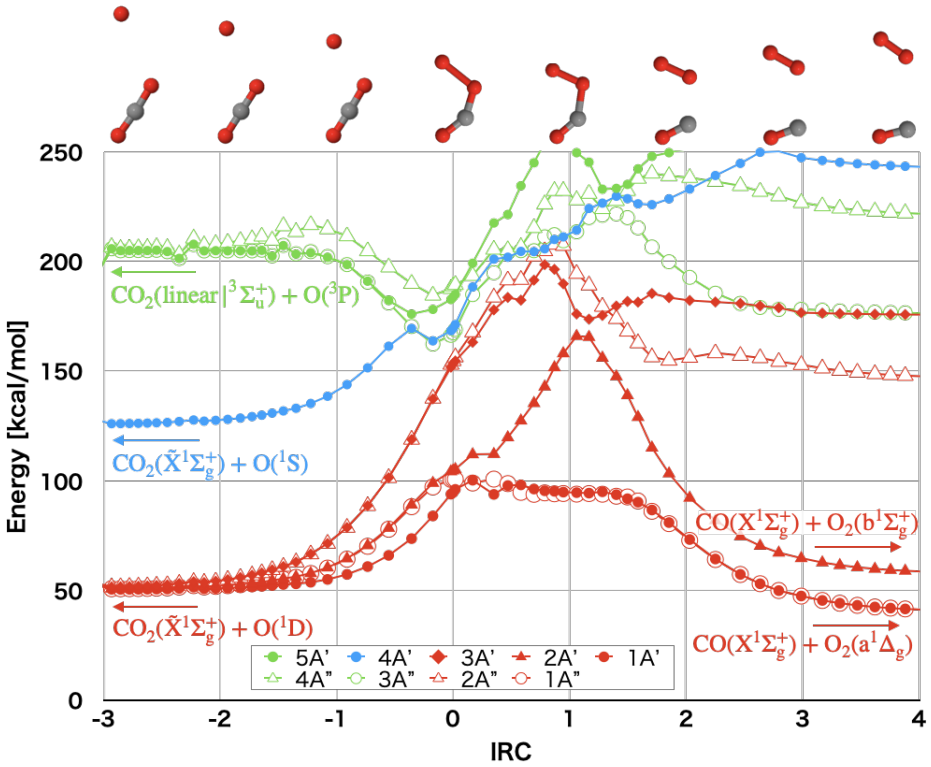

FIGURE 3.4 : Electronic energies of the lowest singlet states along the Pathway V

3.3.4 Local shape of the PES's

Figure 3.5 illustrates the singlet potential energy contours calculated at the CASSCF level, where the third atomic oxygen is placed around a bent CO_2 with optimized geometry of the $^3B_2$ state. The CO_2 lies in the xy plane. The figure on the left show the PES of the first lowest state (1^1A), and the figure on the right show the PES of the second lowest state (2^1A). Figures 3.5c-1 and c-2 are xy slices of the PES where the CO_3 system forms a planar structure. The solid black line indicates the van der Waals radius

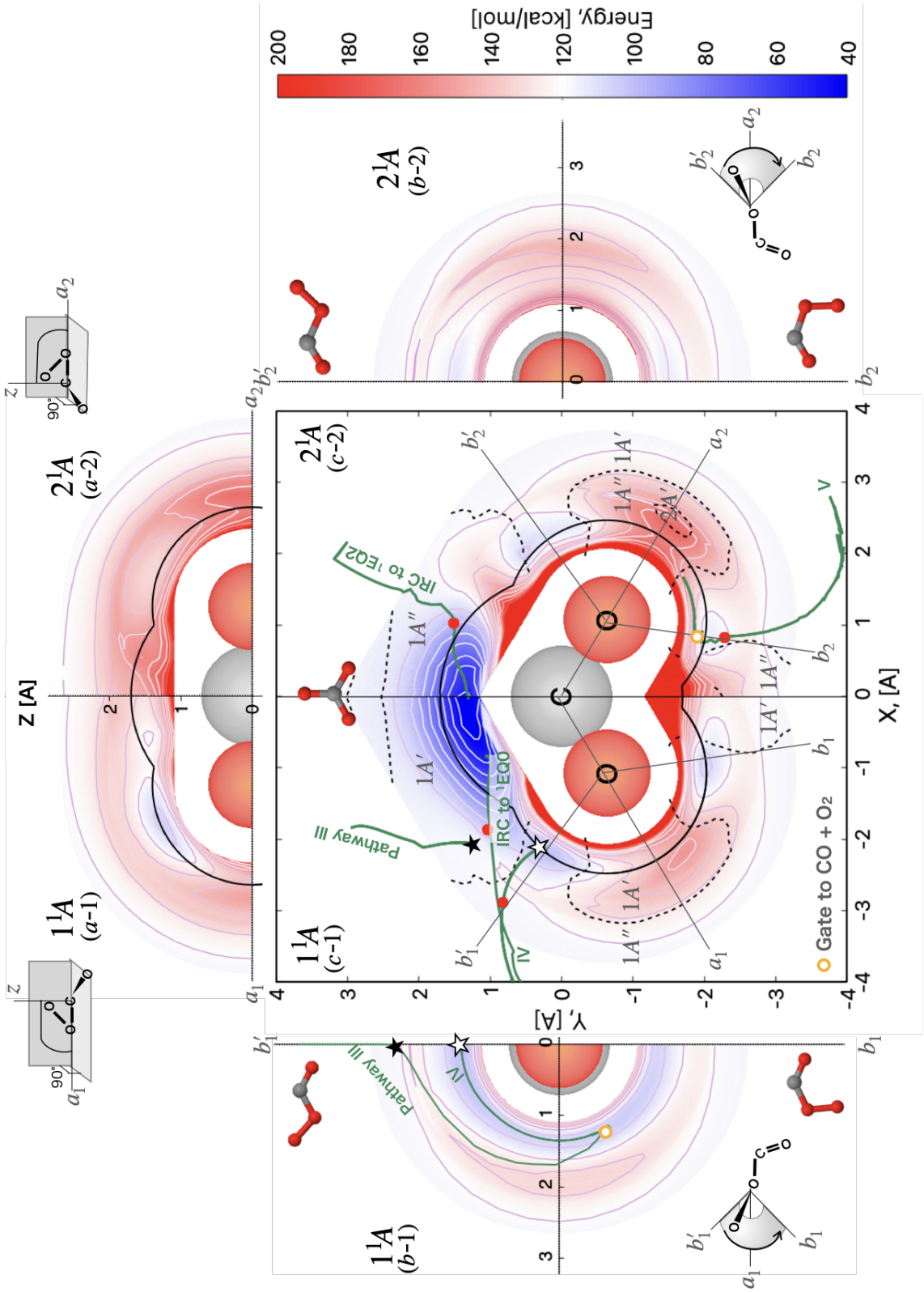

FIGURE 3.5 : PES's when placing an atomic oxygen around a bent CO_2

of atoms. The dashed lines show the crossing seams between the $1^1A'$ and $1^1A''$ states, which were identified from the $1^1A'$ and $1^1A''$ PES's obtained by additional calculations assuming C_{2v} symmetry. Both 1^1A and 2^1A exhibit deep wells near the carbon atom at the vertex of the bent CO_2. The region including the well in the 1^1A state corresponds to the $1^1A'$ state in C_{2v} symmetry, and the region in the 2^1A state corresponds to the $1^1A''$ state. The well in 1^1A ($1^1A'$) is deeper than that of 2^1A ($1^1A''$). We can see peaks of the PES near the cross points of the van der Waals radius line and the CO bond axis, and a pair of valleys around each oxygen atom of CO_2 almost following the van der Waals radius line. They correspond to the entrance to make either cis or trans type chaine-shape complex. In the case of $1^1A''$ also, there are two shallow wells corresponding to one cis and one trans type chain-shape complex. When plotting the IRCs of reaction pathways on these two PES's, they generally follow the valleys between the crests, although the molecular geometries on the IRCs are not exactly the same as those on these contour maps, because the geometry of CO_2 was fixed in these figures. We also have discovered an out-of-plane reaction pathway leading to a reaction on the singlet PES. Figures 3.5a-1 and a-2 present the PES contours when the third O atom is placed on a plane perpendicular to the plane formed by the bent CO_2, passing through the CO axis. A low-energy spot is located in the region where the COO angle is approximately 113 degrees. Figures 3.5b-1 and b-2 show the PES contours when the dihedral angle between the third O atom and the CO_2 plane changes while the C−O−O angle is kept at 113 degrees. The actual computational domain resembles the surface of a cone with the terminal oxygen atom of CO_2 as the apex. This surface is then projected onto a plane with the CO axis as the normal vector to create the diagram. Figure 3.5b-1 reveals a path passing through a tunnel that can connect the trans and the cis types of chain-shape structure. This tunnel is slightly uphill from a trans structure towards an energy barrier connecting to a cis structure, and there is a hole halfway down that leads to DC. In Pathway IV, starting from VW2 with a bent CO_2 fragment, the CO_3 reaches the tunnel while keeping a planar structure. Conversely, Pathway III, starting from VW1 with a linear CO_2 fragment, joins the tunnel at a specific dihedral angle since this pathway involves simultaneous changes in the bond angle of CO_2 and the dihedral angle. The 2^1A PES also has a route connecting trans and cis structures; however, the energy barrier to make a trans-cis transformation is relatively high. Thus, Pathway V on the 2^1A PES prefers to take the route to DC rather than a route to cis-trans transformation.

Figure 3.6 illustrates the IRC's involving non-planar states on the calculated singlet PES as a function of the CO_2 bond angle and the CO_2−O dihedral angle. This figure includes Pathway III and Pathway IV. The two paraboloid-like cones located at the edges of the PES show over-lying PES of the excited state making the avoided crossing with the lowest PES. The edges (0° for cis-type and 180° for trans-type) of the PES correspond to planar molecular geometries. The additional calculations assuming C_s symmetry identify the point-groups of the states on the edges to be either $1^1A'$ or $1^1A''$ states. The crossing PES's for the planar cases shows the conical intersections made from two different point-group symmetries. We can see two streams of IRCs (Pathway III and IV) crossing at ^{1}EQ3. One is the IRC (Pathway III) varying in the CO_2 angle

with no significant variation in the dihedral angle, and the other (Pathway IV) has variation in the dihedral angle with no significant variation in the CO_2 angle. The latter non-planar IRC connects, at one end, to the planar equilibrium state ^{1}EQ4 on the $^1A''$ surface, which originates from $CO_2(^3B_2)$ + O(^3P). At the other end, it leads to the transition state $^1TS_{3-3}$ which connects ^{1}EQ3 and its non-superposable stereoisomer. Along this IRC, there are two intersection points with the $1^1A/1^3A$ seam, where CO_3 system possibly undergoes spin transition.

From Figure 3.2 and Figure 3.6, we can see the possibility of a new collisional excitation/de-excitation reaction $CO_2(^3B_2)$ + O(^3P) $\rightleftharpoons$ $CO_2(\tilde{X}^1\Sigma_g^+)$ + O(^1D), that is entirely different from $CO_2(\tilde{X}^1\Sigma_g^+)$ + O(^1D) $\rightarrow$ $CO_2(\tilde{X}^1\Sigma_g^+)$ + O(^3P) .

3.4 Conclusions

In exploring a large area of the possible internal geometrical parameters, we could find a general view on the seven-dimensional PES about the CO_3 complex and the reaction paths for two possible decompositions, CO_2 + O and CO + O_2. This work resulted in finding three intermediate states not reported so far in the literature : one star-shape triplet state (^{3}EQ2) and two chain-shape singlet states (^{1}EQ3 and ^{1}EQ4) of CO_3. We have used larger basis set and introduced more electron correlation effect than used in previous theoretical studies and found a better agreement with the available experimental data.

In addition to the two triplet reaction pathways reported in the literature, we also found three new connections between the intermediate states on the singlet PESs at high energies ($\simeq$ 80 kcal/mol) above the $CO_2(\tilde{X}^1\Sigma_g^+)$+O(^{3}P) ground state asymptote, but energetically accessible from the $CO_2(^3B_2)$ + O(^{3}P) asymptote. In particular, we have found two possible CO_2 + O $\rightarrow$ CO + O_2 reaction pathways (III and IV) on the singlet PES involving the out-of-plane deformation of the chain-shape CO_3 complex. Pathway IV, originates from the fourth lowest electronic asymptote, $CO_2(^3B_2)$ + O(^3P). Moreover, a direct pathway (Pathway V) connecting the $CO_2(\tilde{X}^1\Sigma_g^+)$ + O(^{1}D) channel to the $CO(X^1\Sigma_g^+)$ + $O_2(a^1\Delta_g)$ channel is reported for the first time. Furthermore, we characterized five intersystem crossing points and found in particular a new spin-change (quenching) reaction involving two different asymptotes, $CO_2(^3B_2)$ + O(^{3}P) and $CO_2(\tilde{X}^1\Sigma_g^+)$ + O(^{1}D).

The evolution of the electronic properties along various reaction pathways was analyzed in detail, showing how the bond is made and broken. In particular, the electron transfer (donation) from the oxygen atom to the carbon dioxide initiates the bonding in CO_3.

The visualization of the PES's involved in various reactions presented in this work should help the kinetic and dynamic analyses in the future. The energy range of the new pathways is compatible with the energy regime found in shock-wave layers. We believe our results could be of interest for kinetic studies of hypersonic CO_2 flows.

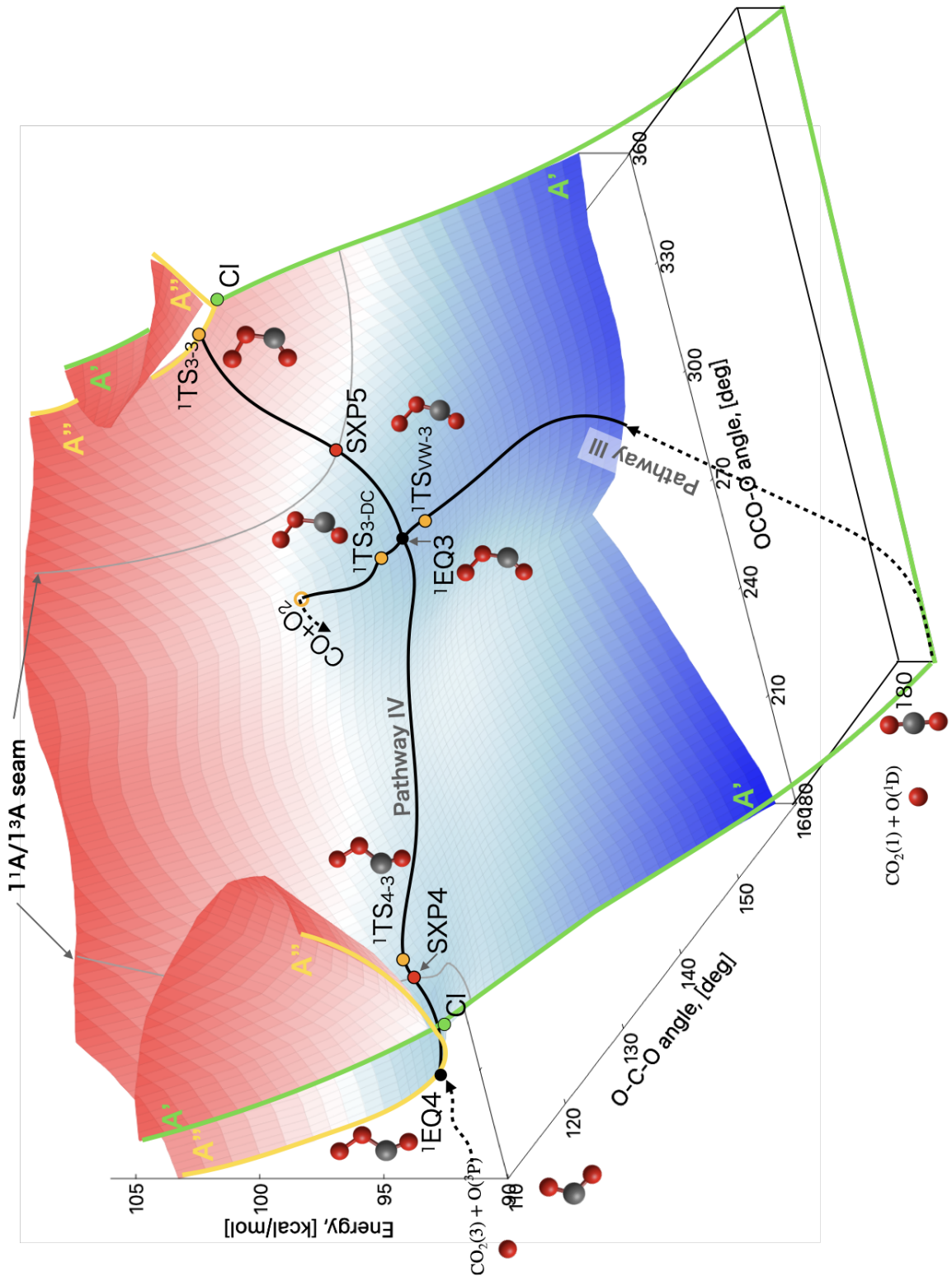

FIGURE 3.6 : Schematic 3D representation of the lowest singlet PES's along the OCO bending and OCOO torsion coordinates

Bibliography of Chapter 3

(1) MOLL, N. G.; CLUTTER, D. R.; THOMPSON, W. E. Carbon Trioxide : Its Production, Infrared Spectrum, and Structure Studied in a Matrix of Solid CO_2. *The Journal of Chemical Physics* **1966**, *45*, 4469-4481.

(2) WEISSBERGER, E.; BRECKENRIDGE, W. H.; TAUBE, H. Reaction of O(^{1}D) with CO_2 at Low Temperatures. *The Journal of Chemical Physics* **1967**, *47*, 1764-1769.

(3) DEMORE, W. B.; DEDE, C. Pressure Dependence of Carbon Trioxide Formation in the Gas-Phase Reaction of O(^{1}D) with Carbon Dioxide. *The Journal of Physical Chemistry* **1970**, *74*, 2621-2625.

(4) JAMIESON, C. S.; MEBEL, A. M.; KAISER, R. I. Identification of the D_{3h} Isomer of Carbon Trioxide (CO_3) and Its Implications for Atmospheric Chemistry. *ChemPhysChem* **2006**, *7*, 2508-2513.

(5) BENNETT, C. J.; JAMIESON, C.; MEBEL, A. M. et al. Untangling the Formation of the Cyclic Carbon Trioxide Isomer in Low Temperature Carbon Dioxide Ices. *Physical Chemistry Chemical Physics* **2004**, *6*, 735-746.

(6) BENNETT, C. J.; JAMIESON, C. S.; KAISER, R. I. An experimental investigation of the decomposition of carbon monoxide and formation routes to carbon dioxide in interstellar ices. *The Astrophysical Journal Supplement Series* **2009**, *182*, 1-11.

(7) MARTÍN-DOMÉNECH, R.; MANZANO-SANTAMARÍA, J.; MUÑOZ CARO, G. M. et al. UV Photoprocessing of CO_2 Ice : A Complete Quantification of Photochemistry and Photon-Induced Desorption Processes. *Astronomy & Astrophysics* **2015**, *584*, A14.

(8) FERRARI, B. C.; SLAVICINSKA, K.; BENNETT, C. J. Role of Suprathermal Chemistry on the Evolution of Carbon Oxides and Organics within Interstellar and Cometary Ices. *Accounts of Chemical Research* **2021**, *54*, 1067-1079.

(9) FORTENBERRY, R. C.; PETERS, D.; FERRARI, B. C. et al. Rovibrational Spectral Analysis of CO_3 and C_2O_3 : Potential Sources for O_2 Observed in Comet 67P/Churyumov-Gerasimenko. *The Astrophysical Journal* **2019**, *886*, L10.

(10) GIMARC, B. M.; CHOU, T. S. Geometry and Electronic Structure of Carbon Trioxide. *The Journal of Chemical Physics* **1968**, *49*, 4043-4047.

(11) OLSEN, J. F.; BURNELLE, L. Molecular Geometry and Electronic Structure of Carbon Trioxide. *Journal of the American Chemical Society* **1969**, *91*, 7286-7290.

(12) CASTRO, M. A.; CANUTO, S.; SIMAS, A. M. Many-Body Perturbation Theory and Coupled-Cluster Calculations of the Ground-State Structure of CO_3. *Chemical Physics Letters* **1991**, *177*, 98-102.

(13) MEBEL, A. M.; HAYASHI, M.; KISLOV, V. V. et al. Theoretical Study of Oxygen Isotope Exchange and Quenching in the O(1D) + CO_2 Reaction. *The Journal of Physical Chemistry A* **2004**, *108*, 7983-7994.

(14) KAISER, R. I.; MEBEL, A. M. On the Formation of Higher Carbon Oxides in Extreme Environments. *Chemical Physics Letters* **2008**, *465*, 1-9.

(15) PERRI, M. J.; VAN WYNGARDEN, A. L.; BOERING, K. A. et al. Dynamics of the O(1D)+CO_2 Oxygen Isotope Exchange Reaction. *The Journal of Chemical Physics* **2003**, *119*, 8213-8216.

(16) PERRI, M. J.; VAN WYNGARDEN, A. L.; LIN, J. J. et al. Energy Dependence of Oxygen Isotope Exchange and Quenching in the O(^{1}D) + CO_2 Reaction : A Crossed Molecular Beam Study. *The Journal of Physical Chemistry A* **2004**, *108*, 7995-8001.

(17) BRABBS, T.; BELLES, F.; BROKAW, R. Shock-Tube Measurements of Specific Reaction Rates in the Branched-Chain H_2-CO-O_2 System. *Symposium (International) on Combustion* **1971**, *13*, 129-136.

(18) RAWLINS, W. T.; GARDINER, W. C. Rate Constant for CO + O_2 = CO_2 + O from 1500 to 2500 K. A Reevaluation of Induction Times in the Shock-Initiated Combustion of Hydrogen-Oxygen-Carbon Monoxide-Argon Mixtures. *The Journal of Physical Chemistry* **1974**, *78*, 497-500.

(19) SULZMANN, K. G. P.; MYERS, B. F.; BARTLE, E. R. CO Oxidation. I. Induction Period Preceding CO_2 Formation in Shock-Heated CO–O_2–Ar Mixtures. *The Journal of Chemical Physics* **1965**, *42*, 3969-3979.

(20) CHAOS, M.; DRYER, F. L. Syngas Combustion Kinetics and Applications. *Combustion Science and Technology* **2008**, *180*, 1053-1096.

(21) VARGAS, J.; LOPEZ, B.; LINO DA SILVA, M. Heavy Particle Impact Vibrational Excitation and Dissociation Processes in CO_2. *The Journal of Physical Chemistry A* **2021**, *125*, 493-512.

(22) TAKAYANAGI, H.; LEMAL, A.; NOMURA, S. et al. Measurements of Carbon Dioxide Nonequilibrium Infrared Radiation in Shocked and Expanded Flows. *Journal of Thermophysics and Heat Transfer* **2018**, *32*, 483-494.

(23) FROESE, R. D. J.; GODDARD, J. D. Features of the Lowest Singlet and Triplet Potential Energy Surfaces of Carbonate Radical. *The Journal of Physical Chemistry* **1993**, *97*, 7484-7490.

(24) SHARIPOV, A.; STARIK, A. Theoretical Study of the Reaction of Carbon Monoxide with Oxygen Molecules in the Ground Triplet and Singlet Delta States. *The Journal of Physical Chemistry A* **2011**, *115*, 1795-1803.

(25) GRIGORENKO, B. L.; DUARTE, L.; POLYAKOV, I. V. et al. Theoretical Characterization of the Photochemical Reaction CO_2 + O(^{3}P) $\rightarrow$ CO + O_2 Related to Experiments in Solid Krypton. *Chemical Physics Letters* **2020**, *746*, 137303.

(26) WERNER, H.-J.; KNOWLES, P. J.; MANBY, F. R. et al. The Molpro Quantum Chemistry Package. *The Journal of Chemical Physics* **2020**, *152*, 144107.

(27) LANGHOFF, S. R.; DAVIDSON, E. R. Configuration Interaction Calculations on the Nitrogen Molecule. *International Journal of Quantum Chemistry* **1974**, *8*, 61-72.

(28) LINSTROM, P.; W.G. MALLARD, E., *NIST Chemistry WebBook, NIST Standard Reference Database Number 69*; National Institute of Standards et Technology, Gaithersburg MD, 20899, https ://doi.org/10.18434/T4D303 : (retrieved June 21, 2024).

(29) HROVAT, D. A.; HOU, G.-L.; CHEN, B. et al. Negative Ion Photoelectron Spectroscopy Confirms the Prediction That D_{3h} Carbon Trioxide (CO_3) Has a Singlet Ground State. *Chemical Science* **2016**, *7*, 1142-1150.

(30) HUNTON, D. E.; HOFMANN, M.; LINDEMAN, T. G. et al. Photodissociation dynamics of CO_3^-. *The Journal of Chemical Physics* **1985**, *82*, 134-150.

4 Kinetics of the reactions CO_2 + O → CO_3 → CO + O_2

Contents

4.1 Introduction . . . 60
4.2 Method of Calculations . . . 61
4.2.1 Stationary Points on PES of CO_3 system . . . 61
4.2.2 Reaction rate constants . . . 62
4.2.2.1 Transitional State Theory . . . 62
4.2.3 Energy grained master equation . . . 62
4.3 Results . . . 63
4.3.1 IRC calculations and TST rate constants . . . 63
4.3.2 RRKM and BM rate constants . . . 64
4.4 Summary . . . 70
Bibliography of Chapter 4 . . . 71

4.1 Introduction

Mars and Venus, the planets closest and geologically similar to Earth, are believed to hold key insights into the origin of humankind and the evolution of the solar system. Mars, in particular, is of great interest due to its potential for water, life, and mineral resources, making it a primary target for space missions planned by the USA, EU, and Asian nations.

In Mars exploration missions, equipment such as rovers is stored in a capsule and sent to the Martian surface, passing through the atmosphere at high velocities of 5 to 10 km/s, corresponding to Mach numbers between 20 and 40, which fall within the hypersonic speed range. During the entry flight, the atmosphere around the entry capsule is strongly compressed, causing temperatures to rise to several tens of thousands of Kelvins. This intense heating excites the internal energy modes of gas molecules and triggers various chemical reactions in the atmospheric gases, known as high-temperature real-gas phenomena.

The Martian atmosphere consists of approximately 95% CO_2, 2.8% N_2, and 2% Ar. These high-temperature real-gas phenomena will produce species such as C, CO, C_2, and CN around the entry capsule, which have strong radiation mechanisms.[1] It is known that strong radiation is emitted from the nonequilibrium region behind

the shock wave[2], where the energy redistribution over energy levels and ongoing chemical reactions take place. The dissociation reactions of CO_2 and CO

$$CO_2 + M \leftrightarrows CO + O + M \tag{4.1}$$
$$CO + M \leftrightarrows C + O + M \tag{4.2}$$

is the most significant endothermic reaction among the reactions in the Mars entry flow, whose heat of reaction is about 126 kcal/mol and 256 kcal/mol, respectively. Once the atomic oxygen is generated by the R1 and R2, the exchange reactions

$$CO_2 + O \leftrightarrows CO + O_2 \tag{4.3}$$
$$CO + O \leftrightarrows C + O_2 \tag{4.4}$$

are initiated and promote R1 by consuming CO and O. Therefore, these exchange reactions are considered to be important reactions in analyzing the Mars entry flow.

There are many studies on the reaction rate constants for the reversed reaction, CO_2+O ← CO+O_2. Most of the experimental reaction rate constants were deduced from infrared emission spectroscopy in shock tubes in the 1960s and 1970s.[3-7]. The experimental reaction rate constants for the direct reaction CO_2+O → CO+O_2 are relatively rare. [8-10]. The computational rate constants from coupled cluster methods are given in [11]. These rate constants are reviewed, and the recommended values are given in some literature. [12, 13]

The present study studies the chemical kinetics of CO_2+O ⇆ CO+O_2 reactions based on the chemical reaction pathways obtained in the previous sections using ab initio electronic calculations. Firstly, the chemical reaction rate was derived from the transition-state theory and compared with the existing chemical reaction rate models. Then, the canonical reaction rate coefficients are calculated from microcanonical rates based on the RRKM theory. The one-dimensional energy-grained master equations are then solved at different temperature conditions to obtain phenomenological reaction rate coefficients. The obtained rate coefficients are compared with the experimental data and past theoretical studies.

4.2 Method of Calculations

4.2.1 Stationary Points on PES of CO_3 system

Potential energy calculations and structure optimization were performed at CASSCF level (Complete Active Space Self Consistent Field), using the aug-cc-pVTZ basis set (with 5s4p3d2f gaussian basis functions). The active space consists of 16 electrons distributed over 13 molecular orbitals (MOs), the first seven MOs being closed-shell orbitals. All calculations, including the IRC calculations, were performed using the MOLPRO [[14]] program.

4.2.2 Reaction rate constants

4.2.2.1 Transitional State Theory

The transition state theory (TST) reaction rate constants for $CO_2 + O \leftrightarrows CO + O_2$ are deduced by using the KiSThelP[7] package. The conventional expression of the TST reaction constant in the unit of cm^3/molecule-s is given by

$$k^{TST} = \sigma \frac{k_B T}{h} \frac{Q^{TS}}{N_A Q^R} \exp\left(-\frac{V^{\ddagger}}{k_B T}\right)$$

where σ is the reaction path degeneracy, k_b the Boltzmann constant, temperature, h the Planck constant, N_A the Avogadro's number, Q^{TS} is the partition function of the transition state, and Q^R is the products of the partition function of the products, and $V^{\ddagger}$ the activation energy. The KiSThelP package uses the equivalent expression for bimolecular reaction in terms of thermodynamics properties;

$$k^{TST} = \sigma \frac{k_B T}{h} \frac{k_B T}{p^0} \exp\left(-\frac{\Delta G^{\ddagger,0}}{RT}\right)$$

where $\Delta G^{\ddagger,0}$ is the standard Gibbs free energy difference between the reactants and the transitions state in the unit of J/mol.

4.2.3 Energy grained master equation

The energy-grained master equations (EGME) are written as follows.

$$\begin{aligned}\frac{dp_m(E)}{dt} = \omega \int_{E_{0m}}^{\infty} P(E|E')\,p_m(E')\,dE' - \omega\, p_m(E) \\ + \sum_{n\neq m} k_{nm}(E)\,p_n(E) - \sum_{n\neq m} k_{mn}(E)\,p_m(E) \\ - k_{Sm}(E)\,p_m(E) \\ + K_{Rm}^{eq} k_{Rm}(E) \frac{\rho_m(E)\,e^{-\beta E}}{Q_m(\beta)} n_A p_B - k_{Rm}(E)\,p_m(E)\end{aligned}$$

where the first and the second terms of the left-hand-side are the population gain/loss of an energy grain at E from/to the other energy grains at E' due to the collisional with the bath gas, the third and fourth are reversible gain/ loss by the reactions from/to other isomers, the fifth is the irreversible loss due to the reactions to products sink, and the sixth and the seventh are gain/loss by the reactions connecting from/to reactants. In the present study, the EGME is solved using MESMER software.

The probabilities appear in the first and the second term of Eq. (X) are calculated by an exponential down model,

$$P(E|E') = A(E') \exp\left(-(E'-E)/ < \Delta E >_d\right)$$

TABLE 4.1 : Energy of stationary points on the IRC paths at CASSCF and MRCIQ

States	Energy [kcal/mol]			
	Pathway I (trans)		Pathway II (cis)	
	CASSCF	MRCIQ	CASSCF	MRCIQ
$CO_2 + O$	0.0	0.0	0.0	0.0
TS1	94.6	74.4	82.7	61.0
INT	82.2	57.7	82.4	59.1
TS2	82.4	55.6	83.1	56.7
$CO + O_2$	36.9	12.9	36.9	12.9

where A is the normalization factor and the $< \Delta E >_d$ the average energy transferred in a deactivating collision. In the present study, $< \Delta E >_d = 500$ cm^{-1} was taken for N_2 as the heat bath gas.

The microcanonical rate constants, k_{nm}, are calculated by the RRKM methods.

4.3 Results

4.3.1 IRC calculations and TST rate constants

Two chemical reaction paths of the exchange reaction $CO_2(\tilde{X}^1\Sigma_g^+) + O(^3P) \leftrightarrows CO(X^1\Sigma_g^+) + O_2(X^3\Sigma_g^-)$ found by IRC calculations on the potential energy surface of the triplet CO_3 ground states are shown in Fig. 4.1. The reaction paths in Fig. 1a and 1b are the path with transition states of trans-OCOO ($^3TS_{vw-3}$ and $^3TS_{3-DC}$ on Pathway I) and with cis-OCOO ($^3TS_{vw-4}$ and $^3TS_{4-DC}$ on Pathway II), respectively. Both paths display two transition states and one intermediate state. For these stationary points with cis- and trans-structures, the potential energies defined with respect to the energy of $O_2(\tilde{X}^1\Sigma_g^+) + O(^3P)$ are summarized in Table 4.1. The intermediates on these two reaction paths are located in the very shallow well and are expected to have short lifetimes. If we take the activation energy as the energy difference between the highest transitions state and the $O_2(\tilde{X}^1\Sigma_g^+) + O(^3P)$ asymptote, the activation energies of Pathway I is 96.1 kcal/mol (46,112 K) at CASSCF level and 75.9 kcal/mol (38,213 K) at MRCIQ level, and 84.4 kcal/mol (42,492 K) at CASSCF and 61.0 kcal/mol (30,711 K) at MRCIQ for Pathway II. The values from MRCRQ calculations are comparable to the values of 37280 K for trans-TS and 30410 K for cis-TS from CCSD/cc-pVDZ calculations in Ref. [11].

Using the obtained activation energies, the reaction rate constants for the $CO_2(\tilde{X}^1\Sigma_g^+) + O(^3P) \rightarrow CO(X^1\Sigma_g^+) + O_2(X^3\Sigma_g^-)$ are derived based on the TST theory using the Kis-Thelp software[16]. The obtained three-parameter Arrhenius expression of the rate constants for each pathway are as follows :

$CO_2(\tilde{X}^1\Sigma_g^+) + O(^3P) \rightarrow CO(X^1\Sigma_g^+) + O_2(X^3\Sigma_g^-)$:

$$k_I = 1.9733 \times 10^4 T^{1.065} \exp(-315,960/RT) \text{ [m}^3\text{/mol} - \text{s]}$$

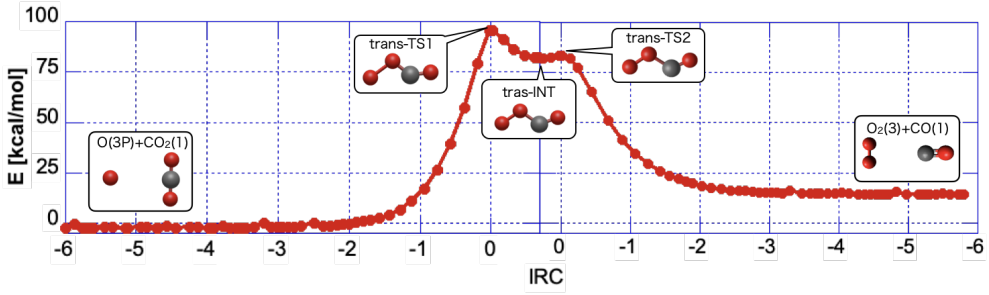

a. Pathway I : IRC path for cis-OCOO transition state at CASSCF level

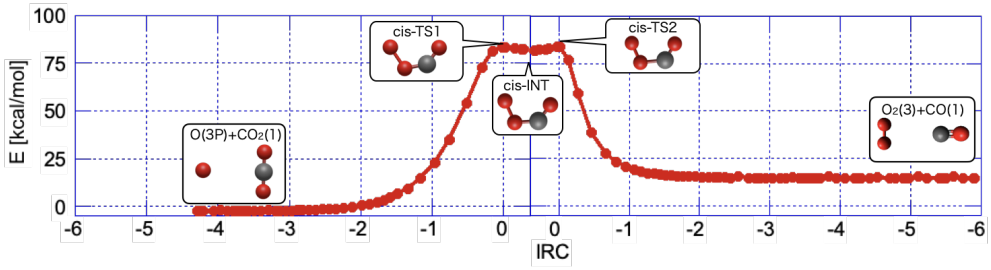

b. Pathway II : IRC path for trans-OCOO transition state at CASSCF level

FIGURE 4.1 : Chemical reaction paths of $CO_2(\tilde{X}^1\Sigma_g^+) + O(^3P) \leftarrow CO(X^1\Sigma_g^+) + O_2(X^3\Sigma_g^-)$

$$k_{II} = 3.0969 \times 10^4 T^{1.058} \exp(-241,610/RT) \text{ [m}^3\text{/mol} - \text{s]}$$
$$k_V = 1.0691 \times 10^4 T^{1.055} \exp(-225,820/RT) \text{ [m}^3\text{/mol} - \text{s]}$$

$CO_2(\tilde{X}^1\Sigma_g^+) + O(^3P) \leftarrow CO(X^1\Sigma_g^+) + O_2(X^3\Sigma_g^-)$:

$$k_{-I} = 0.19753 \times 10^4 T^{2.038} \exp(-309,550/RT) \text{ [m}^3\text{/mol} - \text{s]}$$
$$k_{-II} = 0.31040 T^{2.030} \exp(-285,200/RT) \text{ [m}^3\text{/mol} - \text{s]}$$
$$k_{-V} = 0.19144 T^{2.022} \exp(-282,690/RT) \text{ [m}^3\text{/mol} - \text{s]}$$

These rate coefficients are compared with the existing experimental and theoretical values in Fig. 4.2

4.3.2 RRKM and BM rate constants

The reaction rate constants are then calculated using MESMER software[17] based on the RRKM microcanonical rate constants, as well as the phenomenological rate constants by Bartis-Wisdom method (BM). The considered reaction model is given in the energy diagram in Fig. 4.3, and the obtained rate coefficients are compared with the existing experimental and theoretical values in Fig. 4.4 and Fig. 4.5. Figure 4.6 is the obtained time evolution of the fraction of reactants and products from the integration of EGME at various temperatures.

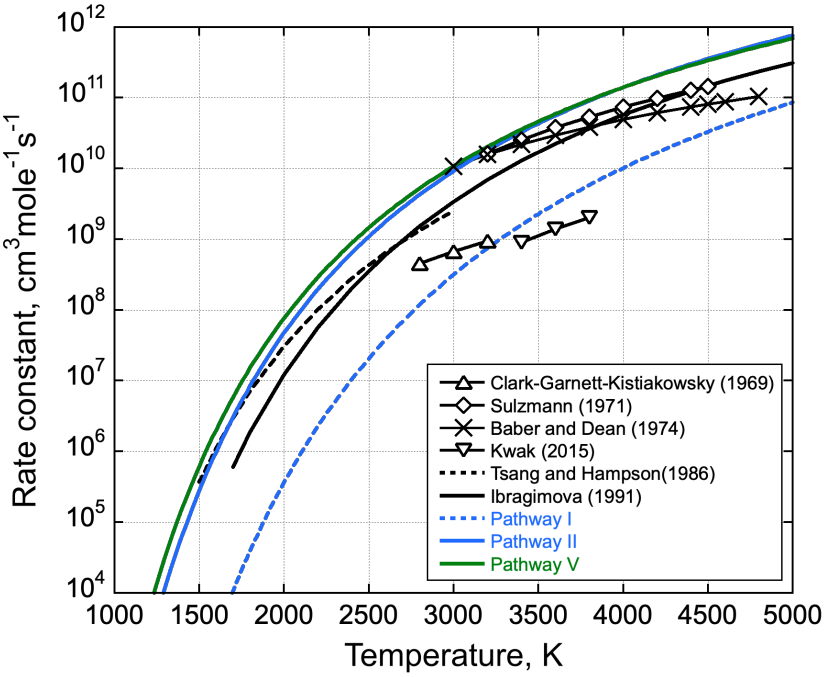

a. Forward reaction rate

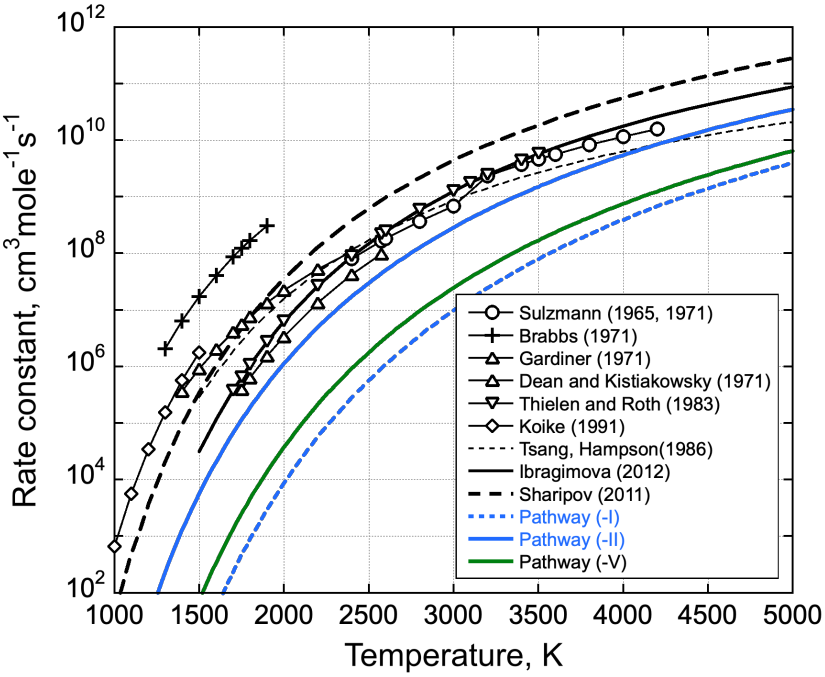

b. Backward reaction rate

FIGURE 4.2 : TST rate constants of $CO_2(\tilde{X}^1\Sigma_g^+)$+O(^{3}P) $\leftrightarrow$ CO($X^1\Sigma_g^+$) + $O_2(X^3\Sigma_g^-)$: Present calculations and the existing values in Ref.[15])

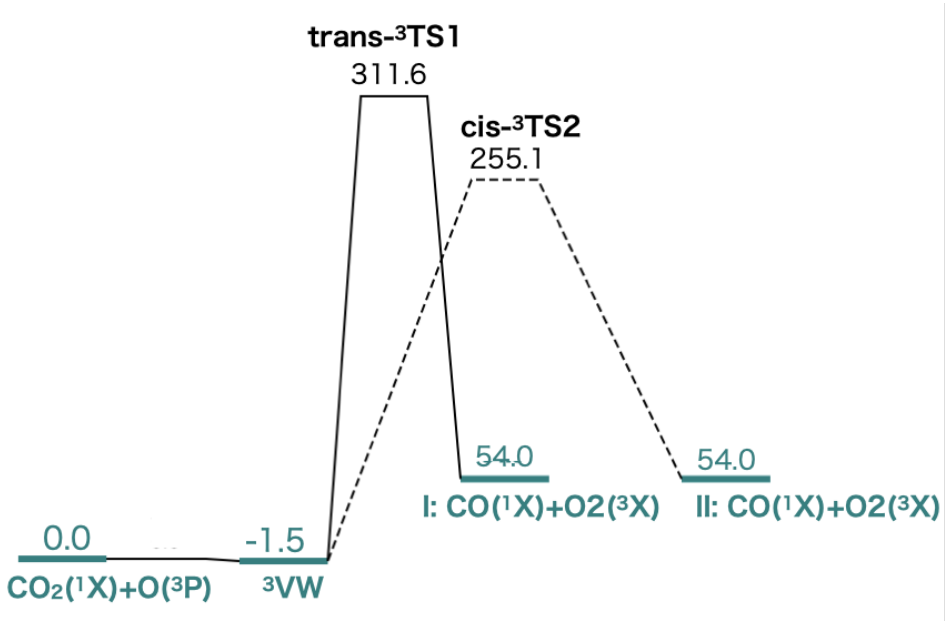

FIGURE 4.3 : Simplified reaction models of Pathways I and II for MESMER

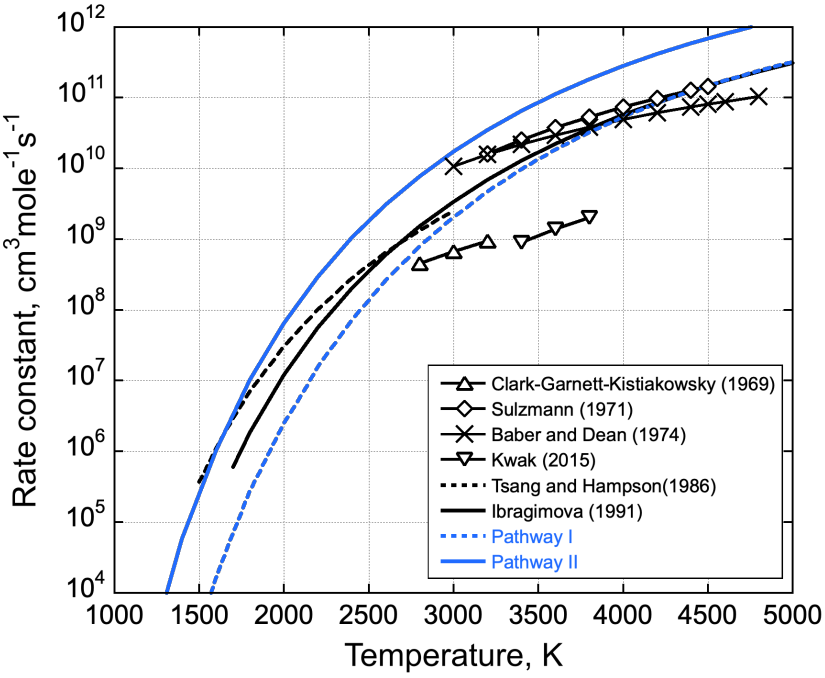

a. RRKM model

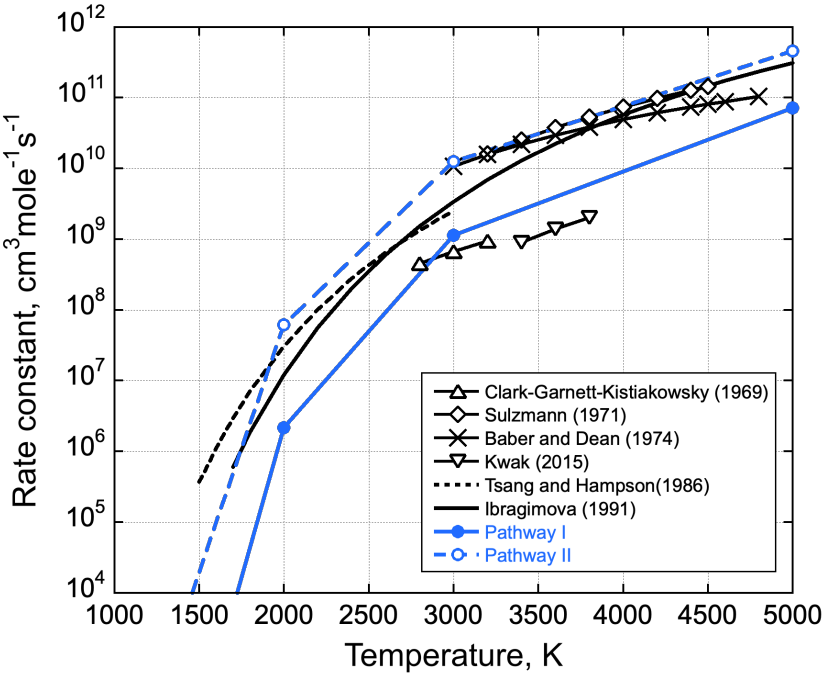

b. BM model

FIGURE 4.4 : RRKM and BM reaction constants for $CO_2(\tilde{X}^1\Sigma_g^+)$+O(^{3}P) → CO($X^1\Sigma_g^+$) + $O_2(X^3\Sigma_g^-)$

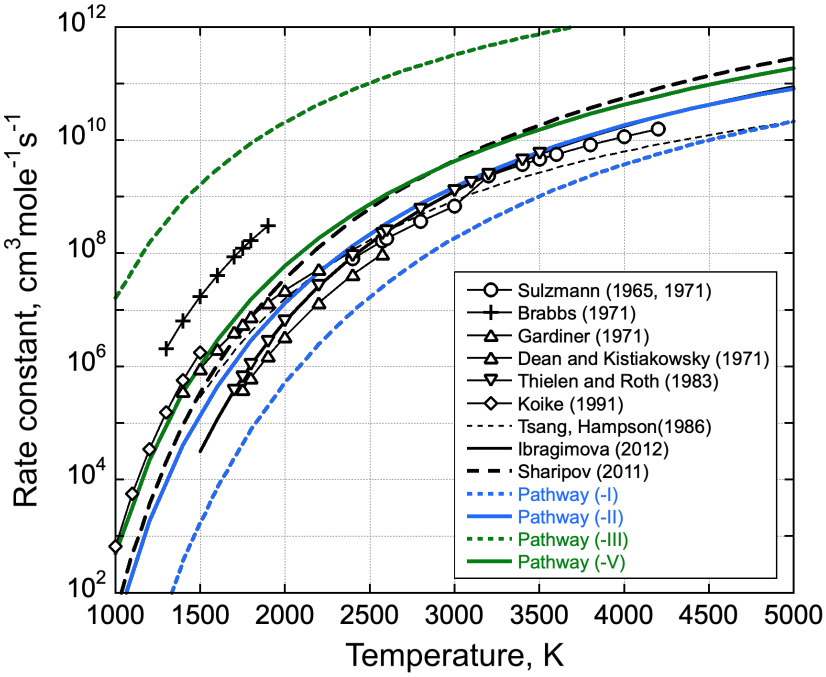

FIGURE 4.5 : RRKM reaction constants for $CO_2(\tilde{X}^1\Sigma_g^+) + O(^3P) \leftarrow CO(X^1\Sigma_g^+) + O_2(X^3\Sigma_g^-)$

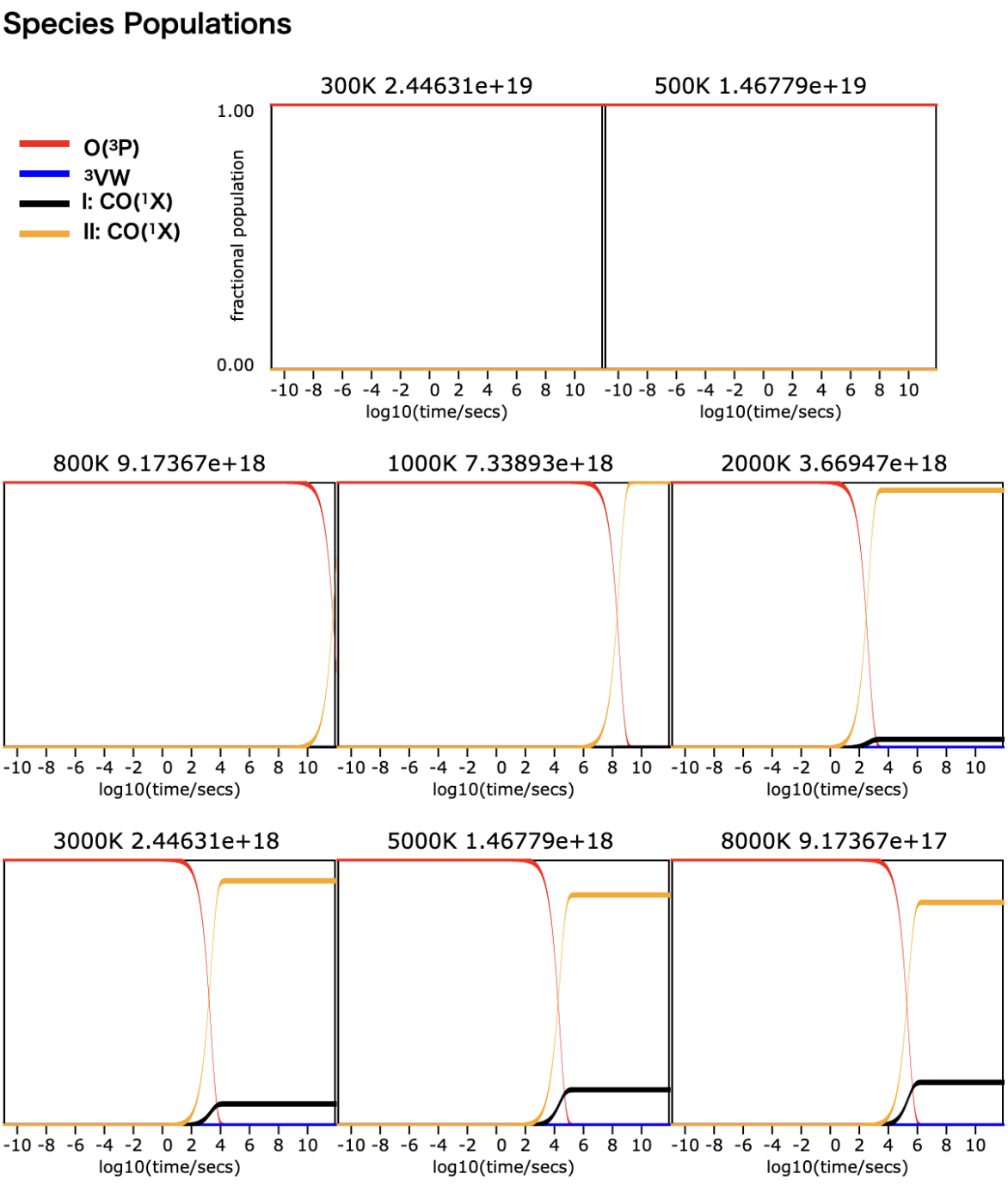

FIGURE 4.6 : Time evolution of species fractions at various temperatures

4.4 Summary

Based on the ab initio calculations, the stationary structures on the potential energy surface on the triplet CO_3 system were obtained, and two reaction channels of the exchange reaction $CO_2(\tilde{X}^1\Sigma_g^+) + O(^3P) \leftrightarrows CO(X^1\Sigma_g^+) + O_2(X^3\Sigma_g^-)$ were successfully found. More results, including the reaction path on the singlet surface and the reaction rate coefficients from transition state theory, will be presented.

Bibliography of Chapter 4

(1) PARK, C.; HOWE, J. T.; JAFFE, R. L. et al. Review of chemical-kinetic problems of future NASA missions. II - Mars entries. *Journal of Thermophysics and Heat Transfer* **1994**, *8*, 9-23.

(2) HYUN, S.-Y.; PARK, C.; CHANG, K.-S. Rate Parameters for Electronic Excitation of Diatomic Molecules : CN Radiation. *Journal of Thermophysics and Heat Transfer* **2009**, *23*, 226-235.

(3) SULZMANN, K. G. P.; MYERS, B. F.; BARTLE, E. R. CO Oxidation. I. Induction Period Preceding CO $_2$ Formation in Shock-Heated CO–O $_2$ –Ar Mixtures. *The Journal of Chemical Physics* **1965**, *42*, 3969-3979.

(4) SULZMANN, K. G. P.; LEIBOWITZ, L.; PENNER, S. S. Shock-tube studies on mixtures of NO, CO, and Ar. *Symposium (International) on Combustion* **1971**, *13*, 137-146.

(5) BRABBS, T.; BELLES, F.; BROKAW, R. Shock-Tube Measurements of Specific Reaction Rates in the Branched-Chain H_2-CO-O_2 System. *Symposium (International) on Combustion* **1971**, *13*, 129-136.

(6) GARDINER, W. C.; MCFARLAND, M.; MORINAGA, K. et al. Initiation Rate for Shock-Heated Hydrogen-Oxygen-Carbon Monoxide-Argon Mixtures as Determined by OH Induction Time Measurements. *The Journal of Physical Chemistry* **1971**, *75*, 1504-1509.

(7) DEAN, A. M.; KISTIAKOWSKY, G. B. Oxidation of Carbon Monoxide/Methane Mixtures in Shock Waves. *The Journal of Chemical Physics* **1971**, *54*, 1718-1725.

(8) CLARK, T. C.; GARNETT, S. H.; KISTIAKOWSKY, G. B. Reaction of Carbon Dioxide with Atomic Oxygen and the Dissociation of Carbon Dioxide in Shock Waves. *The Journal of Chemical Physics* **1969**, *51*, _eprint : https ://pubs.aip.org/aip/jcp/article-pdf/51/7/2885/18864136/2885_1_online.pdf, 2885-2891.

(9) BABER, S. C.; DEAN, A. M. Reaction of atomic oxygen with carbon dioxide behind reflected shock waves. *The Journal of Chemical Physics* **1974**, *60*, 307-313.

(10) KWAK, H. S.; UHM, H. S.; HONG, Y. C. et al. Disintegration of Carbon Dioxide Molecules in a Microwave Plasma Torch. *Scientific Reports* **2015**, *5*, 18436.

(11) SHARIPOV, A.; STARIK, A. Theoretical Study of the Reaction of Carbon Monoxide with Oxygen Molecules in the Ground Triplet and Singlet Delta States. *The Journal of Physical Chemistry A* **2011**, *115*, 1795-1803.

(12) TSANG, W.; HAMPSON, R. F. Chemical Kinetic Data Base for Combustion Chemistry. Part I. Methane and Related Compounds. *Journal of Physical and Chemical Reference Data* **2009**, *15*, 1087.

(13) IBRAGUIMOVA, L.; SHATALOV, O. Non-equilibrium Kinetics behind Shock Waves Experimental Aspects. *High Temperature Phenomena in Shock Waves* **2012**, DOI : 10.1007/978-3-642-25119-1_4.

(14) WERNER, H.-J.; KNOWLES, P. J.; MANBY, F. R. et al. The Molpro Quantum Chemistry Package. *The Journal of Chemical Physics* **2020**, *152*, 144107.

(15) VARGAS, J.; LOPEZ, B.; LINO DA SILVA, M. Heavy Particle Impact Vibrational Excitation and Dissociation Processes in CO_2. *The Journal of Physical Chemistry A* **2021**, *125*, 493-512.

(16) CANNEAUX, S.; BOHR, F.; HENON, E. KiSThelP : A program to predict thermodynamic properties and rate constants from quantum chemistry results†. *Journal of Computational Chemistry* **2014**, *35*, 82-93.

(17) GLOWACKI, D. R.; LIANG, C.-H.; MORLEY, C. et al. MESMER : An Open-Source Master Equation Solver for Multi-Energy Well Reactions. *The Journal of Physical Chemistry A* **2012**, *116*, 9545-9560.

Conclusion

In this study, the potential energy surfaces (PESs) of the CO_3 system were investigated focusing on their role in the O + CO_2 → O_2 + CO reaction, a key process during Martian atmospheric entry. Using *ab initio* quantum chemistry methods, both ground and excited states of CO_3 were examined to explore the detailed reaction processes.

Firstly, to learn the nature of interactions between the electronic states, the Li_2 dimer was analyzed as a model system using a high-level *ab initio* method, Multi-Reference Configuration Interaction (MRCI) method along with a flexible basis set consisting of 13s8p5d3f Gaussian atomic basis functions. The result exhibits complex potential energy curves because the types of interactions vary as functions of the internuclear distance and the energy level; covalent bonding in the short range, resonant ionic bonding in the middle range, steric characteristics in the long range, and several avoided crossing due to the atomic orbital interactions. This work provided spectroscopic constants from the 1 to $5^1\Sigma_u^+$ states, where those of the 4th and 5th $^1\Sigma_u^+$ states were not reported elsewhere.

Then, a large area of the seven-dimensional PESs of the CO_3 system is explored for the possible transition and intermediate structures and the reaction paths of O + CO_2 → O_2 + CO. This work resulted in finding three intermediate states not reported so far in the literature : one star-shape triplet state (^{3}EQ2) and two chain-shape singlet states (^{1}EQ3 and ^{1}EQ4) of CO_3. We have used a larger basis set and introduced more electron correlation effects than used in previous theoretical studies and found a better agreement with the available experimental data. In addition to the two triplet reaction pathways reported in the literature, we also found three new connections between the intermediate states on the singlet PESs at high energies ($\simeq 80\tilde{\text{k}}$cal/mol) above the $CO_2(\tilde{X}^1\Sigma_g^+)$ + O(^{3}P) ground state asymptote, but energetically accessible from the $CO_2(^3B_2)$ + O(^{3}P) asymptote.

Finally, using the obtained transition and intermediate states and the reaction pathways, the kinetics of the reaction O + CO_2 → O_2 + CO was investigated by the energy grained master equations (EGME) with the microcanonical rate constants by RRKM model. The obtained rate constants agree reasonably well with the experimental and theoretical values in the existing studies, consolidating confidence in the results.

By using state-of-the-art quantum chemistry methods, this work has provided a detailed reaction mechanism about the reaction O + CO_2 → O_2 + CO, which would be involved in Mars entry flows. The results can also offer valuable data that can be used to improve the thermochemistry models for hypersonic flow simulations. This research can contribute to improving thermal protection technology for Mars entry so as to enhance the overall safety of planetary exploration missions in the future.